



UNIVERSITY OF THE
WITWATERSRAND,
JOHANNESBURG

The effect of friction hydro-pillar processing on the properties
and characteristics of ASTM grade P92 steel

Tumelo Moropene

378860

School of Chemical & Metallurgical Engineering

University of the Witwatersrand, Johannesburg.

South Africa.

Supervisor: Prof. L.A Cornish

A research report submitted to Faculty of Engineering and the Built Environment,
University of the Witwatersrand, Johannesburg, in fulfilment of the requirements for the
degree of Master of Science in Engineering.

30 June 2021

DECLARATION

I, Tumelo Moropene (Student number: 378860) am a student registered for the degree of Master of Science in Metallurgy and Materials Engineering in the academic year 2021.

I hereby declare the following:

I am aware that plagiarism (the use of someone else's work without their permission and/or without acknowledging the original source) is wrong.

I confirm that the work submitted for assessment for the above degree is my own unaided work except where I have explicitly indicated otherwise.

This task has not been submitted before, either individually or jointly, for any course requirement, examination or degree at this or any other tertiary educational institution.

I have followed the required conventions in referencing the thoughts and ideas of others.

I understand that the University of the Witwatersrand may take disciplinary action against me if there is a belief that this is not my own unaided work or that I have failed to acknowledge the source of the ideas or words in my writing.

Signature: _____

Date: _____

ABSTRACT

The effect of the Friction Hydro-Pillar Process (FHPP) on the microstructure and hardness of P92 ferritic/martensitic steel was studied to determine whether FHPP could be used to repair cracks in the main steam pipes of power plants. The microstructural evolution, phase formation and hardness of the P92 steel were analysed.

Thermo-Calc software with the TCFE5 database was used to calculate phase proportion diagrams for the P92 pipe and weld samples. Gleeble uniaxial compression tests were used to simulate the FHPP weld. Hot compression tests were done at 1100°C and 1200°C at strain rates of 10 s^{-1} and 50 s^{-1} in order to simulate FHPP weld. The compressed samples were subsequently heat treated at 760°C for 3 hours 45 minutes or 5 hours because the provided FHPP welds had been heat treated.

Thermo-Calc phase proportion diagrams indicated BCC as the major phase with minor amounts of M_{23}C_6 , MnS, M_2B , MX, FCC and Laves phases. The Gleeble uniaxial compression results showed that the flow stress increased with decreased deformation temperature and increased strain rate. The FHPP weld had good integrity without defects. The FHPP weld sample was fully tempered martensite with $254\pm 19\text{ HV}_{0.3}$ hardness, whereas the hot compressed specimens had $449\pm 11\text{ HV}_{0.3}$ hardness. The heat treatment reduced the hardness of the hot compressed samples to $280\pm 29\text{ HV}_{0.3}$. Gleeble compression tests with subsequent heat treatment reproduced the FHPP weld structure. Thus, FHPP can be used to repair steam pipes because of the good integrity of the weld.

DEDICATION

Dedicated to my grandparents Chimamone and Madikana Moropene for their love and support through my research journey, despite not being knowledgeable about my work.

ACKNOWLEDGEMENTS

“There is no such a thing as a self-made man. You will reach your goal only with the help of others”-George Shinn. I would like to express my sincere and heartfelt gratitude to the following individuals, without whom the completion of this work would not have been possible:

My supervisors, Prof. L.A Cornish and Prof.L.H Chown for the unparalleled support, guidance, love and patience. I appreciate you Prof, you are the best! My mentor, Dr Michael Bodunrin, thank you for assistance with Gleeble tests, guidance with write-up and the moral support. My Friend and brother, Matimba Mkansi, for moral support and constructive research discussions. My sister, Dr Manoko Maubane for moral and academic support. A sister and friend Dr Madinoge Mampuru for academic support and motivation.

Special recognition to my work reviewers: Dr Liberty Chipise, Miss Mamokete Motjomane, Mr Tatenda Chingosho, Mr Japheth Obiko, Miss Phylis Makurunje and Mr Aubrey Lebea.

I would like to recognise and appreciate the following institutions and departments: Nelson Mandela University for P92 pipe and weld samples. A big thank you to Mr Louis Von Weilligh. MIP for Metallography, a great thank you goes to Mr Brian Bakkes and Mr Wayne Bakkes. The Wits Microscopy Unit for training and operating the microscopes. The Richard Ward and Physics Laboratory, for the assistance, a big thank you to Mr Shadreck Moqabolane, Mr Donald Mahole, Mr Brayner Nelwalani, Mrs Petra Dinham ,Mr Francis, Mr Mohlatsi and student assistant, Miss Thabiso Mashole and Mr Mokgomotsi Leshetla. DSI-NRF Centre of Excellence in Strong Materials (CoE-SM) for the support.

To those who constantly reminded me that giving up is not an option. To mention a few: Dr N.Ramafalo, Miss T Makoti, Miss T Ngobeni, Mr M Hlatshwayo, Miss R Mokwena, Mr E Ngoepe, Miss M Masia, Miss K Makoti, Miss N Rapetswa, , Miss I Skhosana, Mr T Mafubedu, K Motshoeneng Miss A Nkoane, Mr M Mudimeli, Mr M Mphahlele, Mr S Monepya Miss K Mabusela, Mr M Mashaba, Miss P Nkambule, Miss L Sithole, Miss E Nzumeni, Mr T Mphahlele, Miss K Mabala and Mrs N Fakude, I thank you all.

I can never forget my home away from home, IPHC Wits structure, for invaluable support.

A big thank you the uncle Rodney and aunt Desiree Futhana for always believing in me

To my Mother (Maggie Moropene) and my entire family, thank you for the LOVE and support you showed me since day one of my academic journey.

Last but definitely not least, His Grace Comforter FS-MG-FLG Modise, *Ntate kea leboga!!!*

TABLE OF CONTENTS

Chapter 1 Introduction	1
1.1 Overview of the FHPP process and CSEF steels	1
1.2 Motivation	2
1.3 Problem statement	3
1.4 Research aim and objectives	4
1.5 Outline of the dissertation	4
Chapter 2 Literature survey	5
2.1 Brief background on the establishment of ultra-supercritical (USC) plants	5
2.2 Creep Strength Enhanced Ferritic steels	6
2.2.1 History and development of Creep Strength Enhanced Ferritic steels	6
2.2.2 Background on ASME P91 and P92 steels	7
2.2.3 Effect of alloying elements	8
2.3 Hot forming behaviour of steels	12
2.3.1 Effect of hot deformation on the microstructure of steels	12
2.3.2 Work hardening	14
2.3.3 Dynamic recovery	14
2.3.4 Dynamic recrystallization	14
2.3.5 Factors affecting dynamic recrystallisation	18
2.3.6 Hot forming behaviour of 9% Cr ferritic-martensitic steels	20
2.3.7 Microstructural evolution of 9% Cr ferritic-martensitic steels at high temperatures	23
2.3.8 Precipitates in 9% Cr martensitic ferritic steels	25
2.4 Heat treatment	26
2.4.1 Fundamental concepts in steel heat treatment	26

2.4.2	Effect of heat treatment on P92 steels.....	27
2.5	Thermodynamic calculations	27
2.5.1	Software general description.....	27
2.5.2	Application of Thermo-Calc software	29
2.6	Friction Hydro-Pillar Processing (FHPP)	30
2.6.1	Friction hydro-pillar processing overview	30
2.6.2	Terminology associated with FHPP.....	30
2.6.3	The FHPP hole configurations and process stages	32
2.6.4	Effect of FHPP process variables on the weld structure and material properties	34
2.7	Rational of the project	36
Chapter 3 Experimental procedure		38
3.1	Materials.....	38
3.2	Thermodynamic calculations	38
3.3	Thermomechanical testing (Uniaxial compression).....	38
3.4	Heat treatment	41
3.5	Material characterisation	42
3.5.1	Metallographic preparation.....	42
3.5.2	Optical microscopy	43
3.5.3	Scanning electron microscopy (SEM)	44
3.5.4	X-ray diffraction (XRD)	45
3.5.5	Hardness.....	45
3.5.6	Grain size estimation.....	46
Chapter 4 Results		47
4.1	Thermodynamic calculations	47
4.2	Hot compression of P92 steel.....	51
4.3	Characterization	55

4.3.1	Chemical analysis	55
4.3.2	Microstructural analysis	58
4.3.3	X-ray diffraction	78
4.3.4	Hardness.....	80
Chapter 5 Discussion		84
5.1	Thermodynamic calculations	84
5.2	Hot compression of P92 steel.....	84
5.3	Characterization	85
5.3.1	Chemical analysis	85
5.3.2	Microstructural analysis.....	86
5.3.3	X-ray diffraction	88
5.3.4	Hardness.....	88
Chapter 6 Conclusion.....		90
Chapter 7 Recommendations		92
Chapter 8 References		93

LIST OF FIGURES

Figure 2.1:	Development of ferritic/martensitic steels with the coloured boxes showing evolution from T9 to P/T92 steel [28].	6
Figure 2.2:	Schaeffler-Schneider diagram showing the relative positions of various steels including P92 [50].	12
Figure 2.3:	Deformation flow stress curves with microstructural evolution corresponding to the different stages of the curve [52, 53].	13
Figure 2.4:	Flow curves showing dynamic recrystallisation in typical single or multiple, cyclic peaks [62].	15
Figure 2.5:	Three types of recrystallisation mechanisms [61].	16
Figure 2.6:	Schematic illustration of discontinuous dynamic recrystallisation [63].	16
Figure 2.7:	Schematic illustration of continuous dynamic recrystallisation [63].	17
Figure 2.8:	Schematic illustration of geometric dynamic recrystallisation [63].	17
Figure 2.9:	Effect of true strain on $\ln Z$ for P92 steel [74].	22
Figure 2.10:	As-tempered microstructure of P92 before service [81].	23
Figure 2.11:	Microstructure evolution at high temperature [82].	24
Figure 2.12:	Different cooling treatments [89].	26
Figure 2.13:	CCT diagram for P92 Steel [92].	28
Figure 2.14:	Phase Structures [95].	29
Figure 2.15:	Phase proportion diagram for P91 [96].	29
Figure 2.16:	Friction welding technologies [1].	31
Figure 2.17:	Coring and tapered hole preparation process: a) cylindrical core sample is machined, b) core sample is removed, c) FHPP weld is performed, d) stud and flash are removed [102].	32
Figure 2.18:	Stud and hole configurations in FHPP [104].	32
Figure 2.19:	FHPP stages a) dwell, (b) burn-off and (c) forging [105].	33
Figure 2.20:	Schematic diagram of the FHPP process with macrograph of a weld cross-section [1].	35
Figure 2.21:	Region characteristics of the FHPP weld: base material (BM), heat affected zone (HAZ) and thermo-mechanically affected zone (TMAZ) [2].	35
Figure 2.22:	Nickel aluminium : a) as-cast and b) same material after FHPP processing [107].	36
Figure 3.1:	Gleeble chamber.	39

Figure 3.2: Photograph of X20 steel showing thermocouple positioning during FHPP processing.	40
Figure 3.3: Temperature profile of X20 steel processed with FHPP (thermocouple was placed 3mm from the weld).	41
Figure 3.4: Metallographic preparation of the P92 steel samples.	44
Figure 3.5: FHPP sample sectioning and mounting.	44
Figure 4.1: Thermo-Calc phase proportion diagrams for pipe steel: a) all phases, b) minor phases.	48
Figure 4.2: True stress-strain curves from the uniaxial Gleeble hot compression tests on the P92 pipe steel for different total strains: a) 50 %, b) 70 %, c) 90 %.	53
Figure 4.3: All true stress-true strain curves from the uniaxial Gleeble hot compression tests on the P92 pipe steel up to a total strain of 0.6.	53
Figure 4.4: Average maximum stresses attained at different strain rates and deformation temperatures for compressed P92 pipe steel samples.	54
Figure 4.5: Average proof stresses at different strain rates and deformation temperatures for compressed P92 pipe steel samples.	54
Figure 4.6: EDX spectrum of the as-received P92 pipe steel showing elements present.	56
Figure 4.7: EDX spectra of P92 FHPP weld sections: a) base metal and b) rod (filler) showing elements present.	57
Figure 4.8: Optical image of the as-received P92 steel showing martensite and PAGBs (scale bar = 5 μm).	58
Figure 4.9: Optical images for the P92 steel sampled deformed at 1100 °C and 50% total strain: a) as-deformed, b) deformed and heat treated for 5 hours, c) as deformed, d) deformed and heat treated for 3 hours 45 minutes, showing martensite (scale bar = 5 μm).	59
Figure 4.10: Optical images for the P92 steel sampled deformed at 1200 °C and 50% total strain: a) as-deformed, b) deformed and heat treated for 5 hours, c) as deformed, d) deformed and heat treated for 3 hours 45 minutes, showing martensite and PAGBs (scale bar = 5 μm).	60
Figure 4.11: SEM-BSE images for as-received P92 steel after etching: a) nitric acid, b) potassium hydroxide, c) ammonium persulfate, d) oxalic acid, showing coring and PAGBs (scale bar = 10 μm).	61
Figure 4.12: SEM-BSE images for as-received P92 steel after etching: a) Marble's reagent, b) Ferric chloride, c) Kalling's reagent, d) Murakami's reagent, e) Villella's reagent, showing tempered martensite, martensite laths and PAGBs (scale bar = 10 μm).	62

Figure 4.13: SEM-BSE image of the etched as-received P92 steel (scale bar = 20 μm), with inset of high magnification image of the circled area (scale bar = 2 μm) showing precipitates on PAGBs.	63
Figure 4.14: SEM-BSE image and EDX analysis of selected grain boundary precipitates in as-received P92 steel showing different precipitates.	64
Figure 4.15: SEM-BSE image and EDX analysis of a nitrogen-containing precipitate in as-received P92 steel.	65
Figure 4.16: SEM-BSE image and EDX analysis of an oxide inclusion in as-received P92 steel.	65
Figure 4.17: SEM-SE micrographs of the P92 samples deformed at 1100 $^{\circ}\text{C}$ with arrows showing martensite lath (scale bar = 10 μm).	67
Figure 4.18: SEM-SE micrographs of the P92 samples deformed at 1200 $^{\circ}\text{C}$ with arrows showing martensite lath (scale bar = 10 μm).	68
Figure 4.19: SEM-BSE micrographs of P92 samples deformed at 1200 $^{\circ}\text{C}$ and heat treated for 5 hours (scale bar = 10 μm).	70
Figure 4.20: SEM-BSE micrographs of P92 samples deformed at 1100 $^{\circ}\text{C}$ and heat treated for 5 hours (scale bar = 10 μm).	71
Figure 4.21: SEM-BSE micrographs of P92 samples deformed at 1100 $^{\circ}\text{C}$ and heat treated for 3 hours 45 minutes (scale bar = 10 μm).	72
Figure 4.22: SEM-BSE micrographs of P92 samples deformed at 1200 $^{\circ}\text{C}$ and heat treated for 3 hours 45 minutes (scale bar = 10 μm).	73
Figure 4.23: SEM-BSE micrograph of P92 sample deformed at 1100 $^{\circ}\text{C}$ and heat treated (scale bar = 5 μm).	74
Figure 4.24: SEM-BSE micrograph of P92 sample deformed at 1200 $^{\circ}\text{C}$ and heat treated (scale bar = 5 μm).	74
Figure 4.25: Micrograph of P92 FHPP weld cross-section with the dashed lines indicating the regions where hardness indentations were made.	76
Figure 4.26: Higher magnification SEM-BSE images of FHPP weld regions with the average prior austenite grain sizes (scale bar = 10 μm).	77
Figure 4.27: SEM-BSE image of Zone A: Rod-HAZ, showing precipitates on martensite lath boundaries (scale bar = 10 μm).	78
Figure 4.28: XRD pattern of the as-received P92 pipe steel sample.	79
Figure 4.29: XRD patterns of the BM (F), BM-HAZ (E) and Rod-HAZ (A) zones of the FHPP weld section, where zones are labelled as in Figure 4.25.	79

Figure 4.30:	Effect of strain rate on hardness of P92 pipe samples deformed at 1100 °C.	80
Figure 4.31:	Effect of strain rate on hardness of P92 pipe samples deformed at 1200 °C.	80
Figure 4.32:	Effect of heat treatment on hardness of P92 pipe samples deformed at 1200 °C and 10 s ⁻¹ and heat treated.	81
Figure 4.33:	Effect of heat treatment on hardness of P92 pipe samples deformed at 1200 °C and 50 s ⁻¹ and heat treated.	81
Figure 4.34:	Effect of heat treatment on hardness of P92 pipe samples deformed at 1100 °C and 10 s ⁻¹ and heat treated.	82
Figure 4.35:	Effect of heat treatment on hardness of P92 pipe samples deformed at 1100 °C and 50 s ⁻¹ and heat treated.	82
Figure 5.1:	The Schaeffler–Schneider diagram showing the relative positions of various steels including a T/P92 steel [50] and the P92 steel from this work.	86

LIST OF TABLES

Table 2.1:	Comparison of the coal consumption with plant operating conditions for the equivalent energy supply of power plant types [24].	5
Table 2.2:	Chemical composition of selected 9-12Cr steels [28].	7
Table 2.3:	Effect of composition on activation energy in steel P92.	22
Table 3.1:	Uniaxial compression testing matrix.	40
Table 3.2:	Grinding and polishing steps.	43
Table 3.3:	Electrolytic etching and the applied voltage.	43
Table 3.4:	Immersion etchants and times.	43
Table 4.1:	Equilibrium transformation temperatures from Thermo-Calc.	50
Table 4.2:	Phase fractions of minor phases at deformation from Thermo-Calc.	50
Table 4.3:	Phase fractions of the as-received sample at 700 °C from Thermo-Calc.	51
Table 4.4:	OES results of the P92 pipe sample and the P92 FHPP weld (base and rod metals).	55
Table 4.5:	EDX analyses of the P92 pipe sample and the P92 FHPP weld (base and rod metals) showing the average compositions with standard deviations.	56
Table 4.6:	Summary of EDX analysed precipitates and inclusions in as-received P92.	66
Table 4.7:	Average grain sizes of the tempered samples.	75
Table 4.8:	Hardness gradient across the weld (HV _{0.3}).	83

LIST OF ABBREVIATIONS

Abbreviation	Description
FHPP	Friction hydro-pillar processing
CSEF	Creep strength enhanced ferritic
USC	Ultra-supercritical
ASTM	American society for testing materials
ASME	American society for mechanical engineers
HAZ	Heat affected zone
TMAZ	Thermo-mechanically affected zone
PWHT	Post weld heat treatment
SFE	Stacking fault energy
DRX	Dynamic recrystallisation
DRV	Dynamic recovery

Chapter 1 : Introduction

1.1 Overview of the FHPP process and CSEF steels

Friction hydro pillar processing (FHPP) is a friction welding technique whereby an axial force is applied on a rotating consumable rod within a pre-machined hole [1-7]. The hydro pillar portion of the process name is derived from the mechanism whereby some of the plasticised stud material is continually deposited onto previously recrystallised stud material, forming the base for the next layer [8]. The FHPP can be used for repairing thick-section ferrous and non-ferrous plate materials [4 ,9, 10]. This solid welding technique will not completely replace fusion welding but minimise its use. This is because there are defects associated with the fusion welding techniques such as solidification cracking, segregation of alloying elements, solubility of gases, formation of undesirable phases and overheating [2, 9, 11, 12]. Furthermore, FHPP is easily automated, cheap and safe to perform underwater due to absence of high voltage electric hazards [9, 13].

Creep strength enhanced ferritic (CSEF) steels are highly alloyed steels that contains between 9 % and 12 % Cr, varying additions of W, Co, B, N, Ni, and small amounts of Nb, V, Mo [11]. The as received microstructure of CSEF steels is tempered martensite with finely dispersed carbides, nitrides and carbonitrides. The CSEF steels are relatively inexpensive compared to advanced austenitic stainless steels and nickel-based alloys [14]. Lower thermal expansion coefficient as well as the higher resistance to thermal fatigue properties of CSEF steels, make them tolerable to thermal stresses on the power plants due to regular start-ups and shut-downs [14-16].

The first CSEF steel to be approved for application in ultra-supercritical (USC) power plants is Grade P91/T91 [17]. However, the American Society for Testing and Materials (ASTM) and American Society of Mechanical Engineers (ASME) codes required that the diameter and wall thickness of the pipes should be reduced for operations at elevated temperatures [15]. This is because thinner components require less time to reach thermal equilibrium and therefore are less likely to be thermo-mechanically damaged during power plants shutdown cycles. The P91 steel (9Cr-0.5Si-0.6Mn-1.05Mo-0.1Nb-0.07N) was modified by addition of

mainly tungsten to form a 9Cr–0.05Si–0.2Mn–1.9W–0.5Mo–0.25V–0.07Nb–0.08N–0.01B, ASTM grade P92 steel to allow reduced wall thickness. The creep strength of P92 steel is more than 30% higher than P91 steel at 600 °C [15]. The P92 steel has high heat resistance [15, 18].

Creep strength enhanced ferritic steel weldments (HAZ (heat affected zone) and TMAZ (thermo-mechanically affected zone)) fail prematurely due to type IV cracking in the fine-grained heat affected zone and intercritical heat affected zone [14, 15]. Type IV cracking is creep cracking which occurs at the base material and HAZ interface [14]. It occurs at the surface of the HAZ in the over-tempered, intercritical region of the HAZ.

The FHPP process is an emerging technology and this work was aimed at generating knowledge about its application to CSEF steels. The FHPP literature is mainly focused on the effect of the applied force on the weld [3, 7, 10]. Currently, there has been little work done to understand the microstructural evolution during the process, hence the motivation for the present study. The microstructure and hardness of P92 steel processed by FHPP was analysed. The FHPP process was simulated on a laboratory scale by computer controlled thermo-mechanical simulation on a Gleeble 3500 to understand the conditions (deformation strain and strain rates) under which FHPP occurs.

1.2 Motivation

The amount of energy a country can produce drives its economic development, especially in developing countries like South Africa. Despite the advanced variants of technologies in the field of renewable energy, fossil fuels remain the dominant energy resource worldwide, accounting for 80% of energy production [19-22]. Coal is the cheapest and most reliable energy source providing at least 40% of the world's electricity needs; coal-fired plants produce approximately 90%, 40% and 79% of electricity in South Africa, United States of America and China respectively. Furthermore, fossil-fuel plants pose a danger on the environment through greenhouse gases emission. Therefore, an urgent intervention is needed to meet the energy demands with reduced fossil fuel consumption, thus reducing the carbon footprint and preserving the resources for future generations.

Power plants are required to operate at critical conditions (high temperatures and pressures) to produce energy with less environmental contamination from carbon containing gases [23].

At critical conditions, less fossil fuel is consumed for the same amount of energy output [24]. The need to operate power plants under critical conditions requires that major parts of the power plants such as turbines, boilers and piping systems be made of strong structural materials to withstand high temperatures and pressures.

The CSEF steels have adequate properties and are cost efficient, hence they are preferred for applications in power plants compared to nickel-based alloys and austenitic stainless steels [16]. ASTM grade P92 steel is by far the most advanced CSEF steel adopted for application in the power and energy industry due to its high temperature strength and creep performance [25-30]. However, CSEF steel weldments are prone to type IV creep cracking which can lead to catastrophic failure [14]. The FHPP process has the potential to combat this cracking problem, because the creep crack is removed by coring and then the resultant hole is then refilled with similar material. In the same way, FHPP can also be used for creep material sampling by cutting out a small portion of the component for a more accurate creep analysis of the component. As a solid welding process, FHPP does not have the problems of liquid phase. Thus, the technique enables *in situ* repairing of the components, therefore preventing unnecessary long shutdowns.

1.3 Problem statement

The use of FHPP is a possible solution for repairing both ferrous and non-ferrous industrial equipment without off-site removal. However, there is limited understanding of the process, especially its application to steel, and whether reliable welds could be produced. Therefore, the current research addressed this problem, specifically the analysis of the FHPP weldments produced on P92 steel. The following questions were addressed during this research:

1. What is the microstructure of the FHPP weldments, and how does it differ from the base material?
2. What are the mechanical properties of the FHPP weldment?
3. Can the microstructure of FHPP weldments be simulated by Gleeble?
4. Can heat treatment of the P92 weld specimens recover their initial microstructure and properties?

1.4 Research aim and objectives

The main aim of this study was to determine the influence of the FHPP technique on a steel grade P92 weldment, to ascertain whether it was a viable process to repair creep cracks, with the following objectives:

- To characterise the microstructure of the FHPP weldment.
- To determine the mechanical properties of the weldment.
- To simulate the FHPP weldment microstructure by performing Gleeble thermo-mechanical simulations.

1.5 Outline of the dissertation

Chapter 1: This chapter gives a brief overview and history of the FHPP process and CSEF steels. The motivation for this research, problem statement, objectives and aim of the study are also included.

Chapter 2: A literature review on FHPP and CSEF steels is presented.

Chapter 3: The experimental procedures and analytical techniques used in this study are described.

Chapter 4: The results obtained in this study are presented.

Chapter 5: The presented results are interpreted and discussed.

Chapter 6: Based on the results and objectives of the study, conclusions are drawn.

Chapter 7: This chapter presents the recommendations for further work.

References: All the sources used in this study are referenced

Chapter 2 : Literature survey

This chapter gives a brief history on the establishment of ultra-supercritical (USC) power plants and the background to development of creep enhanced ferritic steels. Since these are categorised as high alloy steels, the effect of the alloying elements is also discussed. This family of steel is used in high temperature applications and therefore the hot forming behaviour and microstructural evolution of the steels are discussed. The second part gives an overview of the FHPP welding technique. The last part briefly discusses heat treatment and thermodynamic calculations.

2.1 Brief background on the establishment of ultra-supercritical (USC) plants

Elsam, a large power generation organisation in Denmark, had a major objective of participating in research and development of new energy technologies [23]. In the 1990s, Elsam conducted intensive research into three coal-based technologies for power generation: integrated gasification combined cycle (IGCC), pressurised fluidised bed combustion (PFBC) and USC plants. The USC concept was the most feasible [15]. Table 2.1 [24] shows that higher pressure and temperature operation of USC increases the net efficiency and reduces the coal consumption. Not only will the coal resource last longer, but the emissions and resulting pollution will also decrease. However, strong materials are required in the piping system of the USC plants to withstand high temperatures and pressures.

Table 2.1: Comparison of the coal consumption with plant operating conditions for the equivalent energy supply of power plant types [24].

Type	Vapour parameter	Net efficiency (%)	Coal consumption (g.kW ⁻¹ .h ⁻¹)
Subcritical	(17 MPa, 538 °C)	37-38	330-340
Supercritical	(24 MPa, 538 °C)	40-41	310-320
Ultra-supercritical	(30 MPa, 556 °C)	44-45	290-300

2.2 Creep Strength Enhanced Ferritic steels

2.2.1 History and development of Creep Strength Enhanced Ferritic steels

Steel is an important material due to its wide variety of microstructures and resulting properties that can be generated by solid-state transformation and processing [25]. The heat resistant ferritic/martensitic steels also known as CSEF steels, originated in 1912 at Krupp and Mannesmann Ltd in Germany [26]. This steel family was developed and evolved into a series of compositions from different countries of origin (using ASTM designations): US - Gr. 91, Europe - Gr. 24 and Gr. 911, and Japan - Gr. 92, Gr. 122 and Gr. 23 [17]. In the mid 1980s, the first CSEF steel to be included in the ASME code was Gr. 91 when it was used in fossil fuelled power plants [17, 14, 27]. Figure 2.1 [28] shows the progress and development of CSEF steels with the coloured boxes showing evolution from T9 to P/T92 steel. Table 2.2 [28] shows the composition range of the common CSEF steels. In the names, the letters ‘T’ and ‘P’ were derived from their primary applications, thus T for tubing and P for piping [27]. Tube refers the different shapes of hollow sections used for the conveyance of products such as gases and fluids. A pipe is a circular tube [29].

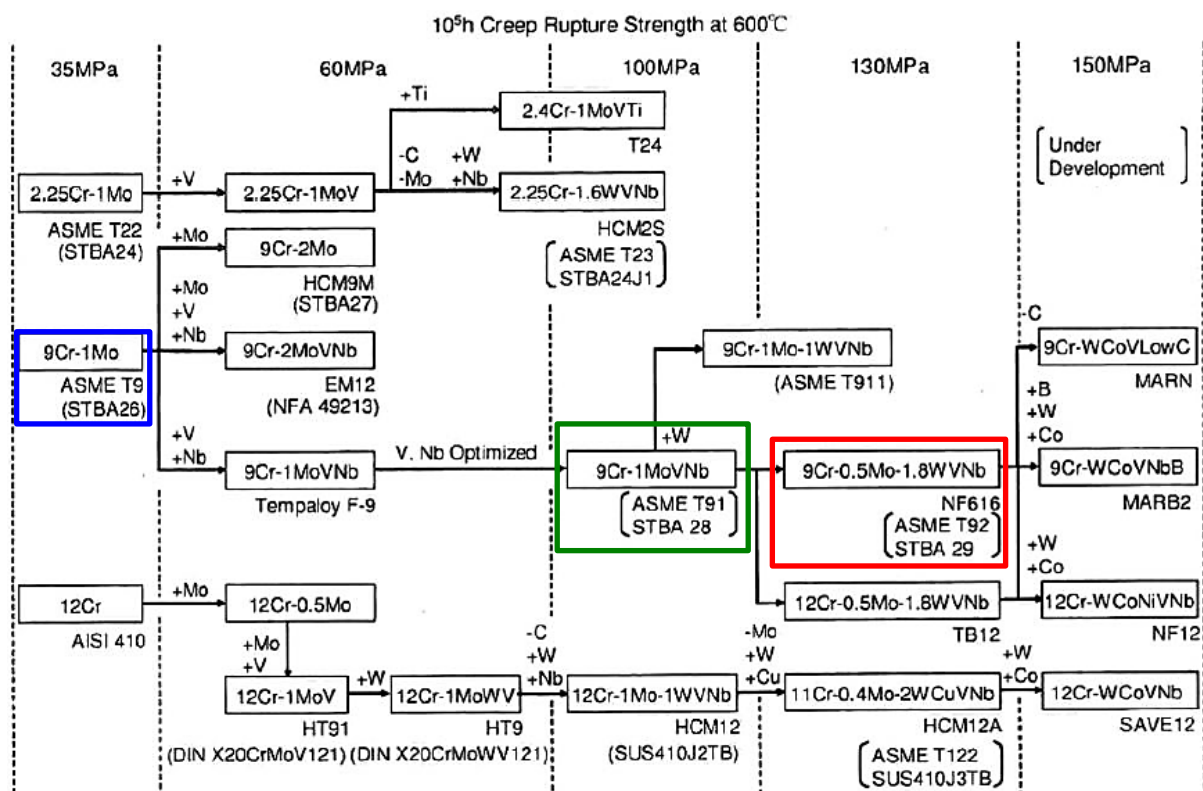


Figure 2.1: Development of ferritic/martensitic steels with the coloured boxes showing evolution from T9 to P/T92 steel [28].

Table 2.2: Chemical composition of selected 9-12Cr steels [28].

Element	Grade 91	NF616 (grade 92)	HCM12A	TB 12M	Grade 911	Grade 122	FB2
C	0.08–0.12	0.07–0.13	0.07–0.14	0.10–0.15	0.09–0.13	0.07–0.14	0.13
Mn	0.20–0.60	0.30–0.60	≤0.70	0.40–0.60	0.30–0.60	≤0.70	0.82
Si	0.20–0.50	≤0.50	≤0.50	≤0.50	0.10–0.50	≤0.50	...
S	≤0.010	≤0.010	≤0.010	≤0.010	≤0.010	≤0.010	...
P	≤0.020	≤0.020	≤0.020	≤0.020	≤0.020	≤0.020	...
Cr	8.00–9.50	8.50–9.50	10.00–12.50	11.0–11.30	8.50–10.50	10.0–12.5	9.32
Mo	0.85–1.05	0.30–0.60	0.25–0.60	0.40–0.60	0.90–1.10	0.25–0.60	1.47
W	...	1.50–2.00	1.50–2.50	1.60–1.90	0.90–1.10	1.50–2.50	...
Co	0.96
Ni	≤0.40	≤0.40	≤0.50	0.70–1.0	≤0.40	≤0.50	0.16
Cu	0.30–1.70	0.30–1.70	...
V	0.18–0.25	0.15–0.25	0.15–0.30	0.15–0.25	0.18–0.25	0.15–0.30	0.20
Nb	0.06–0.10	0.40–0.09	0.09–0.10	0.04–0.09	0.06–0.10	0.04–0.10	0.05
N	0.030–0.070	0.030–0.070	0.040–0.100	0.04–0.09	0.040–0.090	0.040–0.100	0.019
Al	≤0.04	≤0.040	≤0.040	≤0.010	≤0.04	≤0.04	–
B	...	0.001–0.006	≤0.005	0.0005–0.005	0.0083
Sn	≤0.010
As	≤0.010
Sb	≤0.005
10 ⁵ h creep	600 °C 94	(115)*	(115)	[150 (10 ⁵ h)]	(115)
rupture strength	650 °C 50	(60)*	(60)	[80 (10 ⁵ h)]	(65)
/MPa							

2.2.2 Background on ASME P91 and P92 steels

The previous section gave a general overview of CSEF steels and this section discusses two CSEF steels, P91 and P92. ASME P91 steel was developed in the USA by Oak Ridge National Laboratory and Combustion Engineering in the 1970s for application in nuclear pressure vessels [16]. However, it was only approved as a construction material for power plants application by ASTM/ASME between 1983 and 1985 [14, 15, 17]. Figure 2.1 shows that P91 steel was developed by modification of 9Cr-Mo (T9) steel by optimising the niobium, carbon, and vanadium contents, and adding nitrogen, hence it is also referred to as modified 9Cr-1Mo steel. These modifications enhanced the strength of this family of alloys which made it suitable for application at elevated temperatures and pressures.

P91 steel has been widely used in the power industry due to its good combination of creep and corrosion resistance. However, ASTM and ASME codes require the pipe diameter to be smaller and pipe wall thickness to be thinner for operations at 600 °C and above [17, 30]. This is because the thinner components require less time to reach thermal equilibrium within the station and are therefore less likely to be thermo-mechanically damaged during station shutdown cycles [15]. Therefore, to satisfy the wall thickness and diameter reduction requirement, more advanced alloys had to be designed, and P92 steel was one of the products. The NF616 steel, which was later designated by ASTM as P92 steel, was developed in the late 1980s by Nippon Steel of Japan [17, 31]. This steel is a modification of P91 steel by substituting half of the molybdenum (Mo) for tungsten (W) to achieve solid solution

strengthening with 0.5% Mo and 1.8% W, whilst vanadium and niobium are added for precipitation strengthening. In addition, boron and slightly more nitrogen were also added [15, 31, 32].

2.2.3 Effect of alloying elements

The chemistry of an alloy plays a critical role in maintaining its integrity under different conditions during application. Medina and Hernandez [33] found that an increase in the amount of the alloying elements: Mn, Si, Mo, Ti, V, and Nb, increased the activation energy of the steel, but carbon showed the opposite effect. How the alloying elements reacted enabled them to be classified into two categories: carbide formers which are also nitride formers (*e.g.* Cr, Mn, Mo, W, V, Ti, and Nb) and non-carbide formers (*e.g.* Ni, Si, Co, Al, Cu, N) [34, 35]. With the exception of Cu and N, the non-carbide formers do not form chemical compounds with Fe and C, and are therefore only in solution [34].

P92 and P91 steels are the most commonly and widely applied steels in the ferritic-martensitic modified 9% Cr steels. Modified 9% Cr steels have enhanced strength derived from the additional alloying elements compared to the conventional 9% Cr steels. These alloy modifications improve the component life, rupture strength and safety margin, and also reduce the wall thickness of the pipe [30]. Alloying elements in CSEF steels are either austenite stabilisers if they dissolve in austenite and widen the austenite phase field (*e.g.* Ni, Mn, N, Cu, and C) or ferrite stabilisers if they dissolve in ferrite and widen the ferrite phase field (*e.g.* Cr, Si, Al, Ti, V, Nb, Mo, and W) [34, 35].

Ferrite stabilisers decrease the enthalpy of ferrite, thus requiring more energy to transform to austenite, which leads to an increase in the A_{e1} transformation temperature (800 - 830 °C), which is the minimum temperature at which ferrite begins to transform to austenite [35, 36, 37]. Conversely, the austenite stabilisers decrease the A_{e1} temperature. Alexandrov *et al.* [37] highlighted the importance of the A_{e1} temperature in P91 and P92 steels. They found that exceeding the A_{e1} temperature during post weld heat treatment resulted in formation of α ferrite and/or fresh martensite in the final weld microstructure, both which are detrimental to the creep strength and toughness. Addition of alloying elements moves the time-temperature-transformation (TTT) curves to shorter times, thus increasing hardenability, which results in martensite forming at lower cooling rates [34].

The effects of the key alloying elements are discussed further in this section. For the steel to take the full advantage of the alloying elements, the amount of each element must be carefully optimised, so that it is in the required proportions relative to the other elements.

Carbon

The high solubility of carbon in austenite and low solubility in ferrite makes it a strong austenite stabiliser, and promotes the formation of carbides and carbonitrides [27]. Carbon was found to have a slight softening effect in high alloy steels, thus the peak stress decreased with increase in carbon amount [33]. Dudko *et al.* [18] found that the long term creep rate was accelerated by a lower carbon content in P92 steel. Tungsten and molybdenum provide solid-solution strengthening on the matrix. A lower carbon content decreases the solubility of tungsten and molybdenum.

When carbon forms $M_{23}C_6$, Cr is removed from the austenite, thus effectively lowering its content, and reducing the growth of the Z-phase [38]. Z-phase (Cr(V,Nb)N) is the undesired precipitate formed at the expense of MX, M_2X (where $M=V,Nb$ and $X=C,N$) and $M_{23}C_6$ which deteriorate the strength of the steel. However, an extremely low C content is required to promote the formation of fine and thermally stable MX nitride particles instead of thermally unstable $M_{23}C_6$ particles [39]. A higher carbon content also reduces the weldability of the steel by increasing its hardness, thus makes it more brittle [27], although the carbon content has no significant effect on toughness in P92 steel [40].

Nitrogen

Nitrogen is a strong austenite stabiliser like carbon, and forms nitrides and carbonitrides [27]. Nitrogen addition significantly improves creep strength, provided it does not form boron nitride, which severely deteriorates creep strength [39]. This can be ascribed to the increase in tensile and yield strength at the expense of the toughness and ductility of the steel [41]. Chovet *et al.* [40] found that decreasing the N content substantially improved the toughness in P92 steel. Nitrogen is a component of the Z-phase, thus encouraging its formation [42].

Chromium

Chromium provides minimal solution strengthening when added to iron, so its primary role in steels is for oxidation resistance and corrosion resistance [27]. Chromium is a relatively weak carbide former, and only starts forming carbides above 1 wt% Cr [34]. The diffusion rate of

Cr is higher than most other carbide and nitride formers in ferrite, hence the coarsening rate of Cr precipitates is high [34]. A high Cr content of 10 wt% and above accelerates Z-phase formation [43]. High Cr content also stabilises ferrite.

The Cr_{eq} equivalent equation [34] adds the amounts of elements that are ferrite stabilisers, such as chromium:

$$Cr_{eq} \text{ (wt\%)} = Cr + 2Si + 1.5Mo + 5V + 5.5Al + 1.75Nb + 1.5Ti + 0.75W \dots\dots [2.1]$$

Nickel

Nickel has the greatest effect on stabilising the austenite, and significantly decreasing the Ae_1 temperature [34, 37] . Nickel content is kept at about 0.5 wt% to prevent the formation of delta ferrite, thereby improving the toughness [44]. Nickel accelerates precipitation coarsening and promotes the formation of M_6C , thus reducing formation of $M_{23}C_6$, which is used to stabilise the subgrain structure [27]. The Ni_{eq} equivalent equation [34] adds the amounts of elements like nickel that are austenite stabilisers:

$$Ni_{eq} \text{ (wt\%)} = Ni + Co + 0.5Mn + 30C + 0.3Cu + 25N \dots\dots\dots [2.2]$$

Tungsten

Tungsten is one of the key elements in modified ferritic-martensitic steels. The lower diffusion rate of W in ferrite compared to Nb and Mo, slows precipitation of the Laves phase [27, 45]. The major role of tungsten is to enhance the creep strength through solid solution strengthening and pinning effects. This delays the recovery of martensite lath and inhibits coarsening of $M_{23}C_6$ carbides, thus enhancing the martensite stability during long-term exposure at elevated temperatures [45]. The addition of W is kept at the minimum required value to avoid the formation of delta ferrite as it has a negative effect on the steel [41].

Manganese

Manganese has the second largest effect after nickel on reducing the Ae_1 temperature [37]. This affects the post weld heat treatment (PWHT) temperature and toughness in the ferritic martensitic steels [41, 44]. When the PWHT temperature is low there is insufficient tempering, which results in inadequate toughness [46]. Moreover, if the PWHT temperature exceeds the Ae_1 temperature, the metal undergoes the reverse transformation, which promotes a microstructure with fresh martensite of high strength and low toughness.

Molybdenum

Molybdenum is a strong carbide former and ferrite stabiliser [27, 34] . Molybdenum has the ability to form fine carbides with high enthalpies, which remain fine for prolonged times at higher temperature exposure [34]. A molybdenum equivalent, Mo_{eq} [34], in solid solution is defined as:

$$Mo_{eq} = Mo + 0.5 W \text{ (wt\%)} \dots\dots\dots [2.3]$$

The Mo_{eq} should be less than 1 wt%, otherwise precipitation of the Laves phase will occur, removing molybdenum from solid solution and causing poor solid-solution strengthening [27].

Silicon

Silicon is an essential deoxidant. In conjunction with chromium, it improves oxidation resistance at higher steam temperatures [44]. Silicon slows down the nucleation and growth of cementite, promoting the formation of the more stable carbides [34]. Laves phase precipitation is substantially hindered by a decrease in silicon content [47]. This can be attributed to the fact that silicon reduces molybdenum solubility, therefore promoting Laves phase precipitation [48].

Boron

The primary role of boron (B) is to enhance hardenability since it is a surface-active element. However, too much B decreases toughness by precipitation of Fe_2B on austenite grain boundaries [27, 34] .

Niobium

Niobium (Nb) is a strong carbide former [34, 35]. Undissolved Nb carbides impede grain growth during austenitisation. Niobium increases the recrystallisation temperature more than other alloying elements, significantly retarding the softening rate [34, 35]. Lee *et al.* [49] found that Nb addition in ferritic steel with 10 wt% Cr improved the short term creep, but was detrimental to the long term stability due to Z-phase formation, which in turn shortens its creep rupture life.

Vanadium

Vanadium (V) is a strong carbide, nitride and carbonitride former with most of its compounds rich in nitrogen [27]. Vanadium forms carbides and carbonitrides from as little as 1 wt% V [33], [34]. Vanadium carbides replace cementite in steels and persist as fine particles at high temperatures [34]. Nonetheless, vanadium carbides are more stable below A_{e1} temperature [34].

Cr and Ni equivalents

A typical P92 steel composition is shown on the Schaeffler – Schneider diagram (Figure 2.2) [50]. P92 is on the phase boundary of martensite and martensite + ferrite, indicating that it contains mostly martensite, with $\leq 2\%$ ferrite.

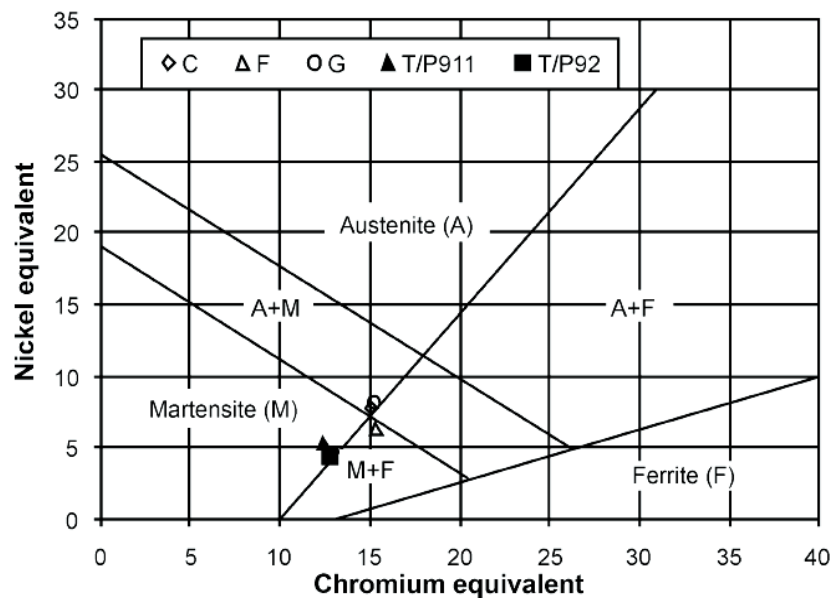


Figure 2.2: Schaeffler-Schneider diagram showing the relative positions of various steels including P92 [50].

2.3 Hot forming behaviour of steels

2.3.1 Effect of hot deformation on the microstructure of steels

Steels are hot formed to produce complex shapes with good strength [51]. The trend in metals has always been to improve mechanical properties because they are why metals have numerous applications. The most important properties are: ease of fabrication, high strength, relatively good ductility and corrosion resistance [51]. One of the ways of acquiring the best

combination of these properties is to select the optimum microstructure, which in turn depends on thermo-mechanical history as well as on chemical composition [52].

Generally, flow curves are used to interpret the mechanisms involved during deformation. Figure 2.3 [52, 53] uses flow curves as well as microstructural evolution to illustrate these metallurgical phenomena during the hot forming process: work/strain hardening, dynamic recovery (DRV) and dynamic recrystallisation (DRX).

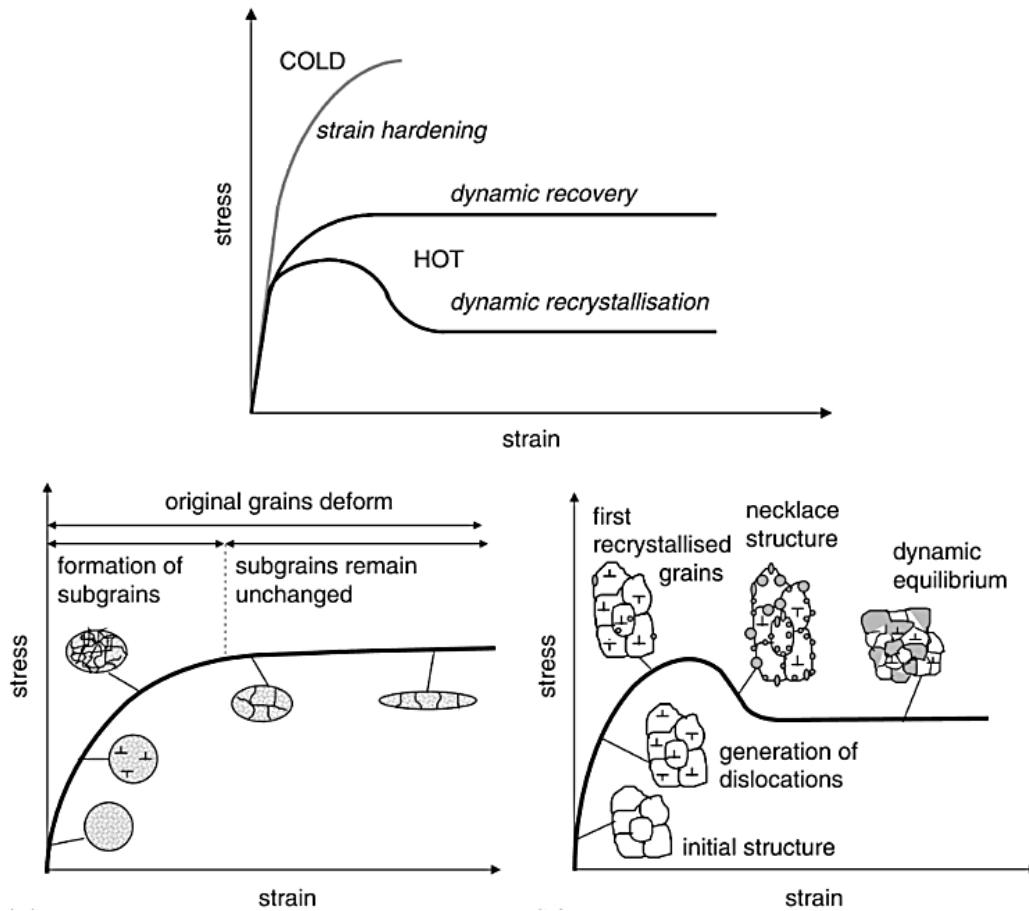


Figure 2.3: Deformation flow stress curves with microstructural evolution corresponding to the different stages of the curve [52, 53].

During hot deformation at relatively high strain rates, the energy is stored in the form of dislocations and the deformed material undergoes work hardening [54]. As the deformation continues, part of the stored energy is released by dislocation rearrangement and annihilation through dynamic recovery. However, with further deformation, the dislocation density reaches a critical point necessary to promote the nucleation of new grains by dynamic recrystallization [54]. However, these competing phenomena occur simultaneously

throughout the deformation process, and the distinct stages are based on which one is predominant at a given point in the deformation process.

2.3.2 Work hardening

Dislocations are the basis of plastic deformation. Plastic deformation requires imperfections, such as dislocations, which move through the lattice when the stress is applied [55]. In the initial stages of deformation, the dislocations are generated and multiplied by a gradual increase in the applied stress or strain [52, 56]. When the density of these dislocations reaches a critical value, they begin to interact. This makes their movement difficult, leading to work hardening, which strengthens the material, seen as the increase in flow stress at later deformation stages.

2.3.3 Dynamic recovery

Materials tend to maintain their stable state where their free energy is at the lowest [57]. A work hardened material is thermodynamically unstable, so the material responds in a way that will minimise the free energy of the system and restore the initial structure. When deformation is carried out at higher temperatures, the restoration process that manifests is dynamic recovery (DRV). At these elevated temperatures, the diffusion rate increases, which promotes dislocation motion [51]. The mobile dislocations decrease the dislocation density by annihilation and formation of low-energy dislocation configurations which relieve some of the internal strain energy [52].

During DRV, the original grains are increasingly strained, but the subgrains remain more or less equiaxed (Figure 2.3) [52]. This implies that the substructure is dynamic and readapts continuously to the increasing strain. The DRV rate is lower in low stacking fault energy (SFE) materials like copper. Low SFE materials allow stored energy accumulation until a critical strain when there is a significant variation in the energy distribution and that marks the onset of DRX.

2.3.4 Dynamic recrystallization

DRX is an important mechanism which controls microstructural evolution during hot deformation [58]. During the deformation of materials with moderate to low SFE, the

dislocation mobility is hampered due to wide stacking faults not being able to cross-slip thus uneven dislocation distribution [59-61]. This results in a high local dislocation density which acts as a nucleation sites for new grains. The nucleation and growth of the new grains affect the mechanical behaviour of the material. DRX is characterised by peaks appearing in the flow stress curve, each with an associated peak strain as shown in Figure 2.4.[62] The driving force for DRX is the stored energy in the deformed material due to plastic deformation.

Dynamic recrystallisation has been categorised into three types: discontinuous dynamic recrystallisation (DDRX), continuous dynamic recrystallisation (CDRX) and geometric dynamic recrystallisation (GDRX) as shown in Figure 2.5 [61]. However, mechanisms of these DRX co-exist and occur interchangeably, for an example, CDRX can be seen in low SFE metals although it is expected to occur in high SFE metals [61].

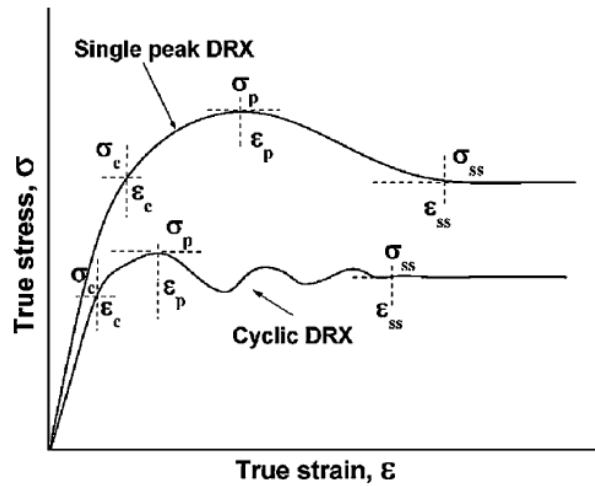


Figure 2.4: Flow curves showing dynamic recrystallisation in typical single or multiple, cyclic peaks [62].

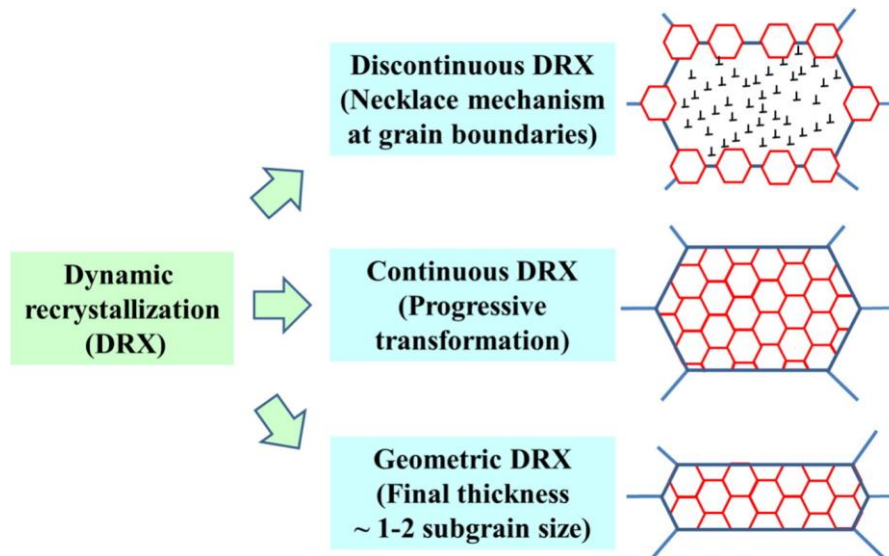


Figure 2.5: Three types of recrystallisation mechanisms [61].

DDRX is common in materials with low SFE whereby heterogeneous nucleation of new strain-free grains occurs and grow solely at the expense of high dislocation density grains, as shown in Figure 2.6 [63]. Unless otherwise specified, DRX refers in general to DDRX. CDRX occurs at larger deformations when polygonised subgrain structures with low angle grain boundaries (LAGBs) evolve into high angle grain boundaries (HAGBs) as a result of progressive subgrains rotations as shown in Figure 2.7 [61, 63]. CDRX is mostly observed in high SFE materials. CDRX is characterised by slower kinetics compared to DDRX because the formation of a CDRX microstructure requires large strains, [52, 61, 63].

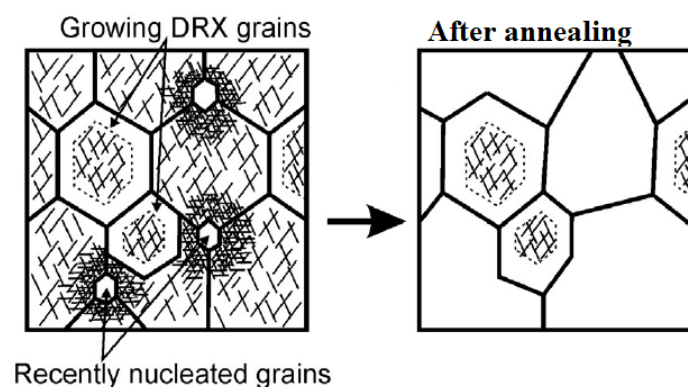


Figure 2.6: Schematic illustration of discontinuous dynamic recrystallisation [63].

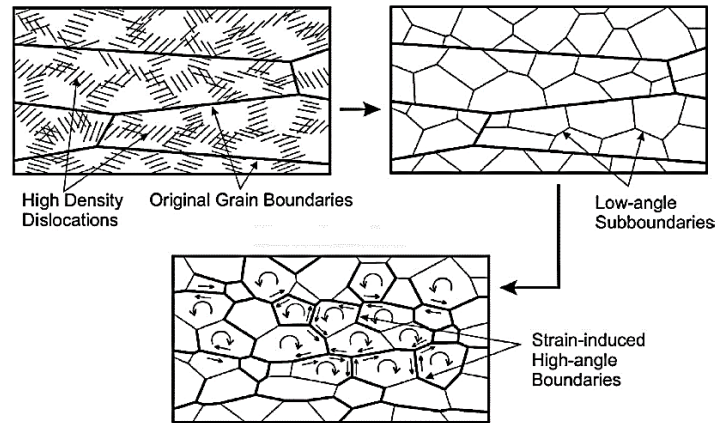


Figure 2.7: Schematic illustration of continuous dynamic recrystallisation [63].

The least researched mechanism, GDRX, is associated with larger strains and higher temperatures [63] whereby extensive grain refinement is due to grain elongation and thinning. Unlike in CDRX, during GDRX both original and strain-induced HABs are rotated into the rolling plane and the HAB spacing decreases with increasing strain (Figure 2.8) [61, 63]. However, a fibrous microstructure can form should HAGB migration not occur. Serration (wave-like character) at the HAGBs is critical for occurrence of GDRX [61].

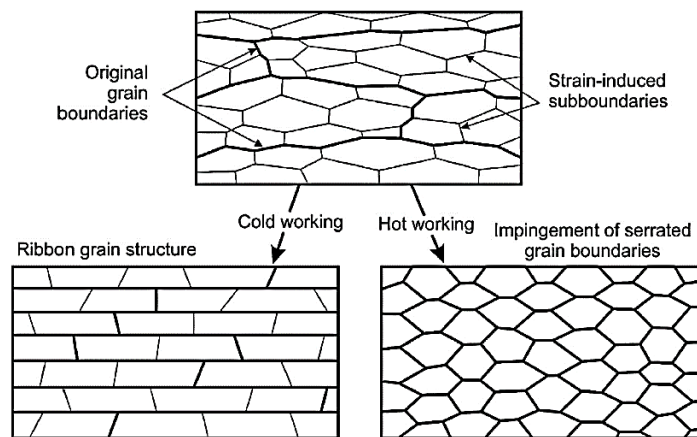


Figure 2.8: Schematic illustration of geometric dynamic recrystallisation [63].

2.3.5 Factors affecting dynamic recrystallisation

Stacking fault energy

Stacking fault energy (SFE) is an important factor when discussing softening mechanisms, because it greatly affects the dislocation mobility. Low SFE enhances dislocation dissociation into partial dislocations which hinders the climb and cross-slip of dislocations [57]. This is because the partial dislocations repel each other, and they are bound together by SFE, hence the lower the SFE, the greater the separation distance. Therefore, the wider they will spread and the more difficult it will become for them to come together and form a unit, so they can cross-slip. This explains the association of DRX with SFE.

Initial grain size

Grain boundaries affect physical, chemical and mechanical properties of crystalline solids, including: electrical and thermal conductivity, thermal coarsening, corrosion resistance, impurity segregation, hydrogen embrittlement, stress corrosion cracking, strength and ductility [64]. However, this section will only cover the relationship between grain boundaries and hot deformation. The yield stress increases with decreased grain size (the Hall-Petch effect [65, 66]) because dislocation pile-ups in fine-grained material contain fewer dislocations. The stress at the tip of the pile-up decreases and thus larger applied stress is required to generate dislocations in the adjacent grain [67]. The grain size can only be reduced to a certain critical size, approximately 10 nm. Further reduction will have the opposite effect thus reduce the material strength, known as the inverse Hall-Petch effect [67]. This is due to the fact that small grains are unable to support dislocation pile-ups.

Anything that tampers with dislocations mobility affects the DRX processes. Large initial grain sizes slow the recrystallisation kinetics because there are fewer grain boundaries to serve as nucleation sites [67]. Finer initial grain sizes accelerate the kinetics and the steady state stress is reached faster. On the other hand, large grains favour the formation of deformation shear bands which are also nucleation sites.

Sakai and Jonas [59] did an extensive study on the effect of the initial grain size on the shape of the flow curves. Multiple peaks were observed during grain coarsening or when grain refinement produced less than a 2:1 reduction in grain size. In the same manner, a single peak was observed when the grain refinement ratio was about 2:1. They associated a peak with a complete cycle of recrystallisation. Therefore, a single peak curve implies that the

deformation conditions were satisfactory to attain an equilibrium grain size, which normally happens at high strain rates and lower temperatures. Conversely, multiple peaks show that each recrystallisation cycle produced grain coarsening until the stable grain size was attained. Thus, equilibrium was established and associated with high temperatures and low strain rates.

Thermo-mechanical processing conditions

The hot forming processes cannot be discussed in the absence of the thermo-mechanical processing (TMP) conditions: deformation strain rate, temperature and total strain. The key TMP conditions are deformation strain rate and temperature which are kept constant throughout the DRX process. From the discussion on the effect of initial grain size, the recrystallized grain size at steady state is not linked to the initial grain size but deformation temperature and strain rate. This implies that for as long as these TMP conditions are the same, the steady state grain size should be the same for a given material with different initial grain sizes. Thermally activated stored energy developed during deformation is the driving force for the occurrence of the DRX and the other abovementioned phenomena observed during hot deformation [52]. A common empirical formula to incorporate the deformation activation energy, strain rate and temperature into a single parameter was developed using the Arrhenius equation and is called the temperature modified strain rate, or Zener-Hollomon parameter (Z) in s^{-1} [68]:

$$Z = \dot{\epsilon} \exp\left(\frac{Q}{RT}\right) \dots \dots \dots [2.4]$$

where:

$\dot{\epsilon}$ is the deformation strain rate,

T is deformation temperature (K),

R is the gas constant, and

Q is the deformation activation energy in kJ/mol.

The activation energy must be overcome for the nucleation and growth of a new surface or grain boundary to occur [52]. A low value of Z corresponds to high temperature and strain rate whilst high Z corresponds to low temperature and high strain rate [61]. Multiple and single peaks on the flow curves are associated with low Z and high Z respectively. The steady state subgrain size decreases with increasing Z [61].

Composition

Second phase particles play a critical role in recrystallisation. Precipitation of second phase particles act as lattice impurities, which causes strain that interacts with dislocation strain fields and hinders dislocation motion, thus slowing down the recrystallisation and grain growth. On the contrary, coarse second phase particles can promote recrystallisation by particle simulated nucleation (PSD) due to the large amount of stored energy in the deformation zone. However there is not enough evidence supporting the PSD occurrence during DRX [61]. Sakai *et al.* [63] found that increasing solute content broadened the flow stress peak and increased the peak stress and strain. The oscillations on the flow curves were found to disappear with increased concentration of the alloying elements [63]. Thus, alloying elements stabilise the microstructure and suppress the grain growth. In general, the effect of second phase particles on DRX depends on whether they exist before, during or after the completion of recrystallisation [63].

2.3.6 Hot forming behaviour of 9% Cr ferritic-martensitic steels

The 9% Cr ferritic-martensitic steels owe their application especially in the energy industry to their elevated temperature properties [69]. Good formability is ascribed to the occurrence of dynamic recrystallisation and dynamic recovery whereas poor formability is attributed to other phenomena such as hot shortness, dynamic strain ageing, localized deformation, cavitation, formation of new phases. Generally, a homogeneous microstructure is desired for defect free formed products [69]. It is therefore important to establish optimum forming conditions which require good combinations of deformation strain rate and temperature as formerly discussed. The optimisation of the hot forming processes is done on a laboratory scale and the common experimental tests performed are compression, tension and torsion. Similarly, although other 9% Cr ferritic-martensitic steels are briefly discussed, the focus is on ASTM grade P92.

Compression tests are used in the simulation of metal forming processes such as forging and rolling. In this process, the force is applied to the surface of the workpiece and the metal flows at right angles to the direction of compression [70]. Hot compression tests have been used to understand the effect of deformation conditions on 9% Cr ferritic-martensitic steels in

the deformation temperature range 600 - 1250 °C, strain rates of 10^{-2} - 20 s^{-1} and true strain of 0.05-0.9 [69, 71-75].

The activation energy indicates the degree of difficulty for plastic deformation to occur, and is sensitive to slight changes in the composition [33,76]. Liu and Yan [73] and Shi and Liu [74] studied P92 steels in the range of 900 - 1250 °C and calculated activation energies of 499 and 437 kJ/mol as presented in Table 2.3. The difference in activation energy can be attributed to the difference in composition. The activation energy increases with increased alloying element concentration as they form stronger retarding effects on DRX [77]. This indicates that the activation energy for every different P92 steel composition must be determined and cannot be generalised based on the previous work.

The effect of deformation amount or true strain on DRX in P92 steel was studied by Shi and Liu [74] in the temperature range 900 - 1250 °C. Complete DRX was achieved at a true strain of 0.9, as shown in the $\ln Z$ - true strain diagram (Figure 2.9) [74]. This behaviour is explained by the modified Avrami equation which shows that as the true strain increases, the DRX volume fraction increases [52].

The effect of deformation temperature and strain rate behaviour combined via the Zener-Hollomon parameter, Z , has been studied for P92 steel. Complete DRX occurred at low Z values, with temperatures above 1100 °C and the strain rate below 0.1 s^{-1} [72-74]. Shi and Liu [74] calculated the natural log of the critical Z value above which DRX would not occur in P92 steel to be $\ln(42.9)$. It was further discovered that for a given Z , the tendency for DRX became stronger with increased true strain. On the other hand, for a given true strain, the tendency of DRX weakened with increased Z [71, 74].

Table 2.3: Effect of composition on activation energy in steel P92.

Elements	Composition (wt%)	
C	0.10	0.097
Mn	0.45	0.5
S	0.01	0.005
Si	0.4	0.34
P	0.02	0.008
Cr	9	8.87
W	1.7	1.82
Mo	0.45	0.48
V	0.2	0.2
Nb	0.05	0.076
N	0.05	0.058
B	0.003	0.0032
Ni	0.4	0.27
Al	0.004	-
Activation energy	499 kJ/mol [73]	437 kJ/mol [74]

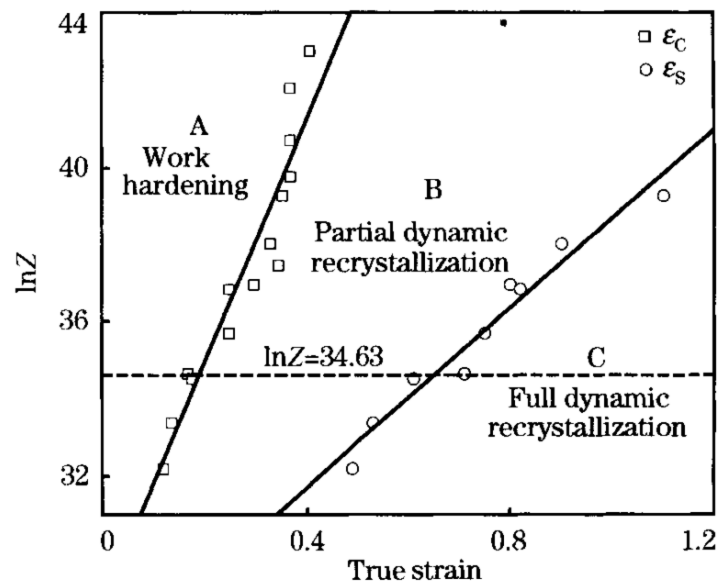


Figure 2.9: Effect of true strain on $\ln Z$ for P92 steel [74].

2.3.7 Microstructural evolution of 9% Cr ferritic-martensitic steels at high temperatures

The target microstructure for 9-12% Cr steels is fully martensitic without delta ferrite and this is achieved by balancing the ferrite and austenite stabilisers [27]. The overall microstructures of the 9-12% Cr steels look similar, therefore their difference in properties can be attributed to their distinct alloy compositions and processes [78-80]. Figure 2.10 [81] shows the heat treated microstructure of P92 steel, which is characterised by tempered martensite decorated with precipitates of Cr, Fe, W, and Mo rich $M_{23}C_6$ carbides on the grain boundaries, whilst fine vanadium and niobium rich MX carbonitrides are dispersed in the intra-lath regions [59, 78, 79]. This is an ideal structure that the material needs to maintain throughout its service life. For the steel to maintain the good strength, the factors to be considered include the type, size and distribution of the secondary phases, as well as the nature of the matrix microstructure [79].

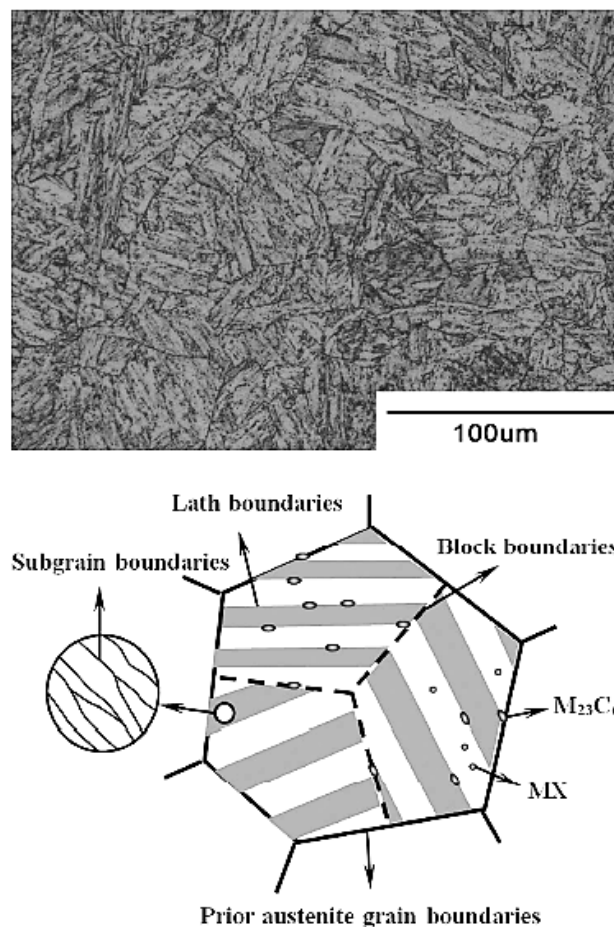


Figure 2.10: As-tempered microstructure of P92 before service [81].

It is a common concern that materials at elevated temperatures tend to become unstable and fail due to creep and fatigue. An effective stress is responsible for plastic deformation at high temperatures [82]. A stable structure is therefore required to provide long-term resistance against plastic deformation, thus giving superior creep and fatigue resistance. Figure 2.11 [82] shows how the microstructure in Figure 2.10 would evolve when exposed to higher temperature for a longer period. During the microstructural evolution, the original precipitates coarsen and some dissolve, while some unwanted precipitates form. These alterations in the microstructure reduce the inner stresses and reduce the good mechanical properties, causing deterioration of fatigue and creep strength of the material [79, 82]. These undesired new precipitates are briefly described.

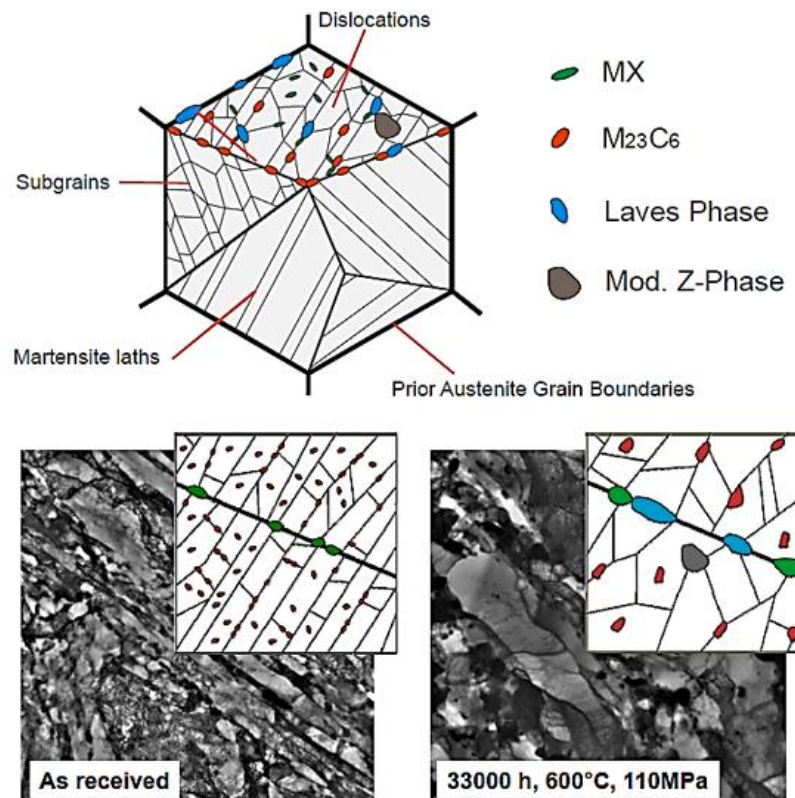


Figure 2.11: Microstructure evolution at high temperature [82].

2.3.8 Precipitates in 9% Cr martensitic ferritic steels

$M_{23}C_6$

$M_{23}C_6$ (M = Cr, Fe, W) carbides are one of the two main precipitate types in CSEF steels [83]. They form preferably on grain boundaries with a high dislocation density and can therefore hinder grain boundary movement. $M_{23}C_6$ particles are large and play a critical role in controlling the subgrain coarsening [83, 84].

MX

The second type of the main precipitates in CSEF are small particles of MX carbonitride (M= V, Nb; X = C, N). Their preferential precipitation sites are within the lath grains [83]. They sporadically occur on the subgrain boundaries. MX are more beneficial than $M_{23}C_6$ because they precipitate finely and densely and act as obstacles to migrating subgrain boundaries by pinning them [85]. Even though the growth rate of MX particles can be enhanced by creep deformation, these particles are much more stable, thus their chemical composition and size do not show a significant change after long term thermal exposure [86].

Laves phase

The Laves phase is an intermetallic phase with the empirical formula AB_2 , e.g. Fe_2W , Fe_2Mo , $(Fe,Cr)_2(W,Mo)$ [83]. The Laves phase growth mechanism is governed by W and Mo atoms diffusion to grain boundaries. They form at the expense of W and Mo dissolved in the ferrite matrix phase, thus reducing the solid solution strengthening effect [39, 85]. The Laves phase starts precipitating when there is high concentration of W and Mo. Laves phase nucleate and grow on the $M_{23}C_6$ carbides [80].

Z-phase

There are two forms of this phase: Z-phase (original) and the modified Z-phase [83]. The crystal structure of the CrNbN Z-phase is tetragonal and the modified $Cr_2(V,Nb)_2N_2$ Z-phase is cubic. Z-phase precipitates decrease the creep strength, because they form at the expense of MX particles suppressing MX precipitation hardening [87]. While fine MN nitrides contribute to creep strength, the coarse Z-phase particles do not, and their formation is the major cause of premature creep strength loss [49, 88].

2.4 Heat treatment

2.4.1 Fundamental concepts in steel heat treatment

Heat treatment is a series of heating and cooling operations, timed and designed to produce the desired microstructure and thus the properties of metals or alloys [57, 89]. The controlled mechanical properties are hardness, ductility, strength, and toughness. The heat treatment process variables are temperature, holding time, heating rate, cooling rate and furnace atmosphere.

The heating and cooling rates are important factors in heat treatment of steels. The cooling rate determines the final structure (Figure 2.12) [89], and slow heating rate allows for structural equilibrium at the maximum temperature [89]. Time-temperature transformation diagrams play a key role in identifying a suitable heat treatment process that will produce a desired microstructure and hardness. Basic heat treatments of steels are annealing, hardening, normalising, and tempering.

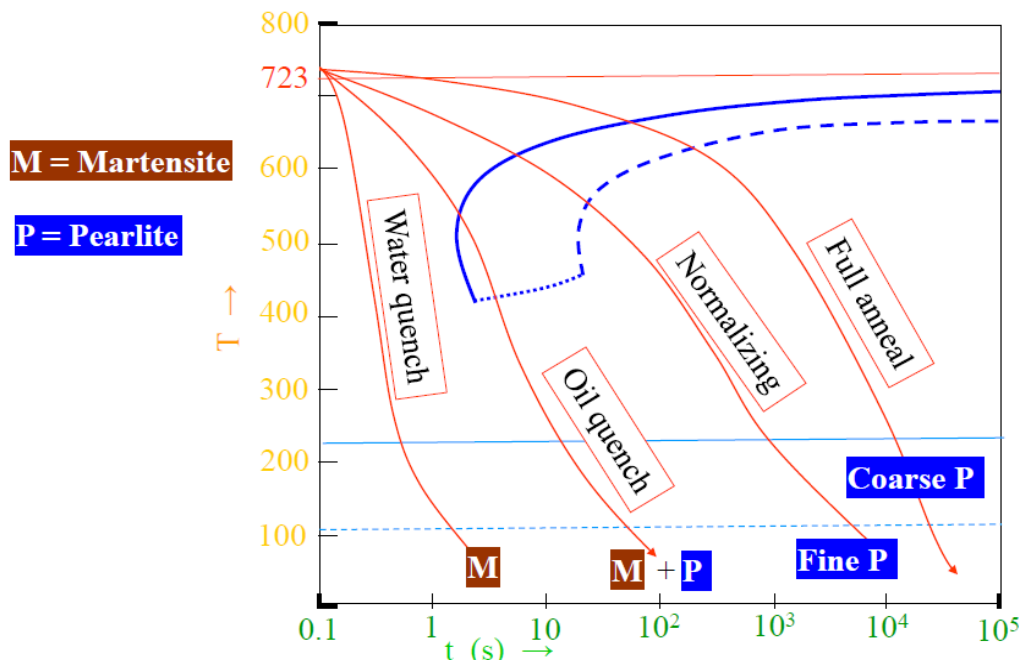


Figure 2.12: Different cooling treatments [89].

2.4.2 Effect of heat treatment on P92 steels

Dipika *et al.* [90] studied the heat treatment of P92 steel. Grain boundaries are the nucleation sites for precipitates and decreasing grain size promotes precipitation. The area fraction of the precipitates decreases with increased normalizing temperature and increases with increased tempering temperature. Higher normalizing temperature increases the precipitate dissolution [91]. Lower normalizing temperature and higher tempering temperature produce straight grain boundaries due to resistance to grain boundary movement offered by more precipitates. The high normalising temperature increases the lath size while it causes no significant change in precipitate sizes [90]. On the other hand, both lath width and small precipitate size increase with increased tempering temperature.

The hardness decreased with increased normalizing temperature due to increased grain size [90, 92]. However, lower precipitation of carbides at higher normalising temperature can result in more carbon retained in the matrix which leads to increased hardness. Hardness decreases with increased tempering temperature due to increased lath size, precipitate size, area fraction of precipitates and subgrain formation with decrease in dislocation density [90].

Continuous Cooling Transformations (CCT) diagrams provide insight in understanding the transformation behaviour of steels. The CCT diagrams enable for extraction of parameters that characterize transformation behaviour [91]. Critical cooling rates for martensite and ferrite can be extracted from CTT diagrams. Figure 2.13 [92] shows a CCT diagram for P92 steel.

2.5 Thermodynamic calculations

2.5.1 Software general description

Simulations are necessary to understand how a certain process is affected by the change in one or more of its parameters. Software have been constantly developed to carry out the simulations including in thermodynamics. Thermo-Calc is a powerful and flexible software and database package initially designed for complex multi-component systems and can be applied to any thermodynamic system in the fields of chemistry, metallurgy, material science, etc. [93]. Calculations performed by Thermo-Calc include phase diagrams (using the CALPHAD (CALculation of PHase Diagram) method [94]), Pourbaix diagrams and phase proportion diagrams (called “property diagrams” in Thermo-Calc). Thermodynamic databases have been developed for Thermo-Calc to be applied in different groups of materials and alloys. CALPHAD “*is a phase-based approach, whereby the thermodynamic properties*

of each phase are described through the Gibbs free energy, which is evaluated through a critical assessment of all experimental and theoretical information available on phase equilibria and thermochemical properties in a system” [94].

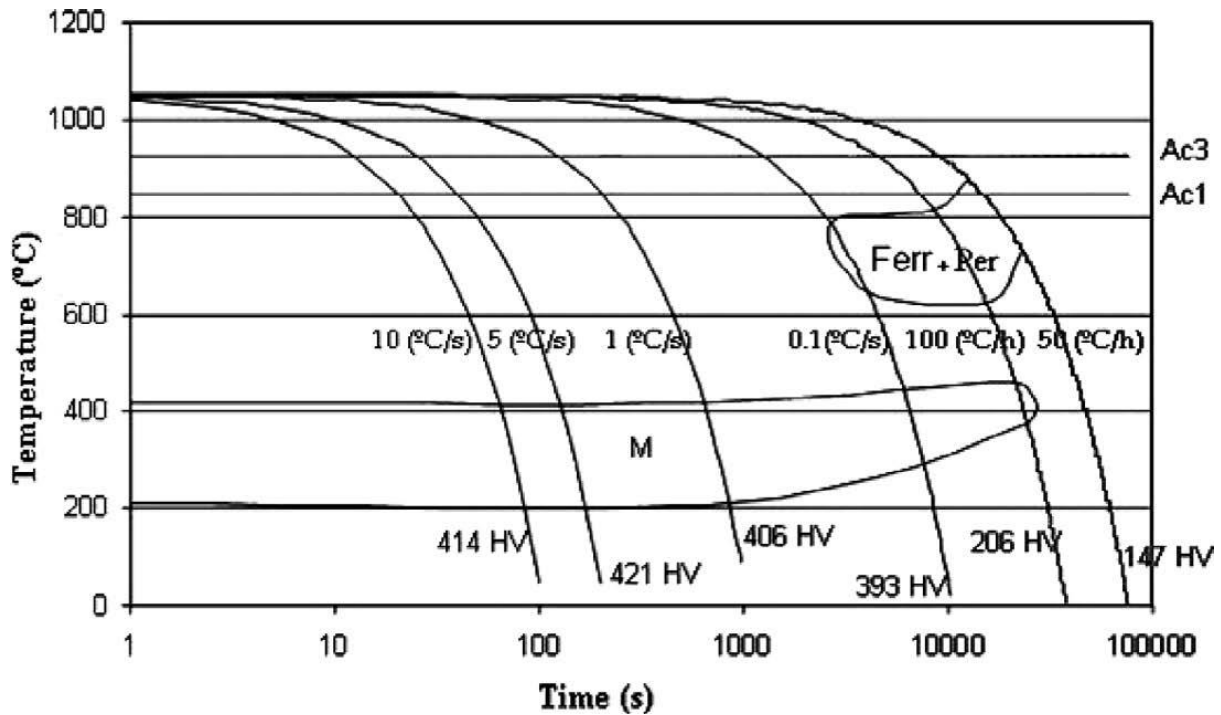


Figure 2.13: CCT diagram for P92 Steel [92].

The databases used depends on the analysed material for an example, TCAL database is for aluminium alloys and TCFE5 is for steels [93]. In thermodynamic databases phases usually have generic phase names, for their structure rather than composition e.g., BCC_A2, BCC_B2, and FCC_A1 (Figure 2.13) [95]. However, if there is a phase with same structure but different composition, the symbol # is used to differentiate them e.g., FCC_A1#1 and FCC_A1#2 signifying Austenite and MX respectively [95].

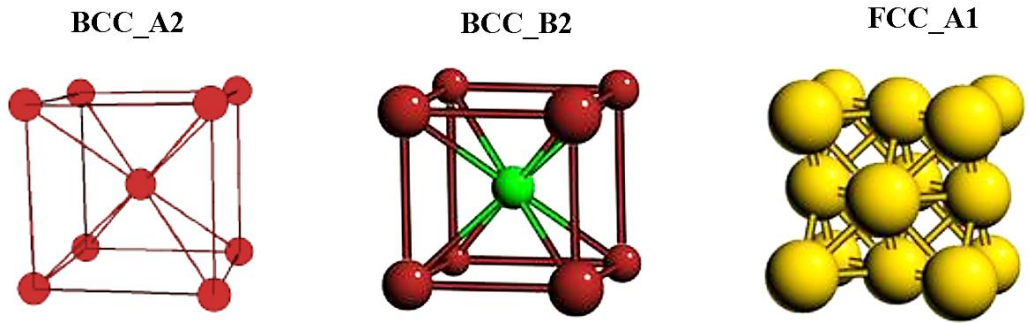


Figure 2.14: Phase Structures [95].

2.5.2 Application of Thermo-Calc software

Thermo-Calc helps to predict possible phases and their proportions in materials for a given chemical composition and temperature. The phase proportion data can be used to understand the microstructure and properties of the material. Another important application of Thermo-Calc is to provide material data that is missing in the handbook data [96]. Figure 2.14 shows a property diagram for a P91 steel which is an example of Thermo-Calc application in CSEF steels.

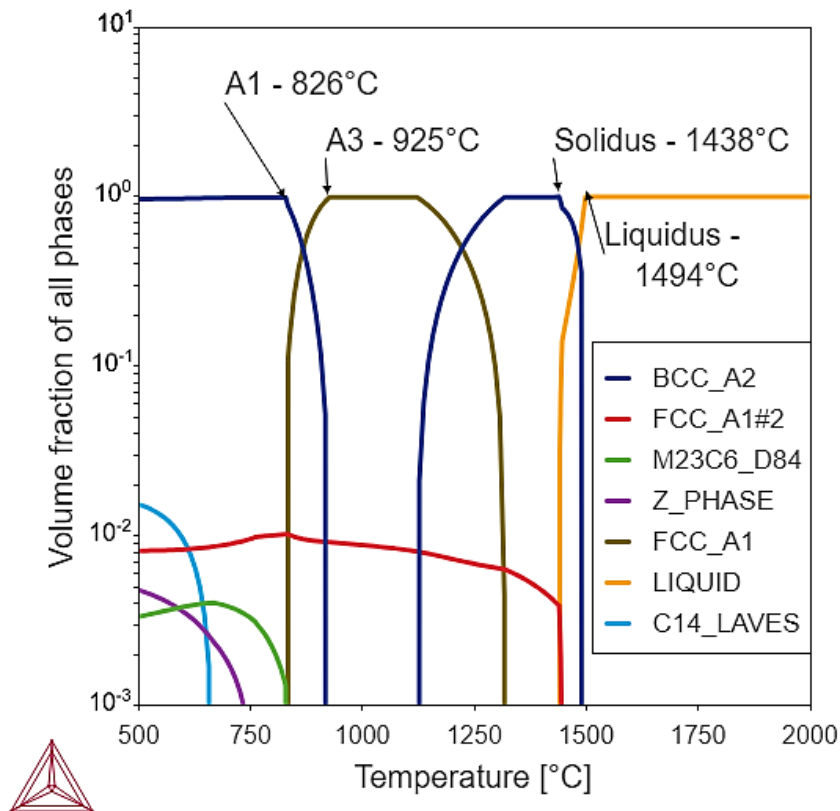


Figure 2.15: Phase proportion diagram for P91 [96].

2.6 Friction Hydro-Pillar Processing (FHPP)

2.6.1 Friction hydro-pillar processing overview

Delany *et al.* [97] described the FHPP process as “*a technique that involves rotating a consumable rod co-axially in a circular hole, under an applied load to continuously generate a plasticised layer.*”

FHPP is an emerging friction welding technique which was developed from the concept of rotary friction welding [98]. Figure 2.12 [1] shows some available friction welding techniques. FHPP was developed and patented in the United Kingdom (UK) by The Welding Institute (TWI - World Centre for Materials Joining Technology) led by Dr Wayne Thomas in the early 1990s.

FHPP is a novel technique that involves drilling a hole in the thick-walled metal structure containing a previous discontinuity such as crack and refilling the hole with an external stud (consumable rod). As a variant of friction welding processes, this technique uses an advantage of the energy conversion of mechanical to thermal energy caused by friction [99-102]. The thermal energy is sufficient to form a solid-state bond between the stud and the metal substrate. FHPP can further be categorised as a hot working process whereby a large amount of deformation is experienced by faying surfaces (surfaces in contact).

In the FHPP process, the consumable rod is fully plasticised across the bored hole at a rate faster than the consumable feed so the frictional rubbing surface rises along the length of the rod, which forms dynamically recrystallised deposit material. The joint is achieved as a result of hydrostatic forces, and the amount of the deposited material is usually greater than the feed material. The excess plasticised material, called flash, is removed at the end of the process to achieve an even, smooth surface. Figure 2.13 [1] schematically shows the FHPP process.

2.6.2 Terminology associated with FHPP

As FHPP terminology is not well defined, some terms are used interchangeably by different authors. The FHPP variants described by Meyer [103] are:

- **Friction Tapered Plug Welding (FTPW):** Friction tapered plug welding is a friction welding process where a through-thickness hole is closed by friction welding a rotational welding consumable to the sides of the hole. The welding consumable is only plasticised

near the surfaces and not across the whole diameter. Usually, a tapered configuration for the consumables (plug) and the hole is used.

- **Friction Stitch Welding (FSW):** Friction stitch welding is the application of the FHPP process where several FHPP welds are performed along a welding path, overlapping each other for a given distance. The bore hole for the following weld is drilled partially in the consumable stud of the prior weld. It is used for the repair of longer cracks and joining plates with longer welding seams.
- **Friction Tapered Stitch Welding (FTSW):** FTSW is stitch welding with tapered holes and welding consumables.
- **Friction Stud Welding (FSW):** FSW is a friction welding process where a single rotational stud is welded on the surface of a workpiece.

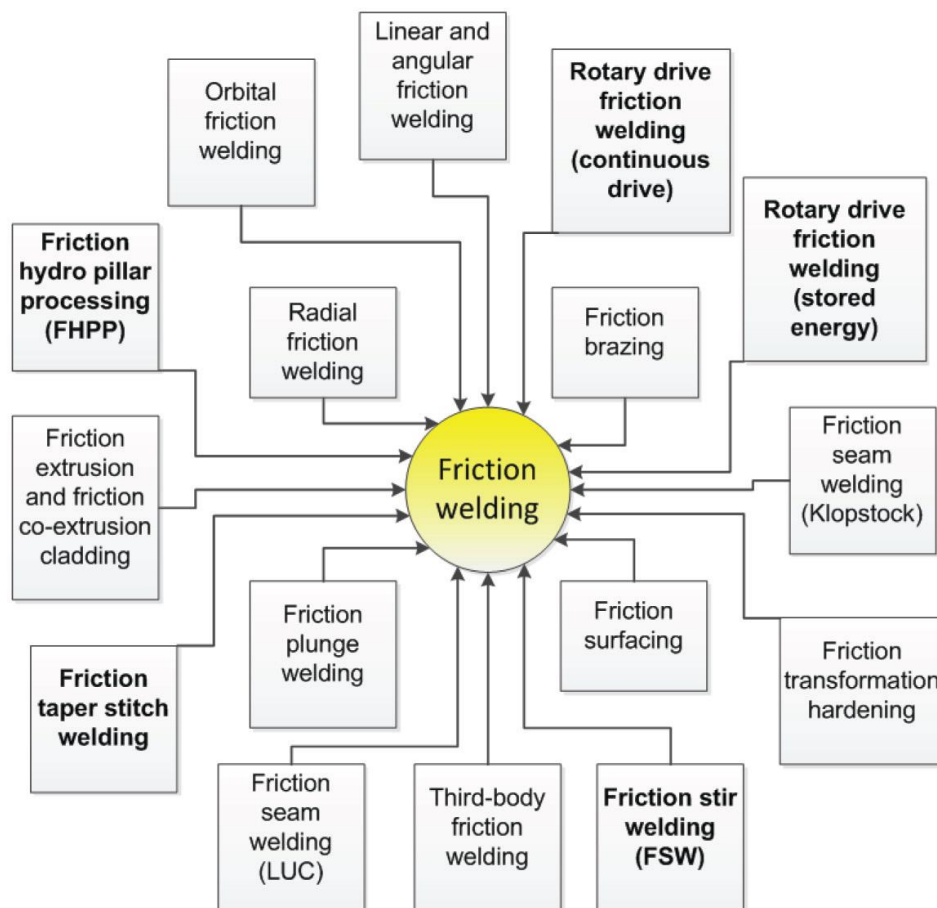


Figure 2.16: Friction welding technologies [1].

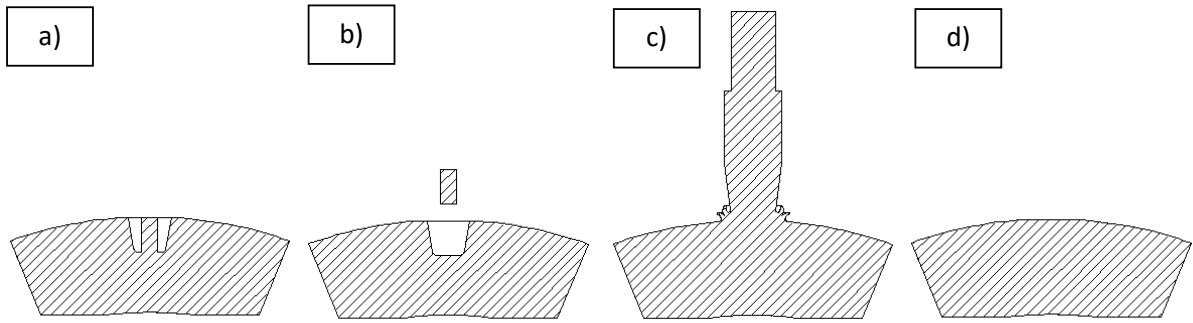


Figure 2.17: Coring and tapered hole preparation process: a) cylindrical core sample is machined, b) core sample is removed, c) FHPP weld is performed, d) stud and flash are removed [102].

2.6.3 The FHPP hole configurations and process stages

The difference in the process descriptions is mainly guided by the geometry of the consumable rod and the pre-machined hole. The two main and common geometries employed are parallel/straight and tapered as shown in Figure 2.14 [104].

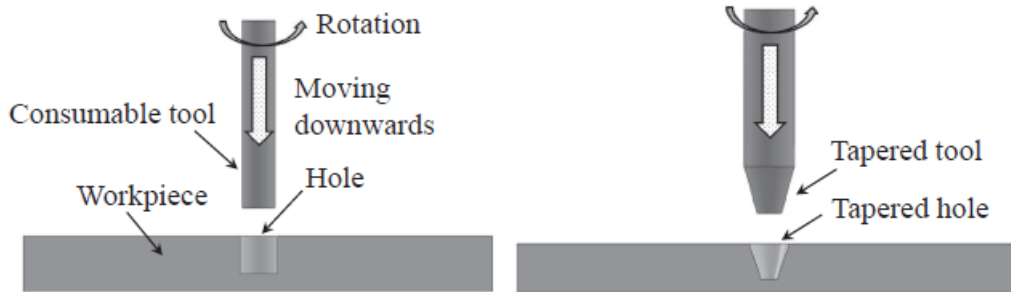


Figure 2.18: Stud and hole configurations in FHPP [104].

- **Parallel/straight configuration:** The parallel/straight configuration prevents defects such as lack of filling. However, as the chamfered edges at the bottom of the hole cause stress concentration and void-like defects, a tapered configuration is widely applied [104].
- **Tapered configuration:** With the tapered configuration, the contact area is increased, which effectively cause friction between the faying surfaces. This ultimately eases the flow of the plasticised material, which then yields a defect free joint [104].

FHPP process stages

FHPP can be summarised into three sequential stages as illustrated in Figure 2.15 [105].

1st stage - Dwell

The external rotating stud is pressed into a pre-machined hole to fully open it which results in frictional heating along the stud. The temperature increase at the interface of the faying surfaces decreases the yield strength which favours the plastic flow of the base/substrate metal and the stud.

2nd stage - Burn-off

The rotating stud is forced into the hole resulting in plastic flow of the stud material through the stud-hole clearance. During this stage, plasticised stud material fills through the stud-hole clearance with the excess coming out of the hole which is referred to as flash. The burn-off describes the length of the rod consumed during the welding and determines the outcome of the process.

3rd stage - Forging

At this point, the hole is filled. The rotational motion of the stud is stopped and the force is increased to promote a solid-state bond between the stud and the base metal.

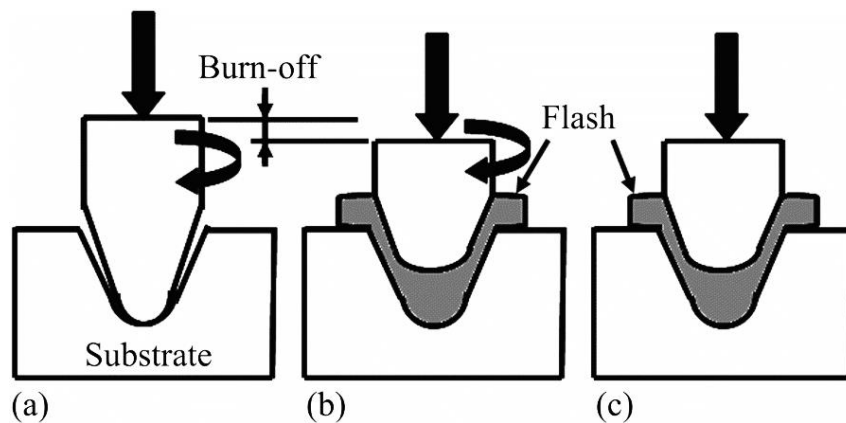


Figure 2.19: FHPP stages a) dwell, (b) burn-off and (c) forging [105].

Figures 2.16 [1] and 2.17 [2] show how the microstructures of the rod and the base material change during FHPP processing. The difference in heat input and strains, strain rates experienced during FHPP process result in a multi layered structure. The generated heat creates a heat affected zone (HAZ) region on both base and rod materials. Similarly, the

experienced strains and strain rates created a highly deformed region on both materials termed thermo-mechanically affected zone (TMAZ). Another region that forms is the interface, which is the bonding point of the rod and the base material.

2.6.4 Effect of FHPP process variables on the weld structure and material properties

Axial force, forging force, rotational speed and burn-off are the main variables that can be controlled in FHPP, to give the optimal combination of temperature and pressure to form the weld [7, 10]. The axial force ensures an appropriate bond through heat generation while the rotational speed ensures the appropriate mixing between the base metal and the consumable rod to give a defect free joint. These factors associated with burn-off determine the welding duration. There are reviews of some FHPP done on various materials [2-4, 10, 106, 107], but there was no available literature on the investigated steel, P92, or its family of creep strength enhanced ferritic steels.

FHPP of ASTM A36 steel was done to understand the relationship between some process variables and their effects on the weld properties [105]. Longer processing time, lower stud force and longer burn-off length resulted in the highest peak temperatures and low temperature gradients. A more uniform hardness distribution was achieved under this set of conditions.

Yeh *et al.* [4] investigated the influence of axial forces on ASTM A36 steel processed by FHPP. Depending on the region, the observed inclusions were: flattened, clustered or isolated, or deformed and oriented in the direction of the material flow. The flattening was attributed to the processing and post processing axial forces. The consumable material at the central lower region experienced rotational deformation rather than a series of shear interfaces. The higher forces shortened the processing time and decreased the heat input with a higher temperature gradient.

Chludzinski *et al.* [10] studied the FHPP of C-Mn steel. Higher axial forces decreased the peak temperatures and shortened the processing time. The higher forces produced fewer inclusions.

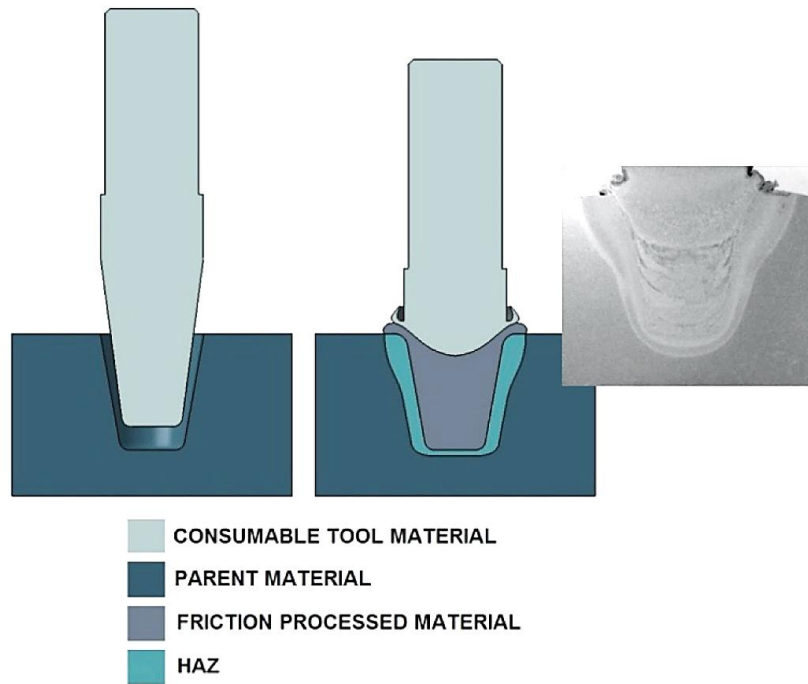


Figure 2.20: Schematic diagram of the FHPP process with macrograph of a weld cross-section [1].

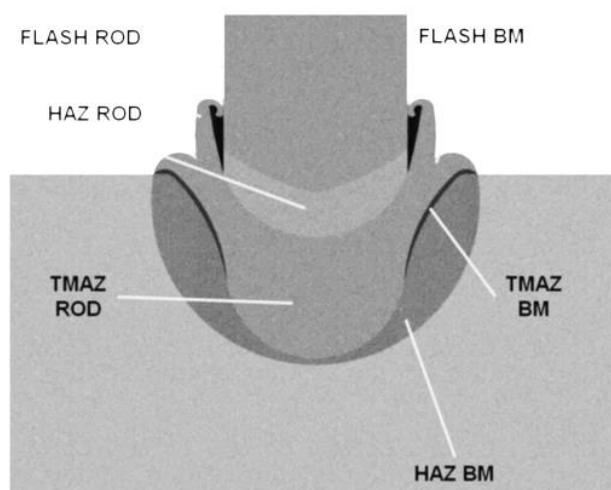


Figure 2.21: Region characteristics of the FHPP weld: base material (BM), heat affected zone (HAZ) and thermo-mechanically affected zone (TMAZ) [2].

FHPP of SAF2205 duplex stainless steel was studied by Rodrigo *et al.* [3]. There was a hardness increase between the mixing zone and the thermo-mechanically affected zone. This shows some material strengthening during FHPP. Three main strengthening mechanisms proposed were: strain hardening, decreasing grain size and microstructural transformation.

Meinhardt *et al.* [106] produced a weld without discontinuities or cracks in FHPP of the duplex stainless steel UNS S31803. Microstructural refinement increased the weld hardness relative to the base material. The FHPP weld maintained the proportion of microstructural phases required by the specification for equipment used in oil and natural gas production (EN ISO 15156-3). Similar to the results of Chludzinski *et al.* [10], FHPP did not have any negative effect on corrosion resistance or fracture toughness.

From Thomas *et al.* [107] and Thomas and Nicholas [108], FHPP has not been detrimental to the mechanical properties of the weld zone, due to homogenising and refining of the microstructure, as shown for a nickel Al-bronze in Figure 2.18 [107]. This behaviour is attributed to the extensive working of the softened material during the processing operation.

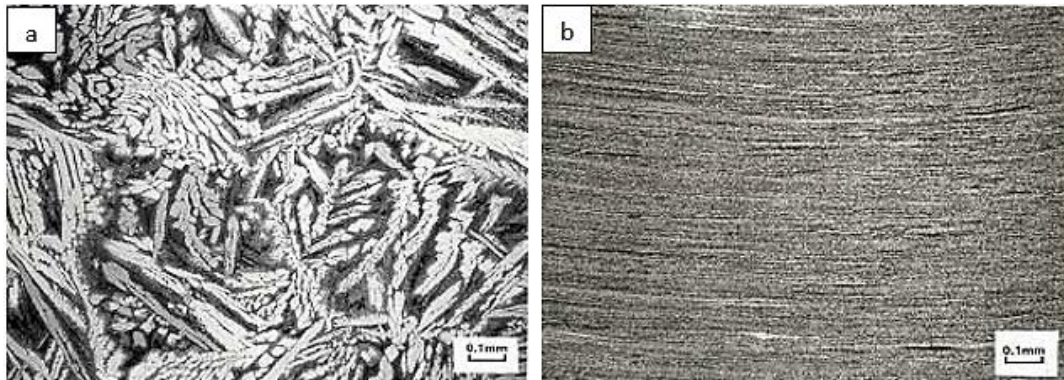


Figure 2.22: Nickel aluminium : a) as-cast and b) same material after FHPP processing [107].

2.7 Rational of the project

The application of P92 steel in ultra super critical power plants will play a large role in preserving coal resource as this utilises less coal for equivalent power output. Therefore, being able to fix the cracked P92 pipes *in situ* with FHPP process will not only save money for pipe replacement but also the time lost on shutdowns.

With no work found on the FHPP of P92 steel and little work done on analysis of FHPP welds microstructure, this research contributed to the body of knowledge in this regard. Having more information available on the process application on P92 steel will assist in improving its applications and making it the material of preference.

Chapter 3 :Experimental procedure

The experimental and characterisation techniques used in this research project are discussed in this chapter. Standard procedures were followed unless otherwise stated, and where necessary, modifications to the standard procedures were made to suit the required application.

3.1 Materials

An ASTM grade P92 steel pipe sample and a cross-section of a FHPP weld sample were received from eNTSA at Nelson Mandela University (NMU). The as-received samples were sent for chemical analysis to Scrooby's Laboratory Services, which is approved by the South African National Accreditation System (SANAS). The major elements were analysed by optical emission spectrographic analysis (OES). Inductively coupled plasma atomic emission spectroscopy (ICP) was done to analyse nitrogen. Nitrogen analysis of the FHPP weld region was not done as it was not clear how deep the weld penetrated the thickness of the machined sample.

3.2 Thermodynamic calculations

Thermo-Calc uses the CALPHAD (Computer Coupling of Phase Diagrams and Thermochemistry) method [109]. The thermodynamic calculations were done using the Thermo-Calc software with the TCFE5 steels database to determine the likely phases, phase transformation temperatures, precipitate dissolution temperatures and the phase proportions for the samples (base metal, rod, and P92 pipe). The chemical compositions were input to calculate the changes in equilibrium phase proportions with temperature.

3.3 Thermomechanical testing (Uniaxial compression)

A computer controlled thermomechanical Gleeble 3500 system was used to perform the hot compression tests. Figure 3.1 shows the Gleeble chamber in which uniaxial tests were done under a vacuum environment with conditions stipulated in Table 3.1. A 'lubricant' was placed between the test specimen and the anvils to minimise friction during the test. For the

current work test temperatures, tantalum foil was used because at such high operating temperatures, graphite foil was expected to react with the tested steel. Type R thermocouples were used instead of Type K for this temperature range (1100 – 1200 °C). The tests were done in accordance with the Gleeble user guide [110].

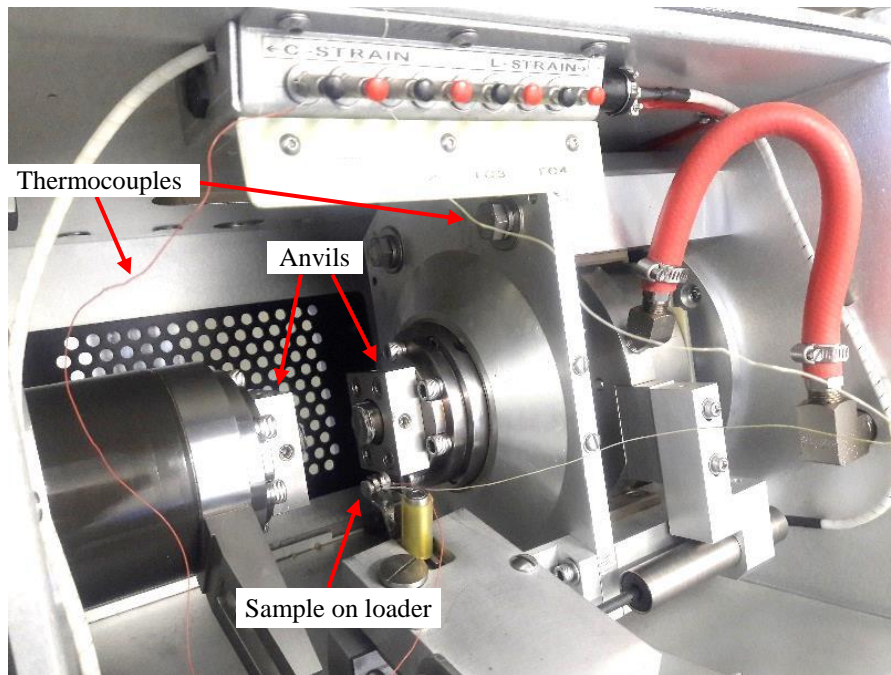


Figure 3.1: Gleeble chamber.

The available information on FHPP processing was used as a guideline to determine the test parameters for the compression tests [111, 112]. The FHPP parameters were stud force, 25kN; rotational speed, 500 rpm; and burn-off length, 9 mm.

The temperature estimation during FHPP was acquired by placing the thermocouples closer to the weld zone as shown in Figure 3.2. The thermocouples were placed at three positions with the closest one placed at about 3 mm from the edge of the weld.

The temperature profile in Figure 3.3 was measured during an FHPP run on ASTM X20 steel by eNTSA at NMU [113]. Data on P92 FHPP material was not yet available due to technical challenges in the data acquisition software of the FHPP equipment.

From Figure 3.3, the highest temperature measured during the FHPP was 1075 °C. The thermocouples were placed closer to the weld and the recorded temperatures were taken as

the benchmark to estimate the temperature at the weld region. The average heating rate from 300 °C to the maximum temperature of 1075 °C was estimated to be 25 °C.s⁻¹ and the air cooling rate to be 15 °C.s⁻¹ using Figure 3.3. The sample was given 60 s soak time at the deformation temperature to allow for temperature uniformity prior to compression.

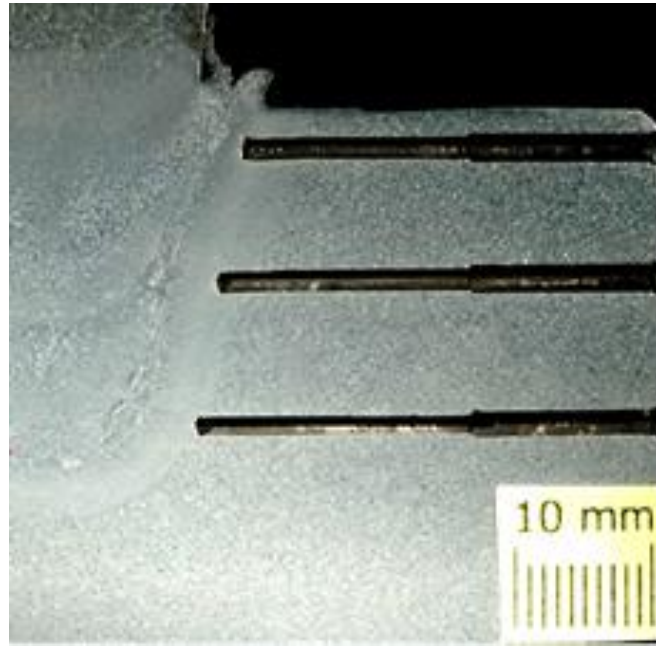


Figure 3.2: Photograph of X20 steel showing thermocouple positioning during FHPP processing.

Using Wolk [111] and Athanasios [112], since both FHPP and friction stir welding apply similar principles, strain rates of 10 and 50 s⁻¹ were used. The specimens with a diameter of 8 mm and height of 12 mm were mounted on the Gleeble sample holder. The anvils were lubricated with tantalum foil. The deformation temperatures were 1100 and 1200 °C. The strain rates were 10 and 50 s⁻¹ with strains of 0.693, 0.9702 and 1.247. The testing matrix is shown in Table 3.1. The test matrix was used for the three total strains: 0.69, 0.97 and 1.24, thus the total number of tests = (4 * 3) = 12.

Table 3.1: Uniaxial compression testing matrix.

Strain rate (s ⁻¹)	Temperature (°C)	
	1100	1200
10	#1	#2
50	#3	#4

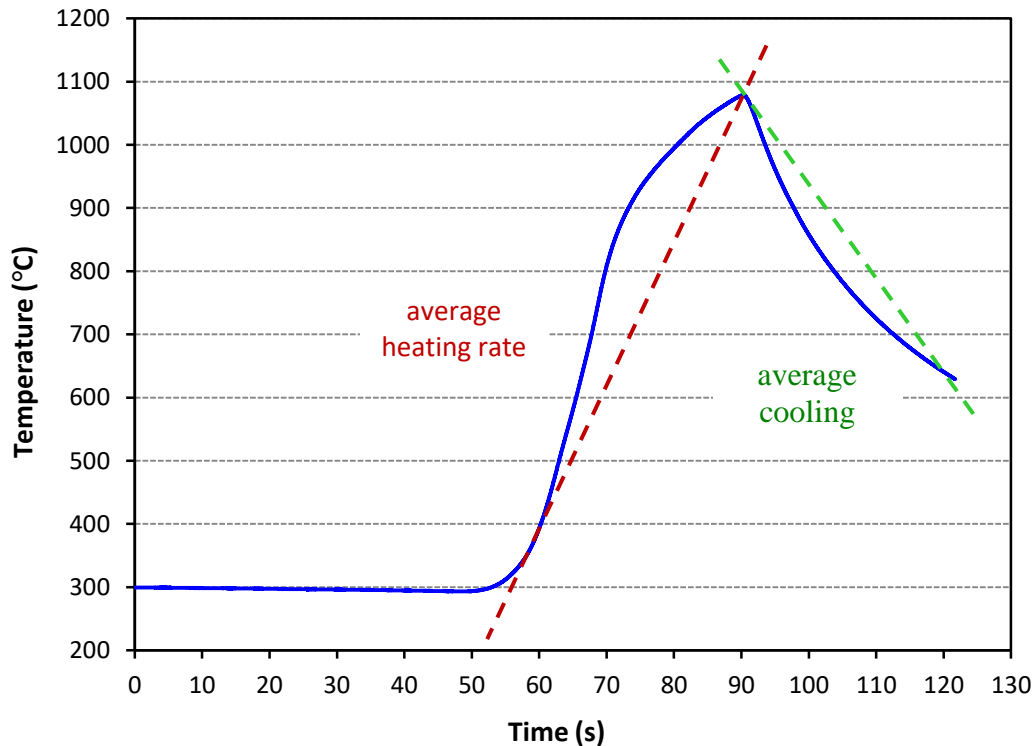


Figure 3.3: Temperature profile of X20 steel processed with FHPP (thermocouple was placed 3mm from the weld).

3.4 Heat treatment

As the FHPP weld sample had been post weld heat treated (PWHT), the same heat treatment parameters were used for the samples which were hot compressed with the Gleeble. A Carbolite tube furnace was used for the heat treatment with the following parameters:

- Heating and cooling rate: 120 °C/ h
- Soak temperature: 760 °C
- Soak times: 3 h 45 minutes or 5 h.

To compare the effect of heat treatment, including soak time, the same characterisation techniques were used for the heat treated samples as for the deformed samples: scanning electrons microscopy (SEM), optical microscopy and microhardness testing.

3.5 Material characterisation

3.5.1 Metallographic preparation

P92 pipe steel sample preparation

The provided pipe segment from Nelson Mandela University was cut using electrical discharge machining (EDM) to produce rod specimens (8 mm Ø, length 12 mm) for thermomechanical testing. After thermomechanical testing, the compressed specimens were sectioned using a diamond cut-off wheel at 3500 rpm and 0.050 mm/s feed. The cross sections of the specimens were hot mounted in PolyFast resin as it is conductive and allows for further analysis such as scanning electron microscopy (SEM).

To reveal the microstructure, the specimens were ground, polished and etched by the procedures listed in Tables 3.2 – 3.4. The different etching techniques as well as etching reagents were used to find the best method to reveal a detailed microstructure. Furthermore, these etchants were used to assess if different microstructural features could be revealed by different etchants. Figure 3.4 summarises the metallographic preparation of the pipe steel sample.

FHPP weld cross-section sample

The FHPP weld cross-section sample was sectioned using a 66A30 abrasive cut-off wheel. The sectioned segment was then hot mounted using PolyFast resin. The mounted specimen was ground and polished according to Table 3.2. Figure 3.5 shows the sectioning of the provided weld cross section. Vilella's reagent with 4 g picric acid was used to etch the specimen to reveal the distinct weld regions.

Analysis of the compressed specimens was done at the centre of the deformed surface as shown in Figure 3.4 (marked area on the mounted sample). This was done because during hot compression testing, the maximum deformation is experienced at the centre [57].

Table 3.2: Grinding and polishing steps.

Step	Polishing particle sizes	Load (N)	Speed (rpm)	Duration (min)
1	320 grit	30	300	Until plane
2	1200 grit	30	300	5-10
3	6 μm	25	150	4-7
4	3 μm	25	150	5
5	1 μm	20	150	4

Table 3.3: Electrolytic etching and the applied voltage.

Etchant	Duration (s)	Voltage (V)
Oxalic acid	40	7
Nitric acid	55	5
Potassium hydroxide	35	3
Ammonium persulfate	40	6

Table 3.4: Immersion etchants and times.

Etchant / reagent	Duration (s)
Vilella's (4g picric)	7
Murakami's	110
Kalling's	5
Marble's	4
Ferric chloride	3

3.5.2 Optical microscopy

Optical microscopy on a LEICA DM6000 M, with a LEICA DFC490 camera was done at low magnifications ($\times 50$, $\times 100$, $\times 200$, $\times 500$) and $\times 1000$ to study the microstructures of both hot compressed specimens and the weld cross section. All samples were etched before analysing.

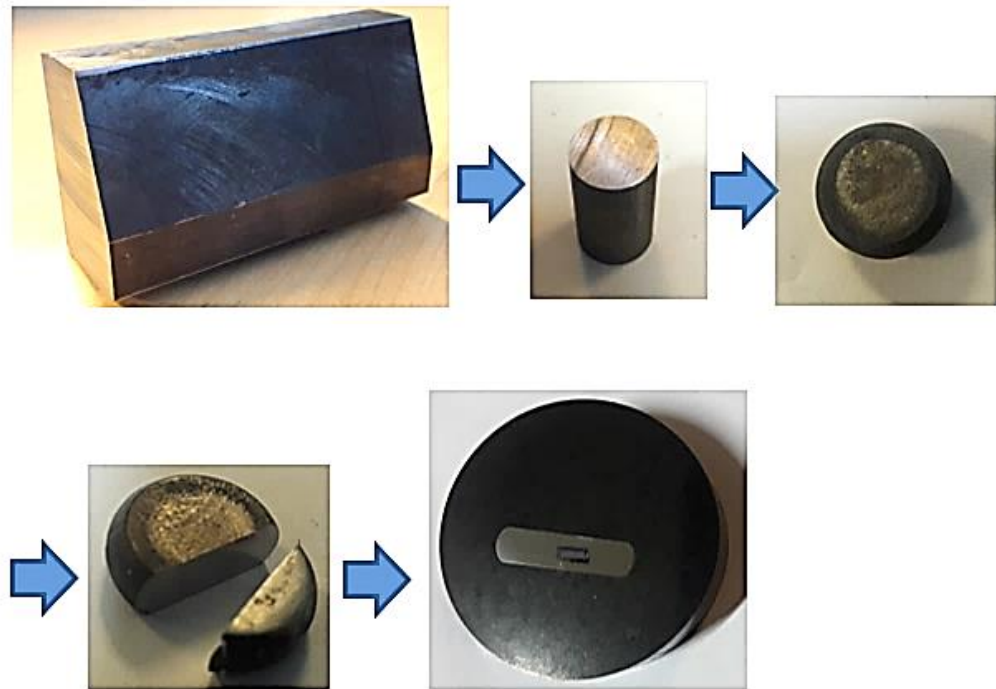


Figure 3.4: Metallographic preparation of the P92 steel samples.

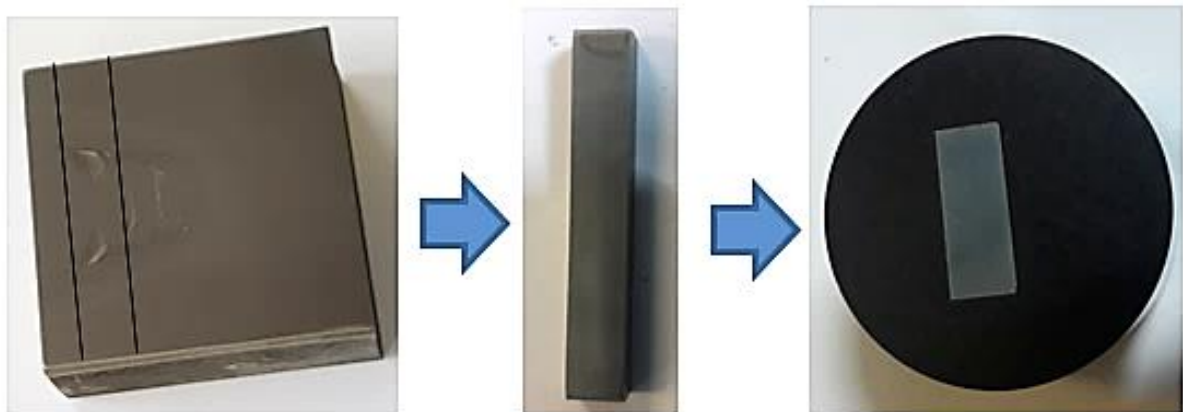


Figure 3.5: FHPP sample sectioning and mounting.

3.5.3 Scanning electron microscopy (SEM)

A Carl Zeiss Sigma field emission scanning electron microscope (FEG-SEM) coupled to an Oxford energy dispersive X-ray spectroscope (EDS) was used to characterise the microstructure of the weld regions and hot compressed specimens. The samples were not carbon coated. Graphite tape was used to stick the samples on the sample holder and as such,

carbon analysis was not accurate. Although the areas with the graphite tape were avoided (which would have led to higher C results), the SEM-EDX is not the best technique for accurate analyses of the light elements. Moreover, the aim of the current study was to distinguish between different phases rather than their accurate analyses. Secondary and back-scattered electron detectors were used. The working distance of 8.5 mm and voltage of 15 kV were used.

Energy dispersive X-ray analysis (EDX) of the compositions of the precipitates was also done. Each type of feature was analysed at least five times to obtain an average. The EDX was done as per SEM user guide [113]. The samples were scanned to find the best areas, and the largest areas identified were analysed.

3.5.4 X-ray diffraction (XRD)

A Bruker D2 Phaser X-ray diffractometer was used. Copper ($\lambda = 1.79 \text{ \AA}$) was used as the target source of X-rays produced at 30 kV and 15 mA ratings. The diffracted rays were detected by a Lynx Eye PSD detector with a detector angle range of 5° . A scanning speed of $1.4^\circ 2\theta/\text{min}$ and a 0.02° step size were engaged for 10 minutes in scanning across $20-90^\circ$ of 2θ values. DIFFRAC plus-EVA® software was used to analyse the phases using the ‘peak-match’ tool.

3.5.5 Hardness

A Future Tech FM-700 Vickers microhardness tester was used with a 300 gf load and 10 sec dwell time. A total of five indentations were done on each hot compression specimen. On the weld sample five indentations were done per weld region/zone. All the indentations were done according to ASTM C1327 [115] which requires that each indentation is spaced apart by at least four times the diagonal of the previous indent to avoid strain hardening.

3.5.6 Grain size estimation

ImageJ software was used to measure grain sizes using the line intercept method on the SEM-BSE images. The measurements were done as per the recommendation of ASTM E112 [116].

$$\text{Average grain size} = \frac{\text{Line length}}{\text{Number of grains}} \dots\dots\dots [3.1]$$

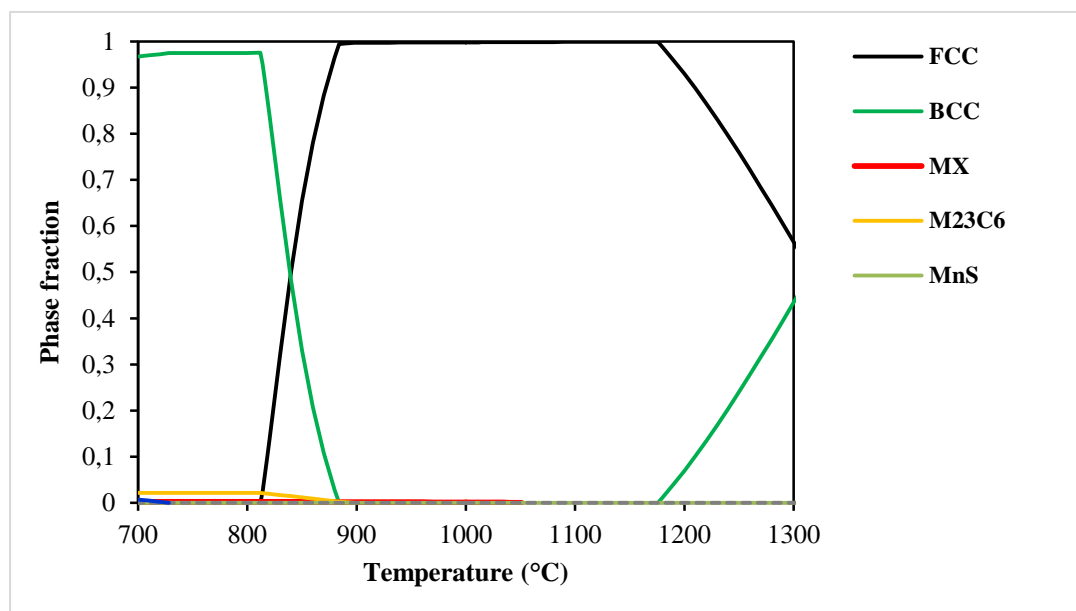
Chapter 4 :Results

This chapter presents all the results obtained from the characterization techniques and software's used in this study.

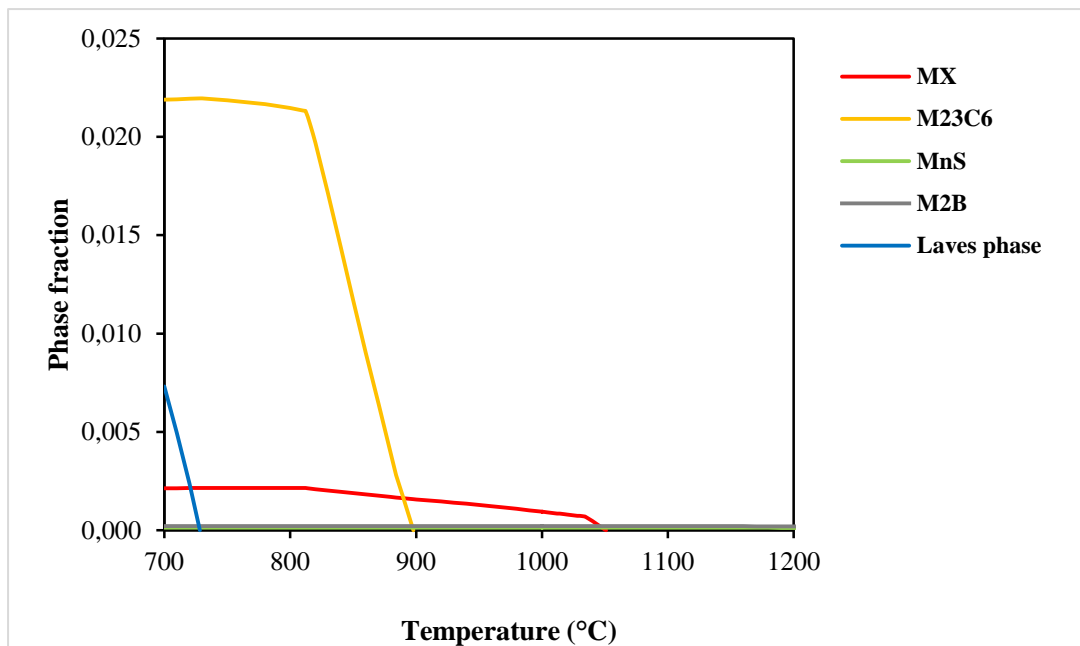
4.1 Thermodynamic calculations

Predicted phases in P92 steel

Figure 4.1 shows Thermo-Calc phase proportion diagrams for the pipe sample, rod and base metals. The phase proportion diagrams had similar trends and same phases due to a slight difference in their compositions. The delta ferrite formed and described as BCC phase at the temperatures above 1175 °C. The phase proportions of precipitates at 700 °C were: 0.002 MX, 0.02 M₂₃C₆, 0.0001 MnS, 0.0004 M₂B and 0.0087 Laves phase. Laves phase and M₂₃C₆ carbides were not visible above 900 °C. Tables 4.1 and 4.2 show the equilibrium transformation temperatures and minor phase percentages. Table 4.3 shows the phase fractions of the as-received steel at 700 °C.

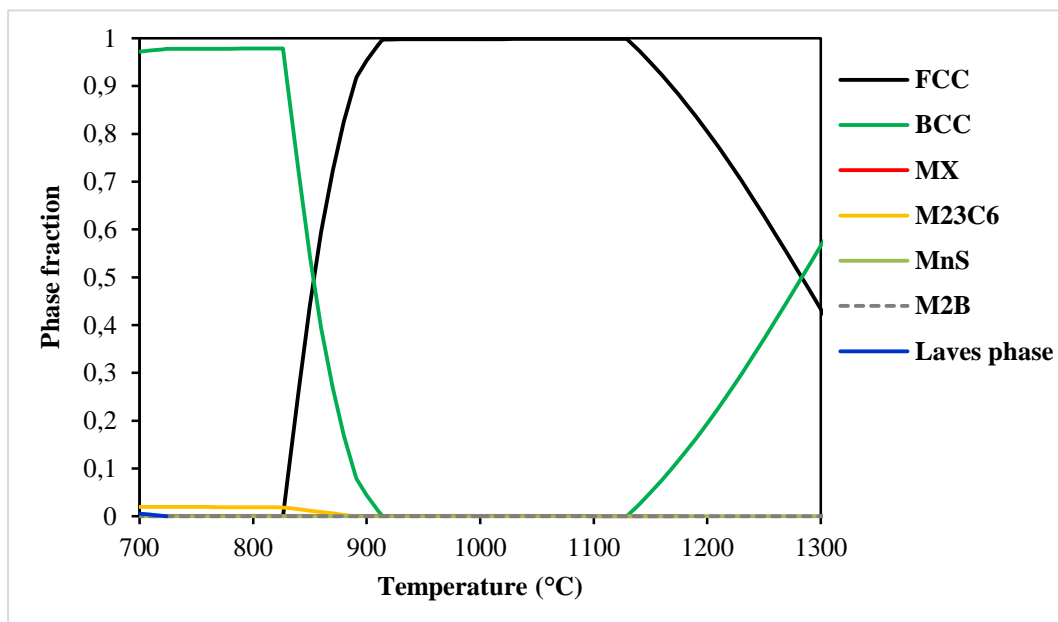


a)

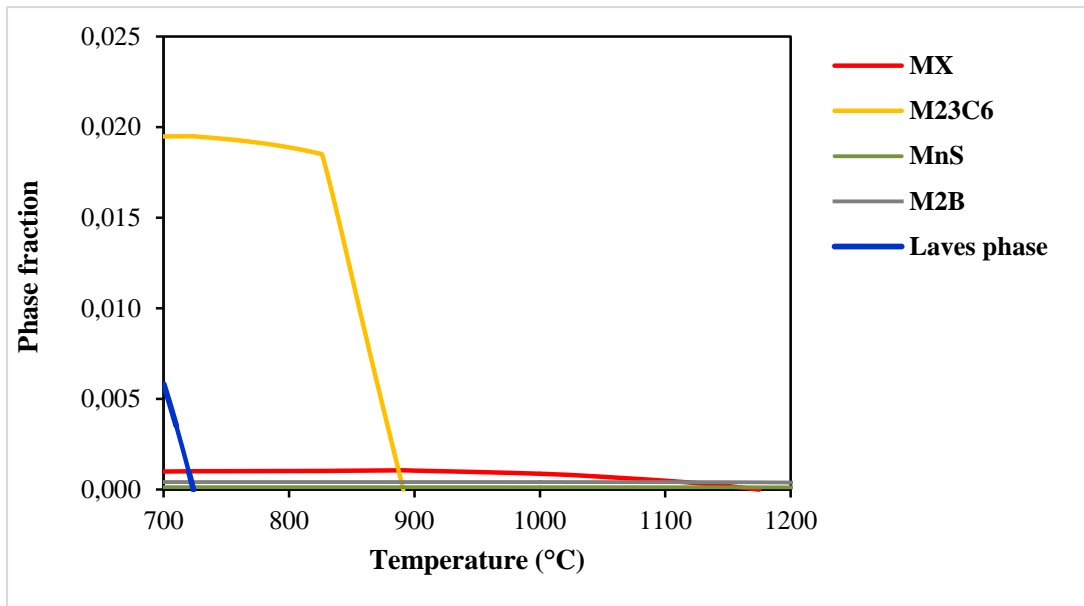


b)

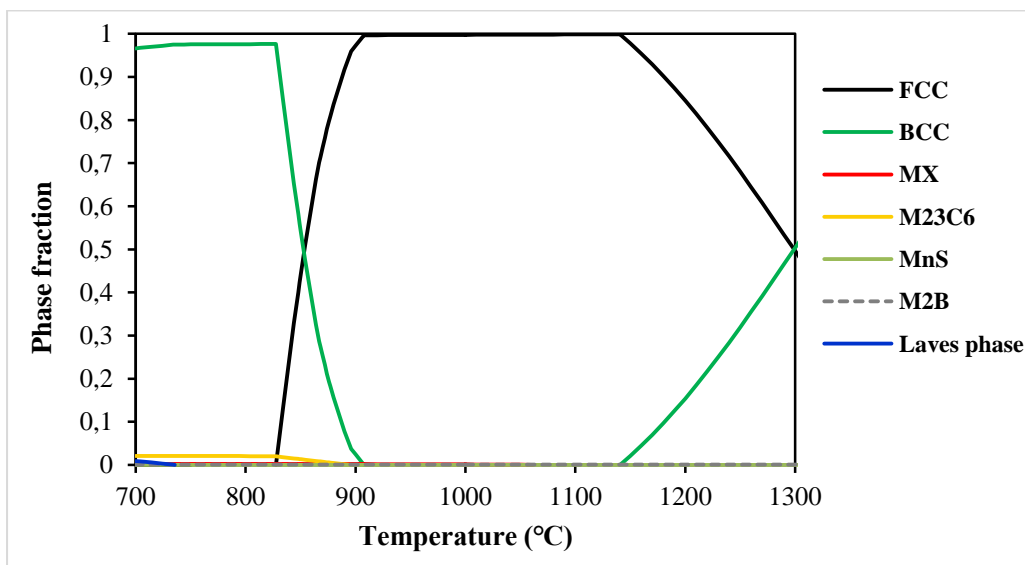
Figure 4.1: Thermo-Calc phase proportion diagrams for pipe steel: a) all phases, b) minor phases.



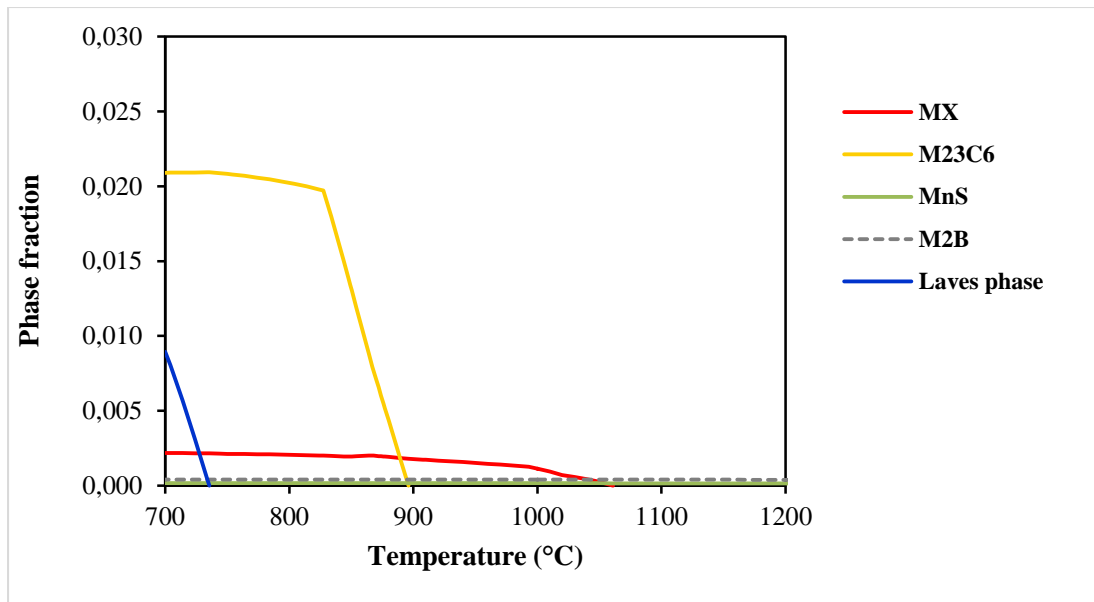
c)



d)
Figure 4.1: Thermo-Calc phase proportion diagrams for the rod metal, continued: c) All phases, d) minor phases.



e)



f)

Figure 4.1: Thermo-Calc phase proportion diagrams for the base metal, continued: e) all phases, f) minor phases.

Table 4.1: Equilibrium transformation temperatures from Thermo-Calc.

	Temperature (°C)		
	Pipe steel	Base metal	Rod metal
Alpha ferrite formation	884	907	913
Lower limit for delta ferrite	1175	1140	1129
Laves formation	728	735	723
M ₂₃ C ₆ formation	897	896	891
MX formation	1050	1060	1175

Table 4.2: Phase fractions of minor phases at deformation from Thermo-Calc.

Deformation Temperature (°C)	Material	MnS	M ₂ B	MX	Delta ferrite
1100	Pipe	0.013	0.022	-	-
	Base metal	0.016	0.040	-	-
	Rod	0.013	0.042	0.044	-
1200	Pipe	0.013	0.020	-	6.99
	Base metal	0.015	0.039	-	15.39
	Rod	0.012	0.039	-	19.4

Table 4.3: Phase fractions of the as-received sample at 700 °C from Thermo-Calc.

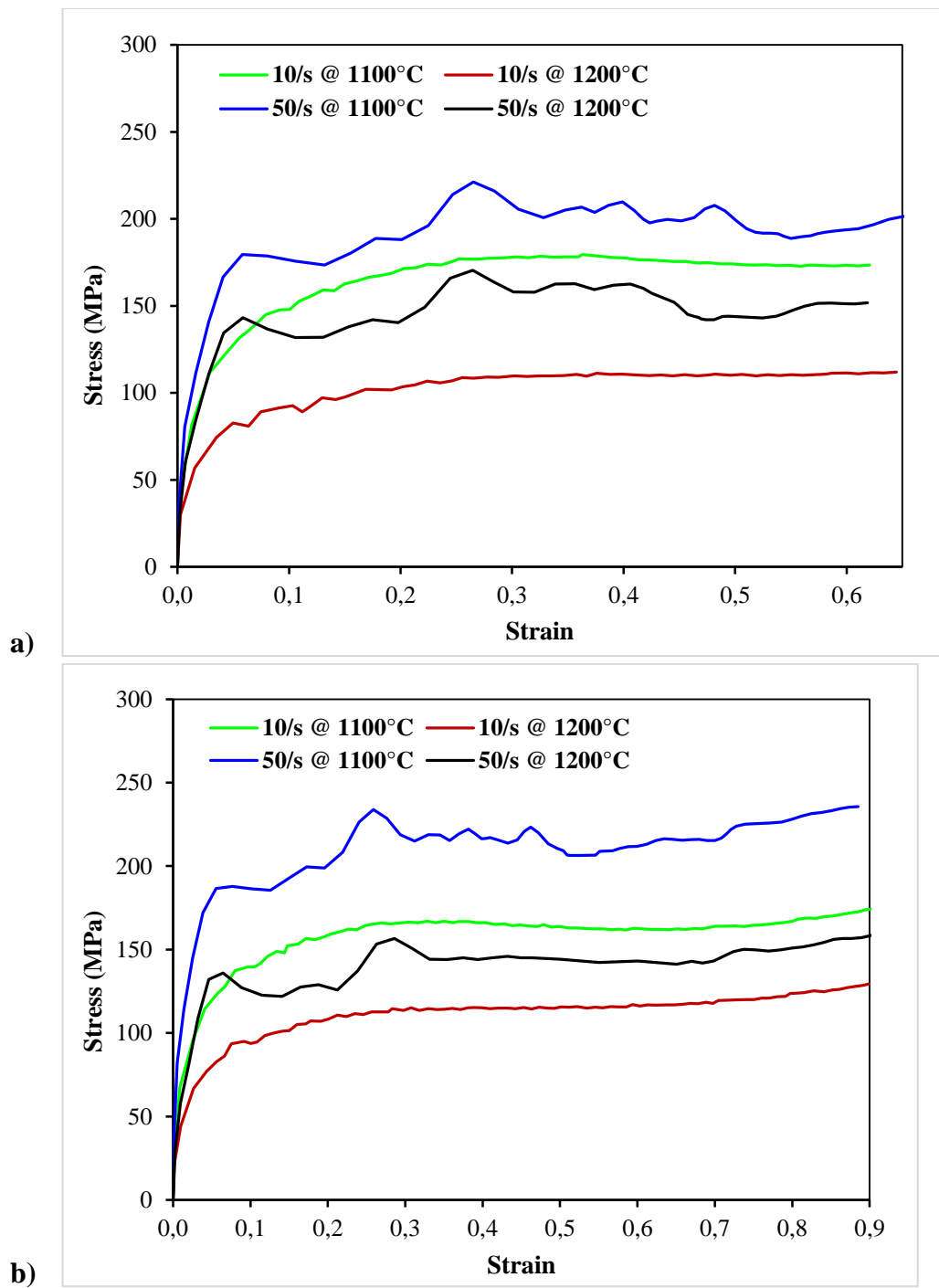
Phases	Fraction
M₂₃C₆	0.021882
MnS	0.000136
M₂B	0.00022
MX	0.002141
Laves	0.007312
Ferrite	0.9674

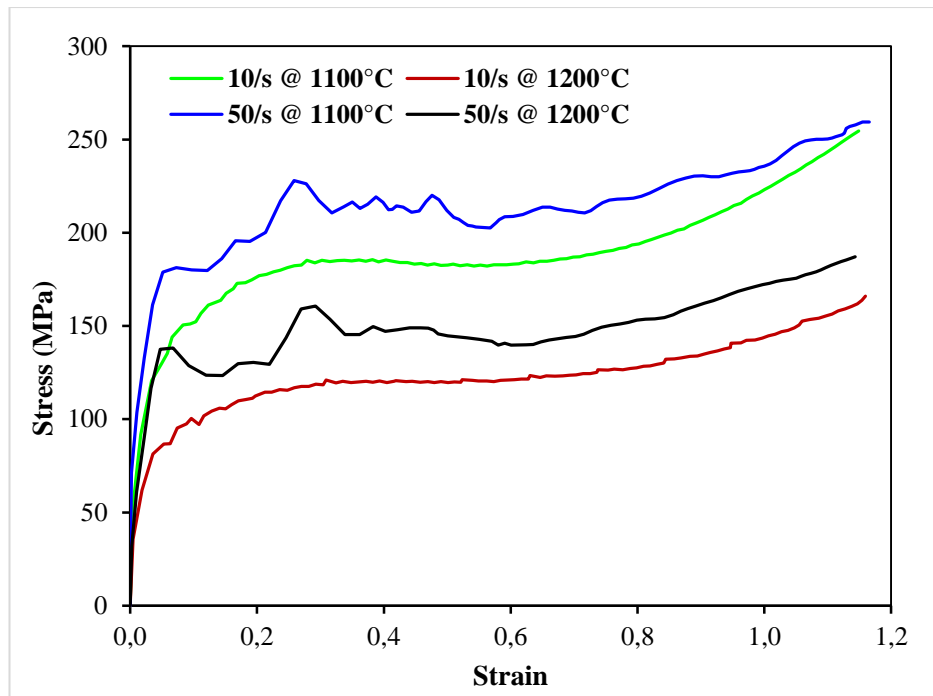
4.2 Hot compression of P92 steel

Stress-strain curves

Figures 4.2 and 4.3 show the stress-strain curves of the P92 pipe steel specimens deformed at 1100 and 1200 °C, having strain rates of 10 and 50 s⁻¹, for total strains of 50 % (0.6), 70 % (0.9) and 90 % (1.2). Overall, the graphs show that with the increase in strain from 0.6 to 0.9 and 1.2, the flow stress continued to increase due to the bulging of the sample. The flow stress increased with decreased temperature at a given strain rate. Similarly, at a given temperature, the flow stress increased with increasing strain rate. The curves at 50 s⁻¹ strain rate showed oscillation due to the Gleeble erratic movements at high strain rates.

The flow stress increased with decreasing deformation temperature, and the average maximum flow stress were higher at 1100 °C. Figures 4.4 and 4.5 show that the average maximum and proof stresses (taken at 0.2 %) decreased with increasing temperature and decreasing strain rates.





c)
Figure 4.2: True stress-strain curves from the uniaxial Gleeble hot compression tests on the P92 pipe steel for different total strains: a) 50 %, b) 70 %, c) 90 %.

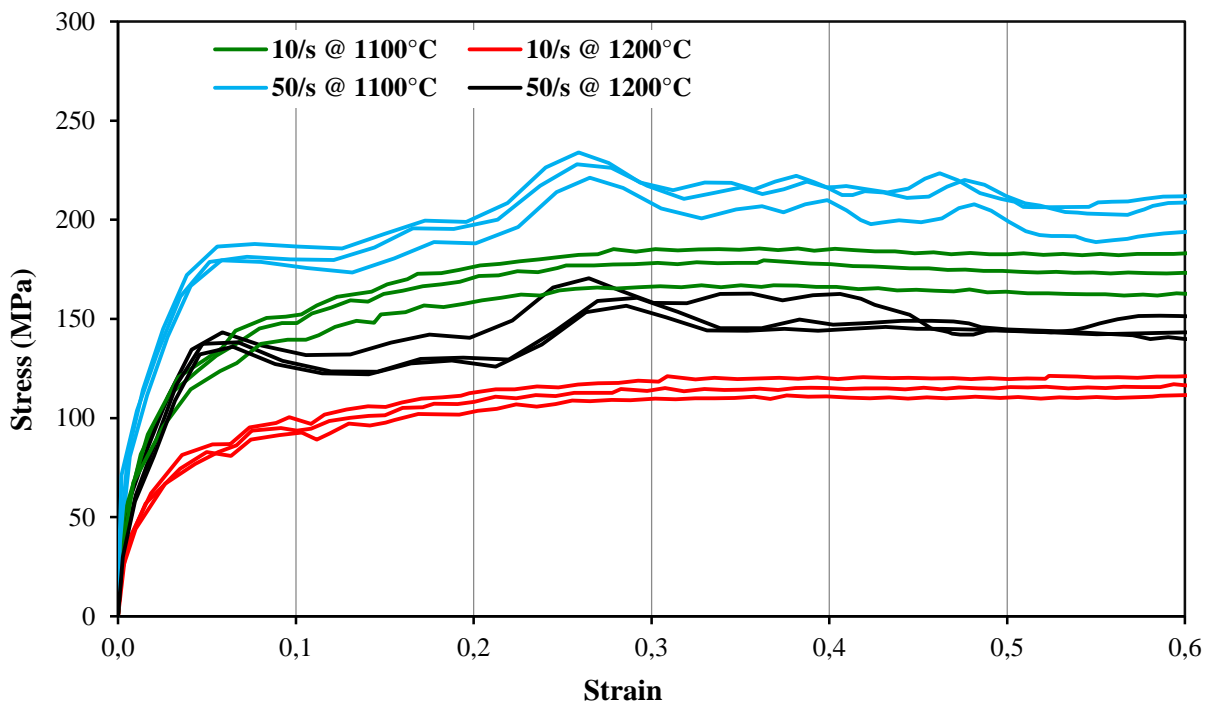


Figure 4.3: All true stress-true strain curves from the uniaxial Gleeble hot compression tests on the P92 pipe steel up to a total strain of 0.6.

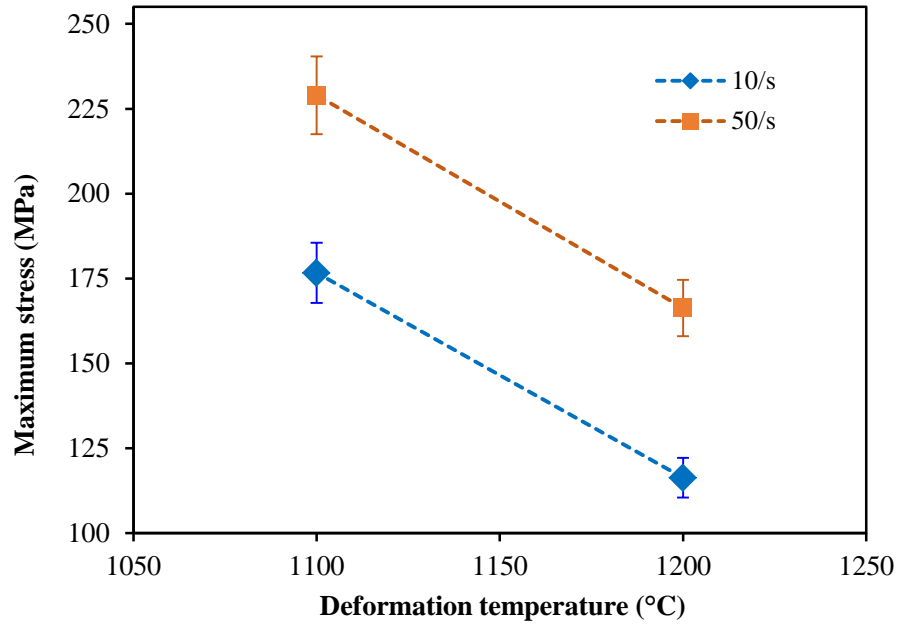


Figure 4.4: Average maximum stresses attained at different strain rates and deformation temperatures for compressed P92 pipe steel samples.

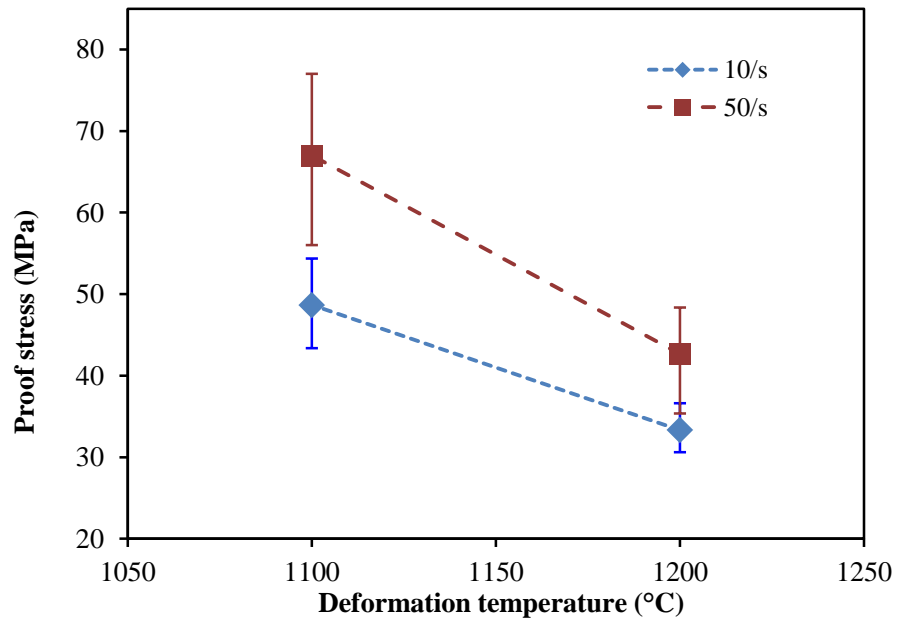


Figure 4.5: Average proof stresses at different strain rates and deformation temperatures for compressed P92 pipe steel samples.

4.3 Characterization

4.3.1 Chemical analysis

Table 4.4 shows the composition results from optical emission spectrographic analysis (OES) and inductively coupled plasma atomic emission spectroscopy (ICP). Figures 4.6 and 4.7 together with Table 4.5 show EDX analyses of similar areas of the as-received P92 pipe steel and FHPP weld. Boron was only found in OES results (Table 4.4) and absent in EDX results (Table 4.5), which was expected since it is a light element. The overall compositions of the materials were similar which confirmed that the FHPP weld was also made from P92 steel. However, nitrogen and cobalt contents were higher in EDX.

Table 4.4: OES results of the P92 pipe sample and the P92 FHPP weld (base and rod metals).

Composition in wt (%)				
Element	P92 pipe		FHPP sample	
	steel sample	Base metal	Rod 'filler' metal	
C	0.12	0.11	0.11	
Mn	0.43	0.26	0.36	
S	≤0.005	0.006	≤0.005	
P	0.011	0.016	0.016	
Si	0.16	0.13	0.15	
Cr	9.61	9.85	9.47	
Mo	0.49	0.50	0.52	
Ni	0.20	0.19	0.18	
Cu	0.11	0.11	0.10	
Al	≤0.005	≤0.005	≤0.005	
V	0.19	0.18	0.20	
Nb	0.096	0.092	0.093	
Ti	≤0.005	≤0.005	≤0.005	
W	1.97	1.98	1.78	
Co	0.027	0.027	0.016	
B	0.0020	0.0369	0.0038	
N*	0.0430	0.0513	-	
Cd	0.055	≤0.0005	≤0.0005	
Fe	balance	balance	balance	

* ICP analysis

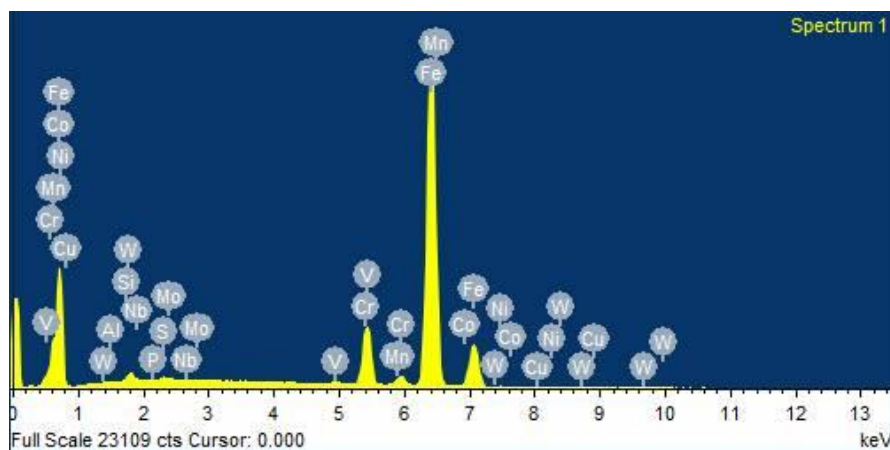
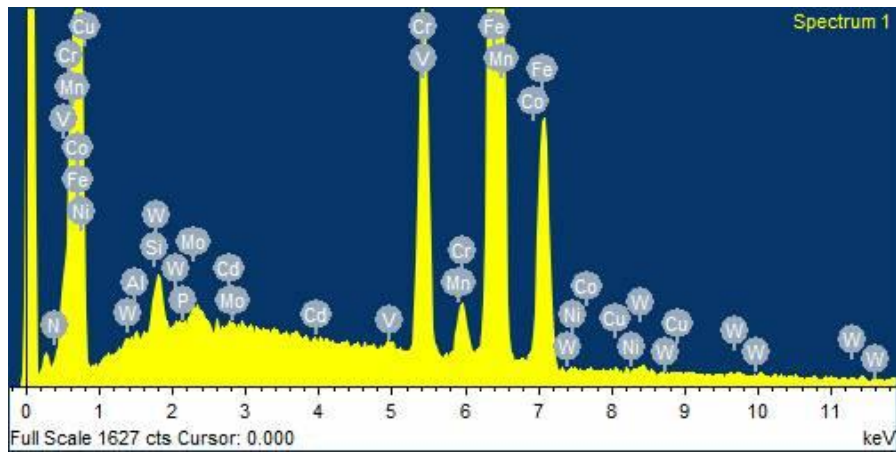


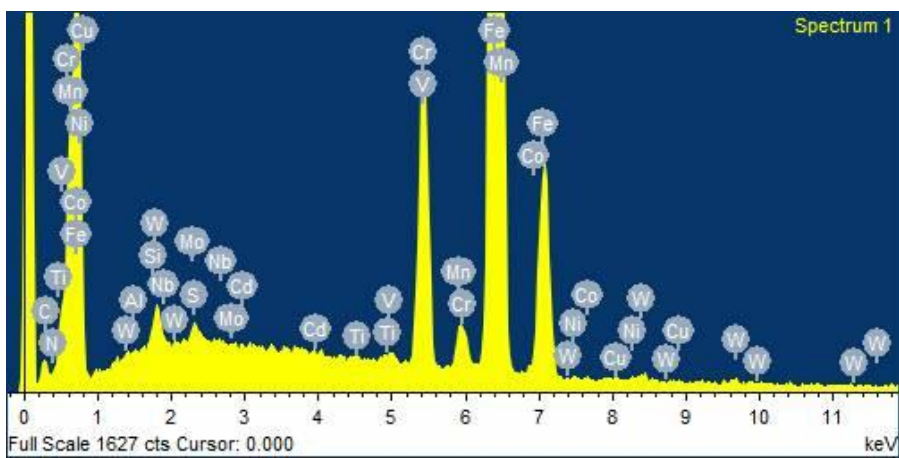
Figure 4.6: EDX spectrum of the as-received P92 pipe steel showing elements present.

Table 4.5: EDX analyses of the P92 pipe sample and the P92 FHPP weld (base and rod metals) showing the average compositions with standard deviations.

Element	Average weight%		
	P92 pipe steel sample	FHPP sample	
		Base metal	Rod 'filler' metal
Mn	0.5±0.1	0.5±0.0	0.5±0.1
S	≤0.04	≤0.04	0.1±0.0
P	0.1±0.0	0.1±0.0	≤0.04
Si	0.1±0.0	0.1±0.0	0.1±0.0
Cr	9.2±0.1	9.3±0.1	9.3±0.1
Mo	0.5±0.2	0.5±0.1	0.5±0.2
Ni	0.2±0.1	0.2±0.1	0.3±0.2
Cu	0.1±0.0	0.1±0.0	0.1±0.0
Al	≤0.04	0.1±0.0	≤0.04
V	0.2±0.0	0.2±0.1	0.2±0.0
Nb	0.2±0.1	0.2±0.0	0.1±0.1
Ti	0.1±0.0	≤0.04	≤0.04
W	2.0±0.1	2.1±0.1	1.9±0.1
Co	0.3±0.0	0.4±0.1	0.3±0.1
N	1.3±0.5	1.0±0.4	1.0±0.6
Cd	0.1±0.1	0.1±0.0	0.1±0.0
Fe	balance	balance	balance



a)



b)

Figure 4.7: EDX spectra of P92 FHPP weld sections: a) base metal and b) rod (filler) showing elements present.

EDX area analyses of the FHPP weld, rod metal and base metal are compared in Table 4.5. The chromium and tungsten contents for the rod and base metals were similar, and the overall EDX analysis agreed with the OES analysis (Table 4.4). This confirmed that the rod metal was made from P92 steel.

4.3.2 Microstructural analysis

Figures 4.8- 4.10 show the optical images of the as-received, deformed and heat treated P92 samples. The as-received and heat treated samples showed tempered martensite indicated by coarse laths. The as-deformed samples showed untempered martensite with fine, needle-like structures. Prior austenite grain boundaries (PAGBs) were also visible as shown in Figures 4.8 and 4.10. The samples deformed at 1100 °C had finer grains than those deformed at 1200 °C.

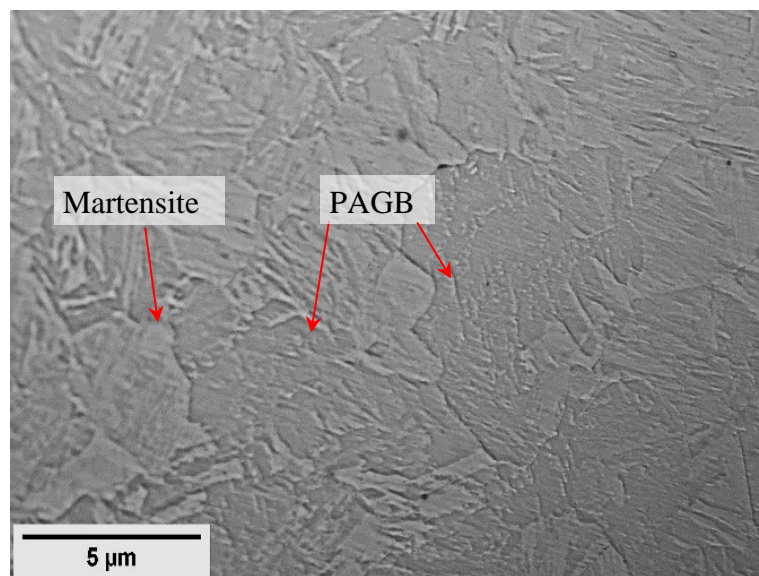


Figure 4.8: Optical image of the as-received P92 steel showing martensite and PAGBs (scale bar = 5 μm).

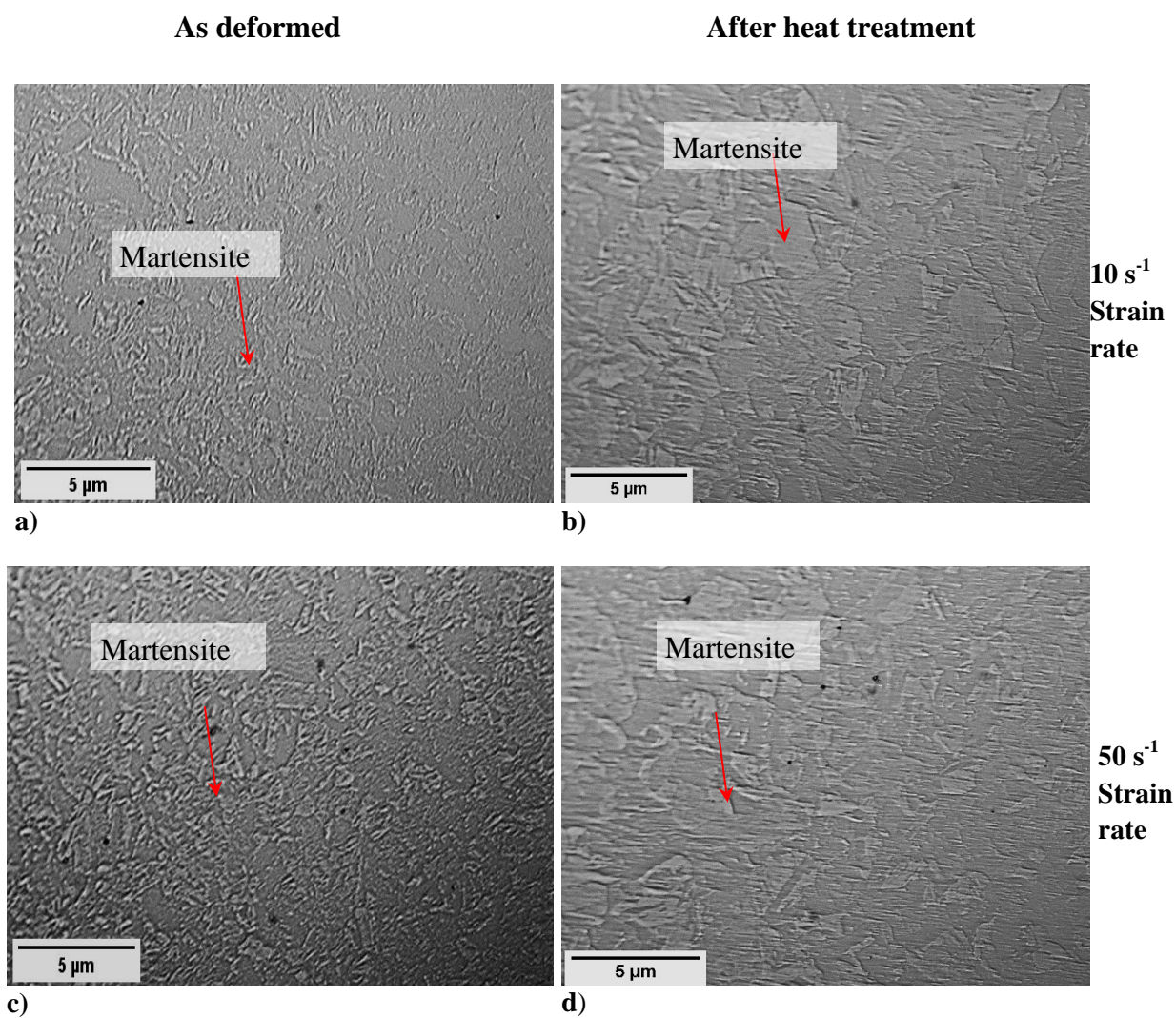


Figure 4.9: Optical images for the P92 steel sampled deformed at 1100 °C and 50% total strain: a) as-deformed, b) deformed and heat treated for 5 hours, c) as deformed, d) deformed and heat treated for 3 hours 45 minutes, showing martensite (scale bar = 5 μm).

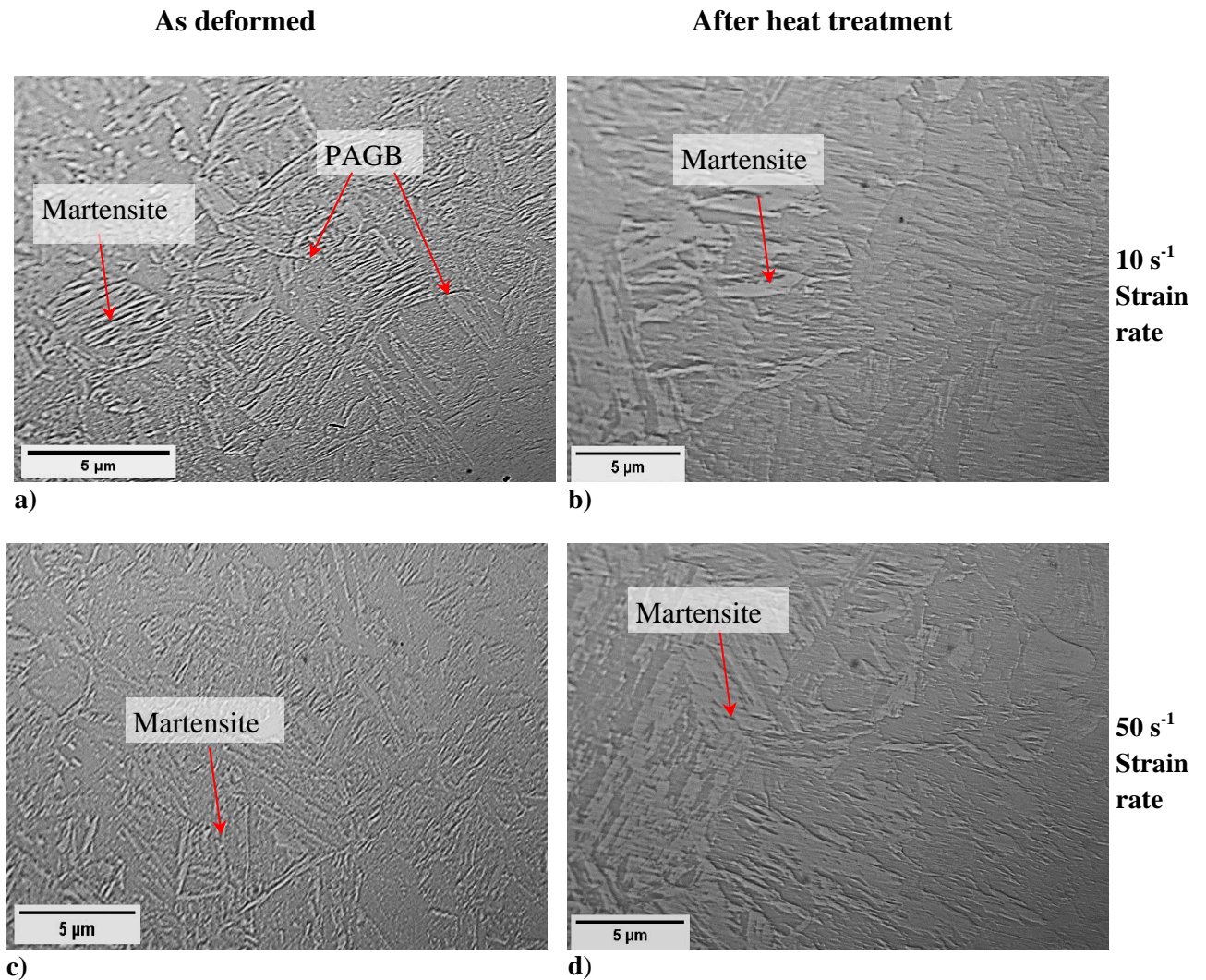


Figure 4.10: Optical images for the P92 steel sampled deformed at 1200 °C and 50% total strain: a) as-deformed, b) deformed and heat treated for 5 hours, c) as deformed, d) deformed and heat treated for 3 hours 45 minutes, showing martensite and PAGBs (scale bar = 5 μm).

SEM backscattered electron (SEM-BSE) images of electro-etched samples in the following solutions: nitric acid, potassium hydroxide, ammonium persulfate and oxalic acid, are shown in Figure 4.11. All the electro-etchants only revealed the prior austenite grain boundaries (PAGBs) by attacking the precipitates on the grain boundaries. The darker areas inside prior austenite grains were coring from the as-cast dendritic structure.

All the samples etched by immersion revealed tempered martensite, lath boundaries and PAGBs (Figure 4.12) except for Murakami's etch (Figure 4.12 d), which only revealed PAGBs. The tempered martensite structure was recognised by the lath structure with precipitates on the laths' boundaries. Hydrochloric acid was a common constituent in all the reagents that revealed tempered martensite: Marble's reagent, ferric chloride reagent, Kalling's reagent and Villella's reagent.

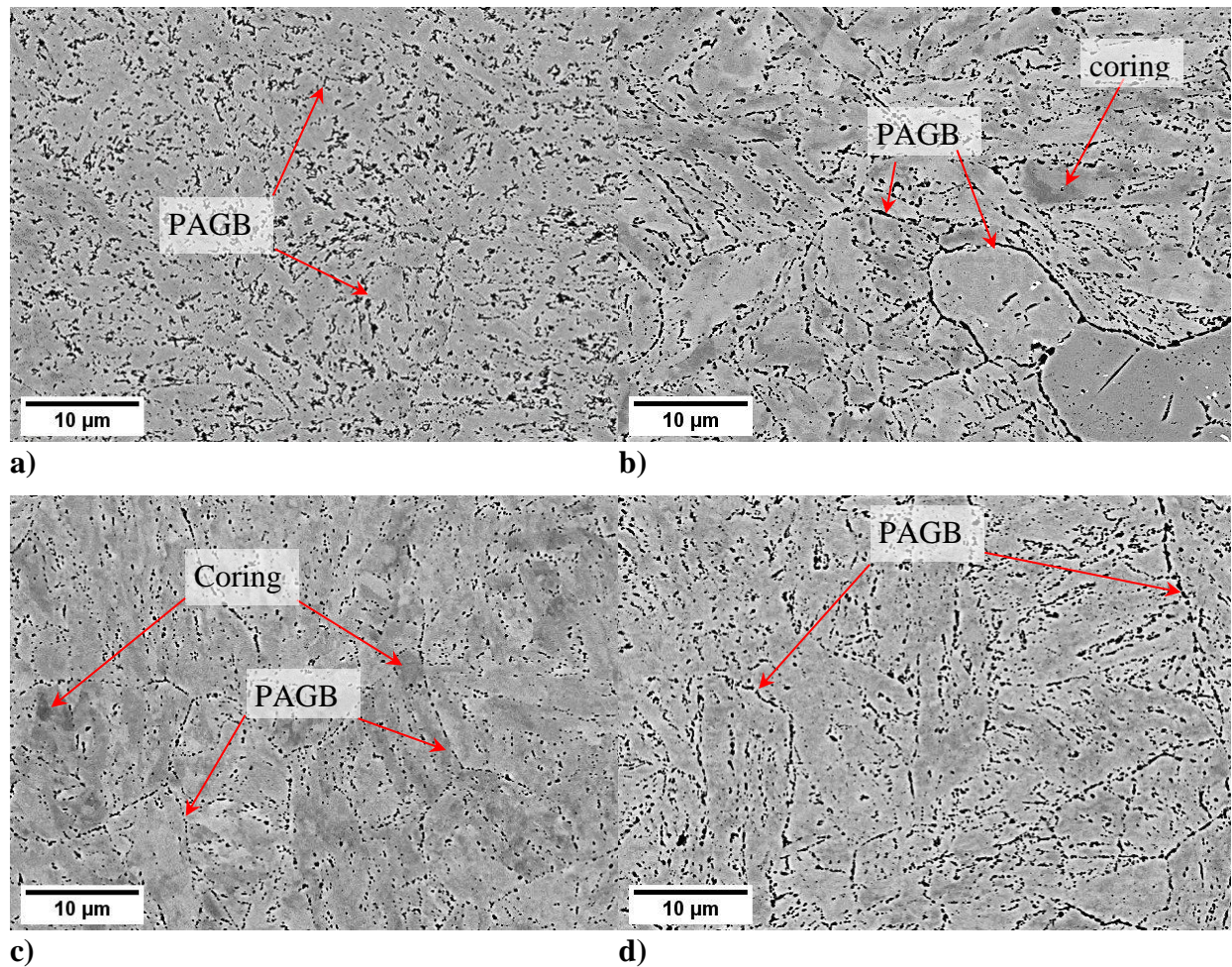


Figure 4.11: SEM-BSE images for as-received P92 steel after etching: a) nitric acid, b) potassium hydroxide, c) ammonium persulfate, d) oxalic acid, showing coring and PAGBs (scale bar = 10 µm).

The microstructure of the as-received P92 pipe steel is shown in Figure 4.13. The samples exhibited a typical tempered martensite structures with martensite laths within the prior austenite grains. There were submicron-sized precipitates on the grain boundaries. The

average grain size of the prior austenite grains was $7.6 \pm 2.0 \mu\text{m}$. Small regions of ferrite were revealed as indicated in Figure 4.13.

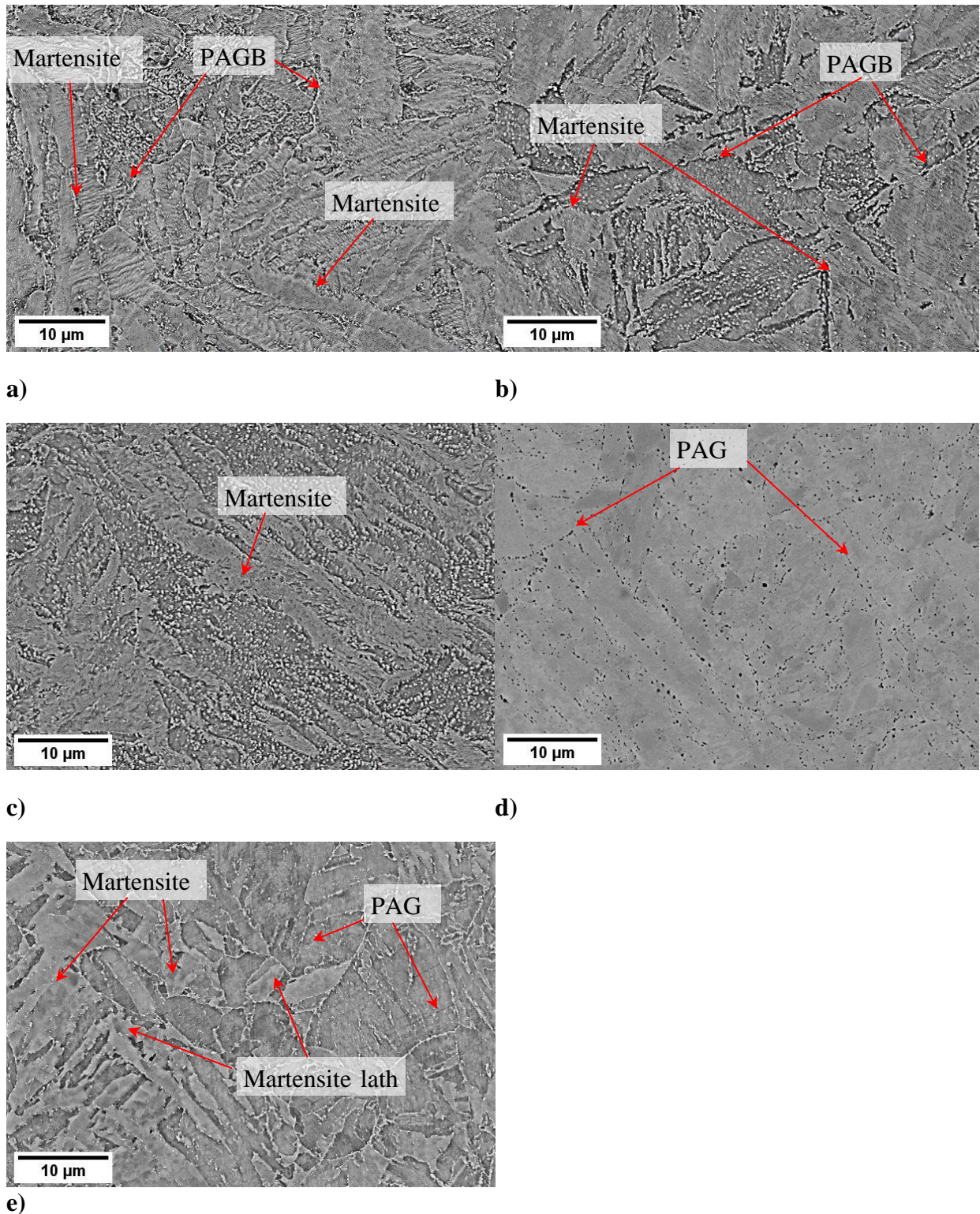


Figure 4.12: SEM-BSE images for as-received P92 steel after etching: a) Marble's reagent, b) Ferric chloride, c) Kalling's reagent, d) Murakami's reagent, e) Villella's reagent, showing tempered martensite, martensite laths and PAGBs (scale bar = 10 μm).

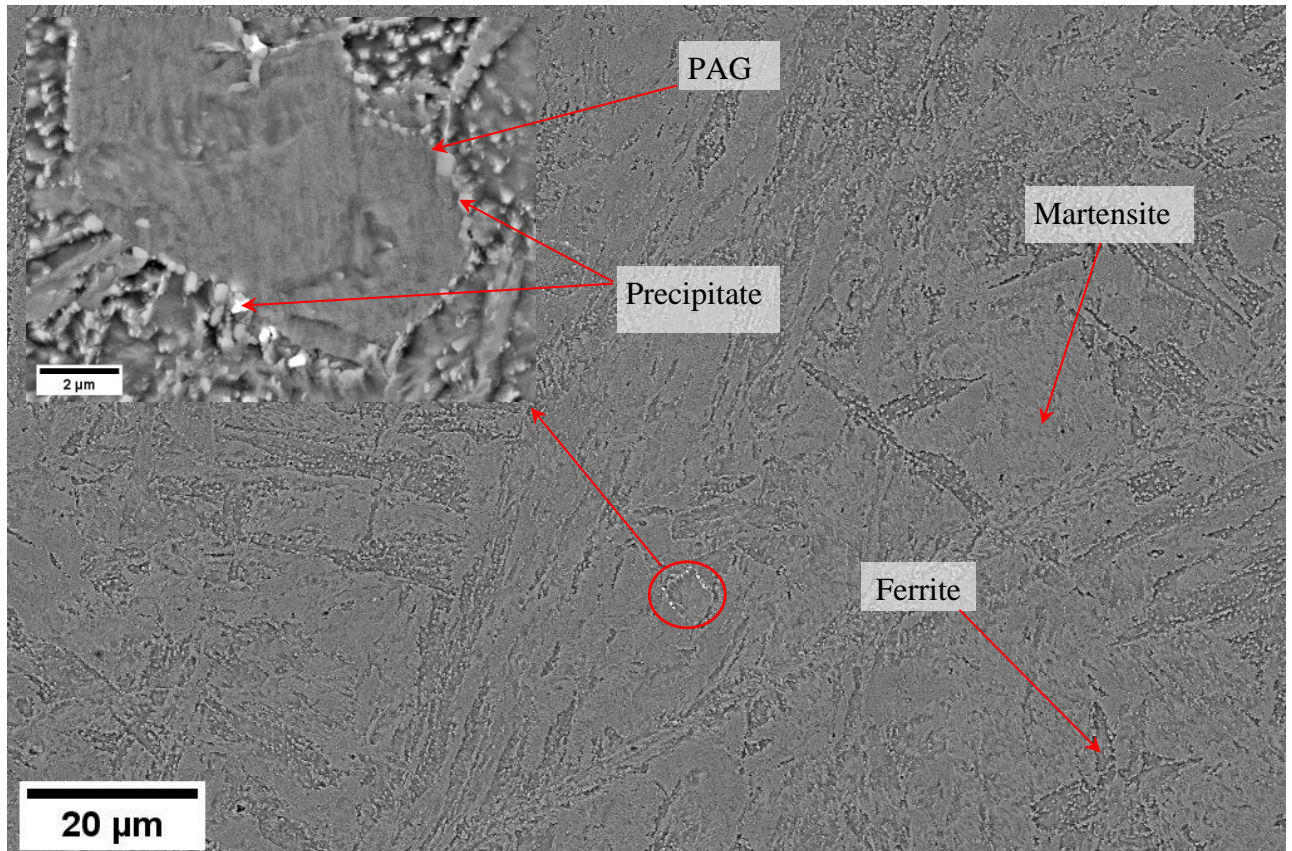
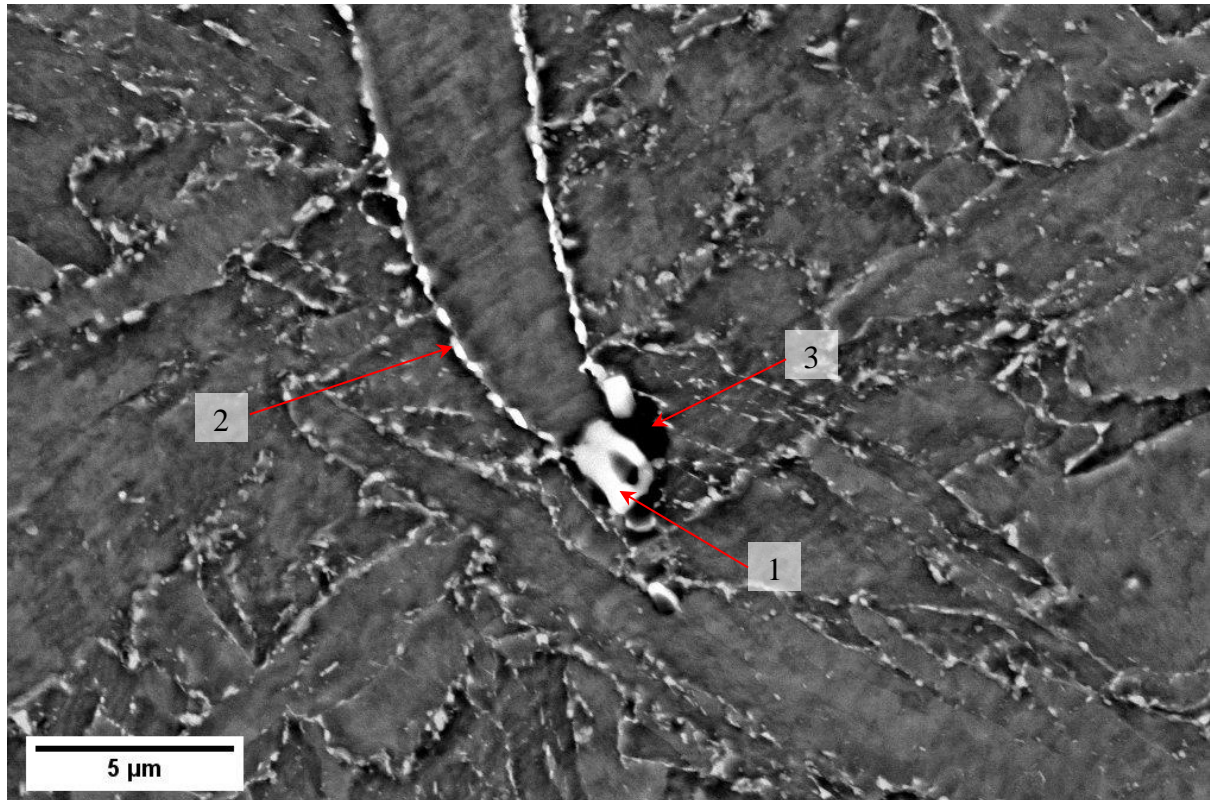


Figure 4.13: SEM-BSE image of the etched as-received P92 steel (scale bar = 20 μm), with inset of high magnification image of the circled area (scale bar = 2 μm) showing precipitates on PAGBs.

The precipitates (Figures 4.14 and 4.15) and inclusions (Figure 4.16) were analysed, and their analyses are summarised in Table 4.6. The precipitates were identified as M_2X , M_{23}C_6 (even taking into account the limitations of using EDX for measuring carbon), MX , MnS , and the inclusions were oxide and nitride. Table 4.6 shows that the precipitate in Figure 4.14 (precipitate #3) and inclusions in Figures 4.15 and 4.16 contained no tungsten, while precipitates # 1 and 2 (Figure 4.14) contained less than 10 wt% of the heavier elements such as Nb and W. This explains the darker contrasts of precipitates # 1 and 2 because backscattered electrons are sensitive to the atomic mass of the nuclei from which they scatter. Heavier elements emit higher energy backscattered electrons, hence they appear brighter [117].



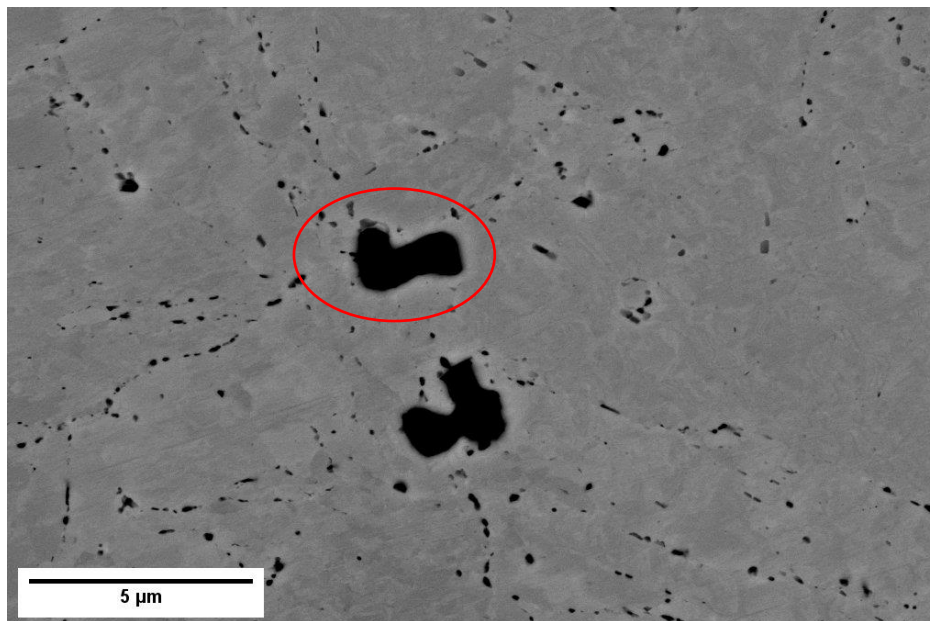
Precipitate #1	
Element	Weight%
N	4.6
V	2.4
Cr	5.3
Mn	0.8
Fe	39.7
Nb	46.2
W	1.0
Total	100.0

Precipitate #2	
Element	Weight%
V	1.2
Cr	12.2
Fe	65.7
Mo	4.4
W	16.5
Total	100.0

Precipitate #3	
Element	Weight%
S	15.5
V	1.2
Cr	5.6
Mn	25.6
Fe	32.2
Cu	0.5
Nb	14.8
100.0	

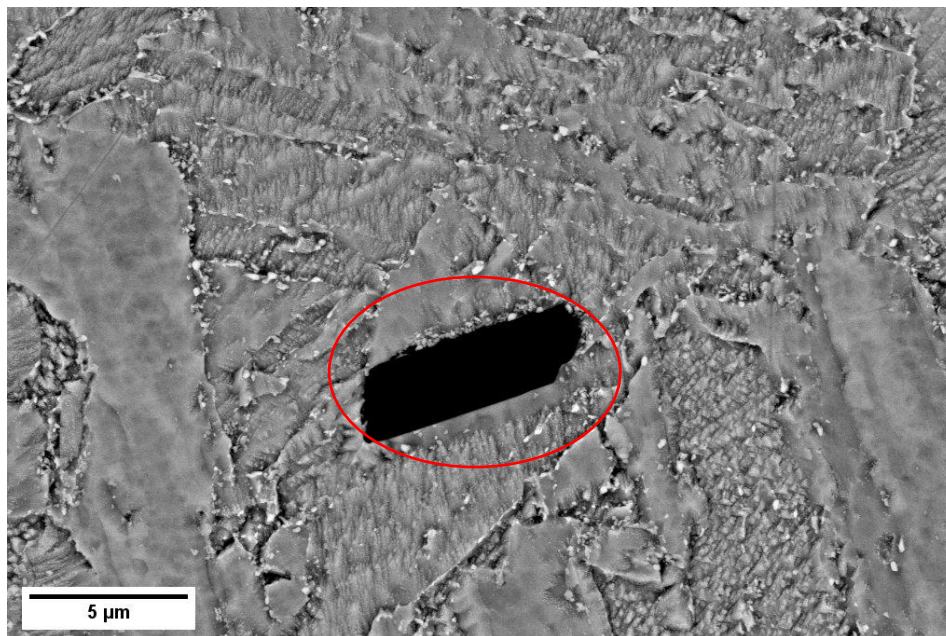
Figure 4.14: SEM-BSE image and EDX analysis of selected grain boundary precipitates in as-received P92 steel showing different precipitates.

The chromium content of the precipitates was higher than 1 wt%, which made it possible to form the precipitates listed in Table 4.6 [34]. The higher Nb and N contents in precipitate #1 made it M_2X . The precipitate #2 with Cr content higher than 7 wt% and presence of Mo was identified as $Cr_{23}C_6$ rather than Cr_7C_3 [34]. Moreover, W in precipitate #2, promoted the formation of $Cr_{23}C_6$. The precipitate #3 was identified as $(Mn,Cu)S$ due to high Mn and S contents with the presence of Cu. [34].



Element	Weight %
N	43.4
Cr	6.6
Fe	50.0
Totals	100.0

Figure 4.15: SEM-BSE image and EDX analysis of a nitrogen-containing precipitate in as-received P92 steel.



Elements	weight %
O	49.7
Mg	1.4
Al	45.3
Cr	0.9
Mn	0.4
Fe	2.2
Total	100.0

Figure 4.16: SEM-BSE image and EDX analysis of an oxide inclusion in as-received P92 steel.

Table 4.6: Summary of EDX analysed precipitates and inclusions in as-received P92.

Figure: analysis #	Particle composition (atomic%)	Identification
9: precipitate 1	V + Nb = 31.9%, N = 19.1%, Fe = 41.9%, Cr + Mn + W = 7.1%	M ₂ X: (V,Nb) ₂ N
9: precipitate 2	Cr + Fe + Mo + W = 79%, C	M ₂₃ C ₆ : (Cr,Fe,Mo,W) ₂₃ C ₆
9: precipitate 3	Mn = 19.7%, Cu = 0.3%, S = 20.5% C, Cr + V + Nb + Fe + Cu = 48.6%	(Mn,Cu)S
10	N = 75.2%, Fe = 21.7%, Cr = 3.1%	Possible M ₂ X (Cr ₂ N)
11	O = 60.3%, Al = 32.6%, Mg = 1.1%, Cr + Mn + Fe + C = 6%	Oxide inclusions: Al ₂ O ₃ and MgO

Figures 4.17 and 4.18 show the SEM images of the specimens compressed at 1100 °C and 1200 °C, respectively. At 1100 °C, there was less martensite, especially at low deformation strains (Figure 4.17a-c). The microstructures of specimens deformed at 1200 °C (Figure 4.18) showed full martensite. The microstructures at both 1100 °C and 1200 °C did not show any precipitates which suggests complete dissolution of the precipitates, including M₂₃C₆ and MX, unless they were too small to be seen.

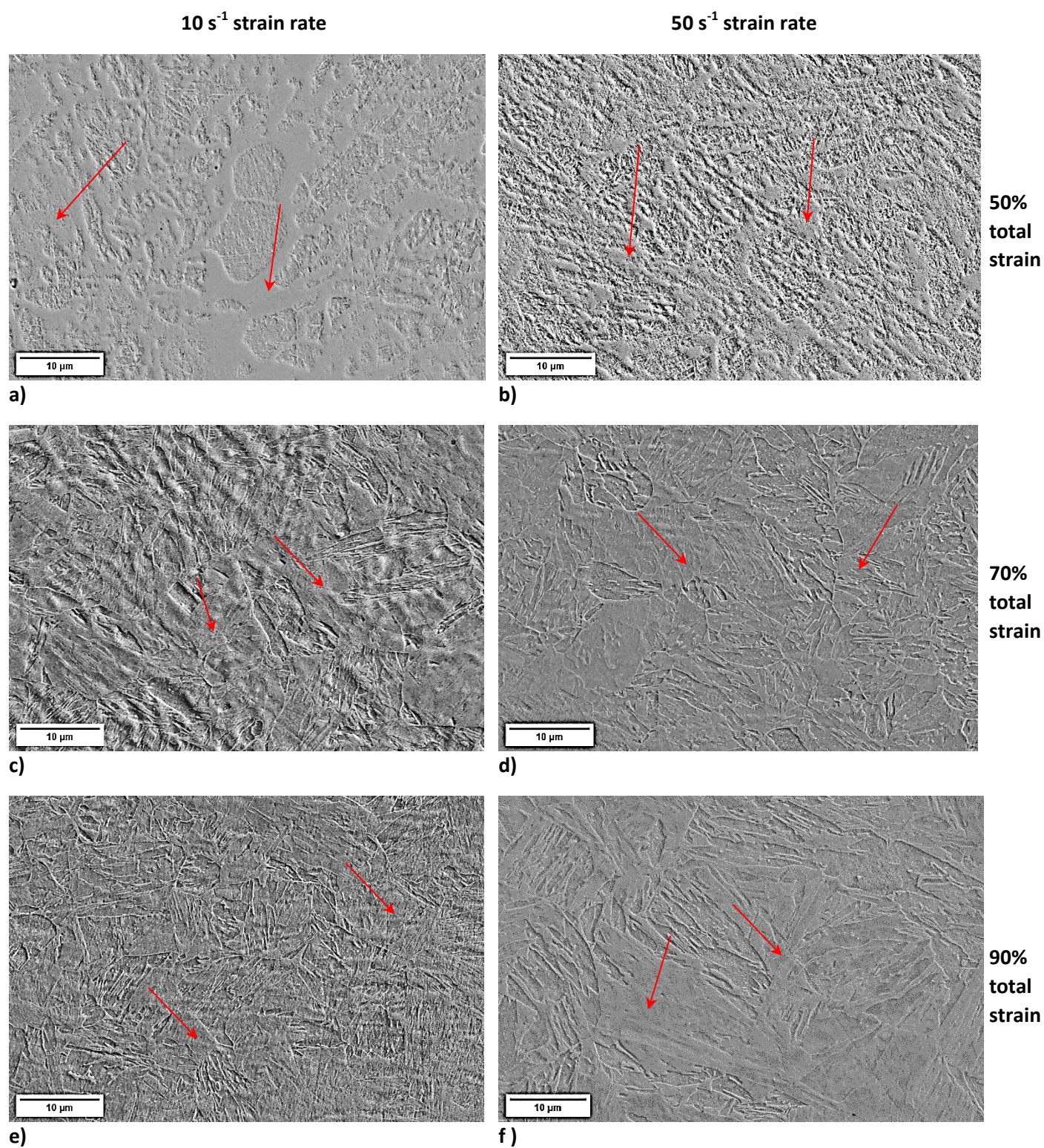


Figure 4.17: SEM-SE micrographs of the P92 samples deformed at 1100 °C with arrows showing martensite lath (scale bar = 10 μm).

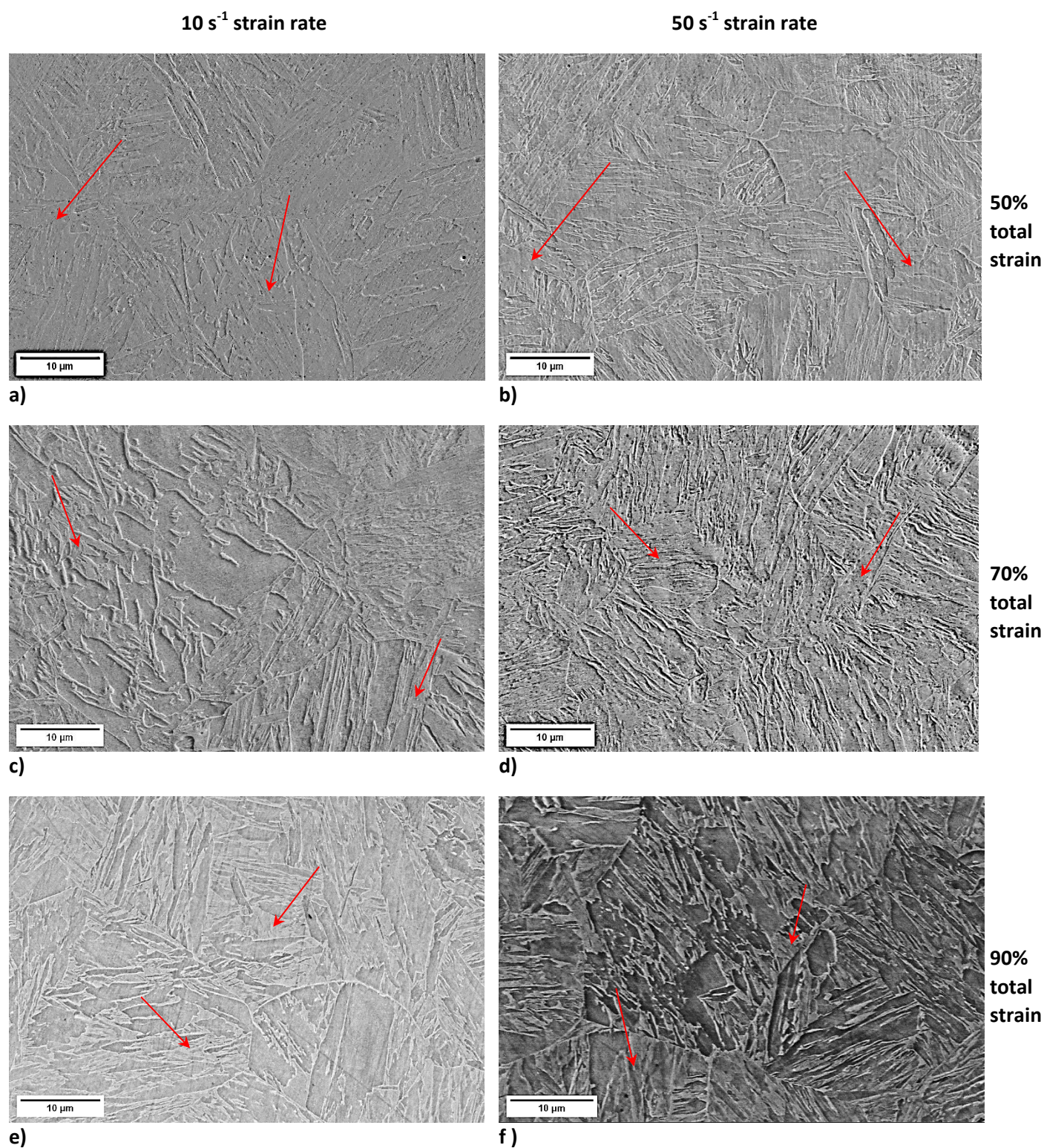


Figure 4.18: SEM-SE micrographs of the P92 samples deformed at 1200 °C with arrows showing martensite lath (scale bar = 10 μm).

Figures 4.19 – 4.22 show the SEM-BSE images for the deformed specimens after the heat treatments. The microstructure of the as-deformed specimens (Figures 4.17 and 4.18) transformed from untempered to tempered martensite after heat treatment. The tempered martensite had fine precipitates on the prior austenite grain boundaries and lath boundaries as shown by high magnification micrographs in Figures 4.23 and 4.24. Table 4.7 shows prior austenite grain measurements of the deformed P92 steel samples after heat treatment. The specimens deformed at 1100 °C had finer grains of $8\pm2\text{ }\mu\text{m}$ compared to $17\pm3\text{ }\mu\text{m}$ at 1200 °C after both 3 hours 45 minutes and 5 hours heat treatments. At a given deformation temperature, the difference in grain sizes between the strain rates, 10 and 50 s^{-1} were $\leq 1\text{ }\mu\text{m}$. Similarly, at a given deformation strain rate and temperature, the difference in grain sizes for both heat treatments, 3 hours 45 minutes and 5 hours were $\leq 2\text{ }\mu\text{m}$. At 1100 °C, the difference in grain sizes for different deformation strains, 50, 70 and 90% were $\leq 4\text{ }\mu\text{m}$, while at 1200 °C the differences were $\leq 9\text{ }\mu\text{m}$.

.

.

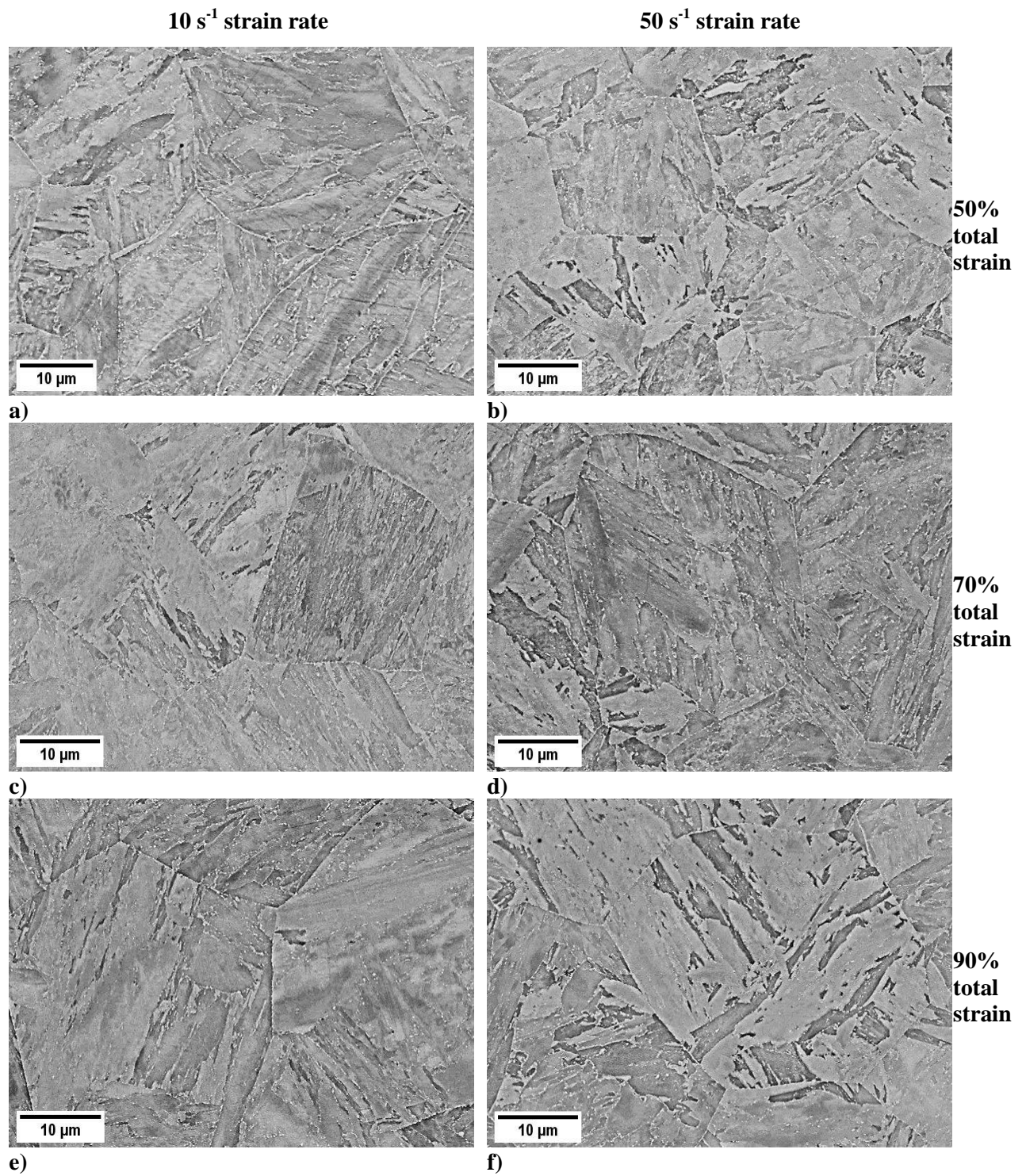


Figure 4.19: SEM-BSE micrographs of P92 samples deformed at 1200 °C and heat treated for 5 hours (scale bar = 10 μm).

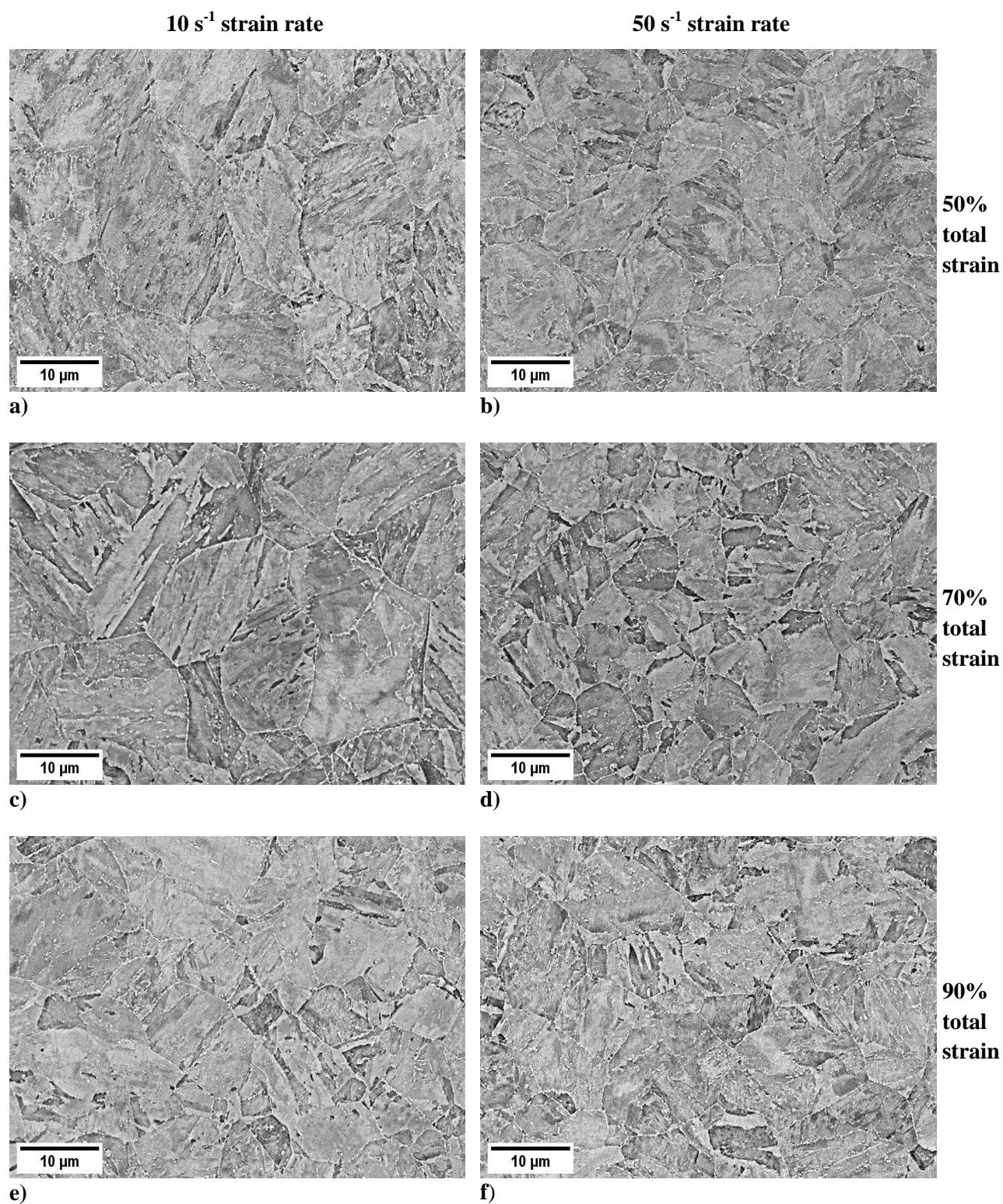


Figure 4.20: SEM-BSE micrographs of P92 samples deformed at 1100 °C and heat treated for 5 hours (scale bar = 10 μm).

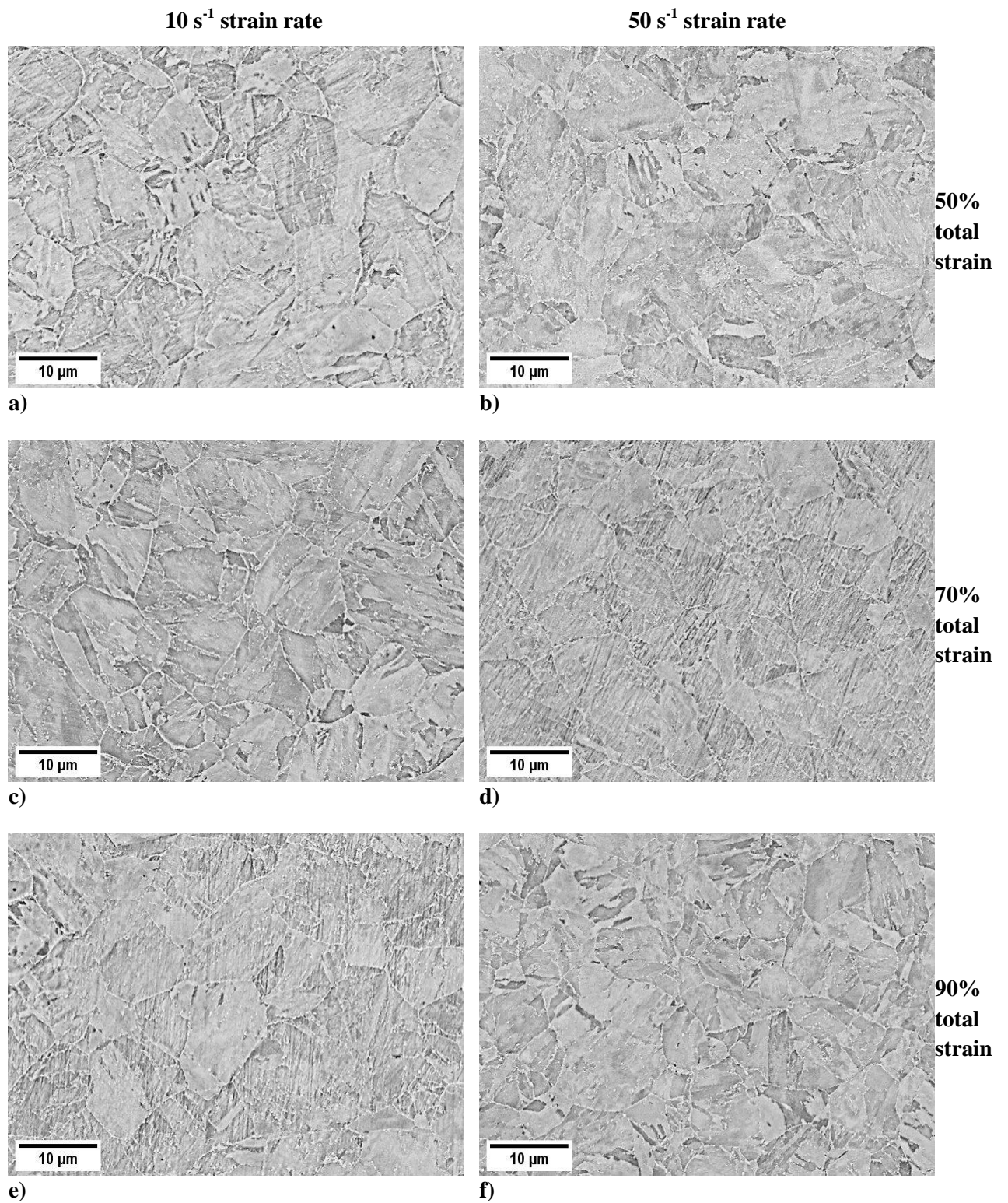


Figure 4.21: SEM-BSE micrographs of P92 samples deformed at 1100 °C and heat treated for 3 hours 45 minutes (scale bar = 10 μm).

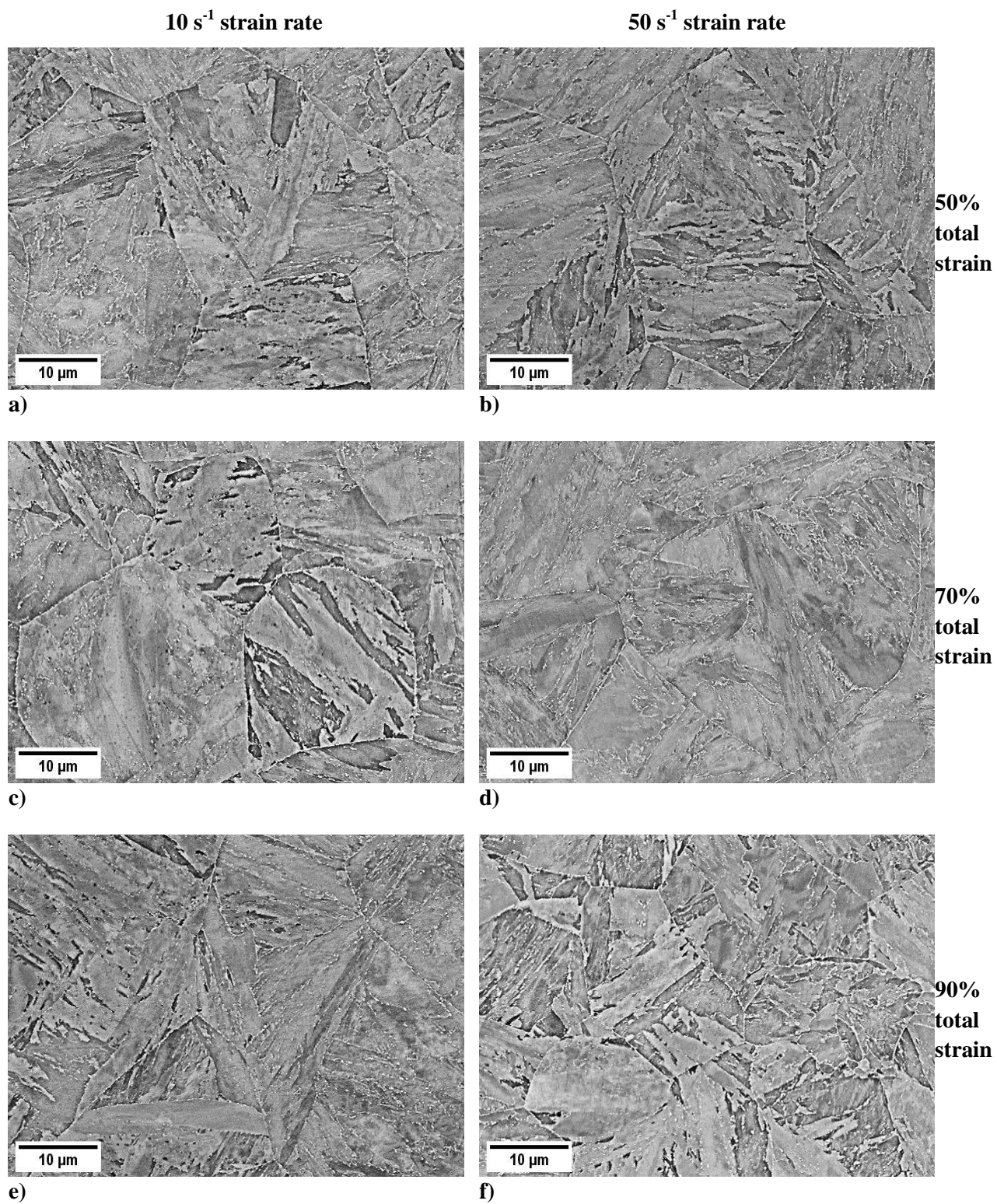


Figure 4.22: SEM-BSE micrographs of P92 samples deformed at 1200 °C and heat treated for 3 hours 45 minutes (scale bar = 10 μm).

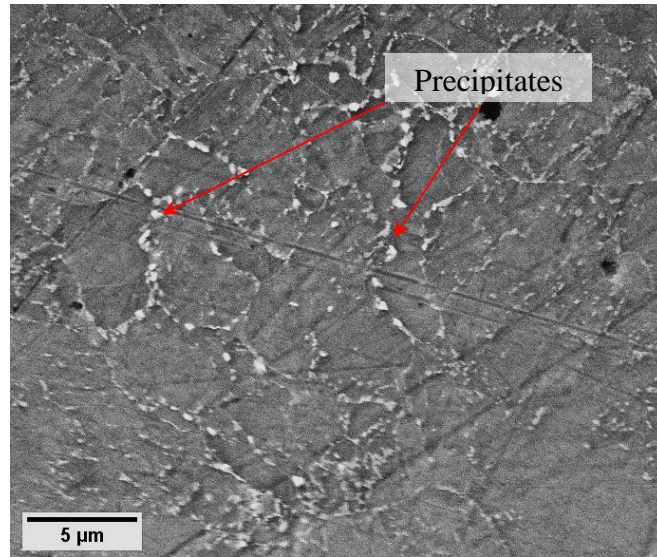


Figure 4.23: SEM-BSE micrograph of P92 sample deformed at 1100 °C and heat treated (scale bar = 5 μm).

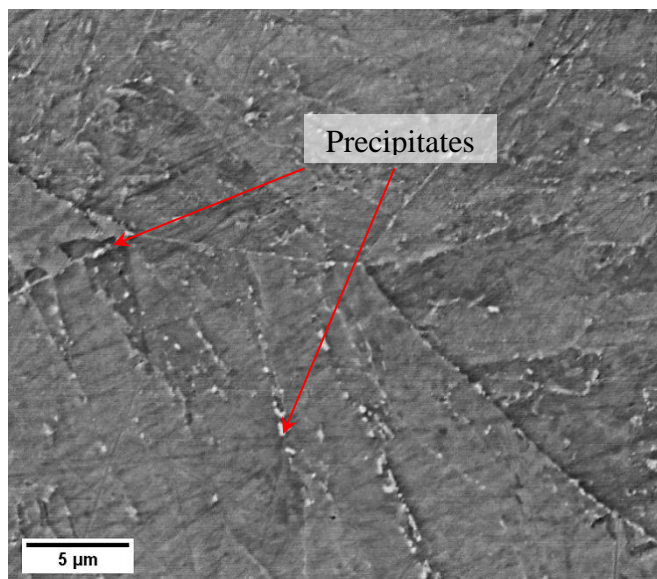


Figure 4.24: SEM-BSE micrograph of P92 sample deformed at 1200 °C and heat treated (scale bar = 5 μm).

Table 4.7: Average grain sizes of the tempered samples.

		Average grain size (μm)				Total strain (%)
Soak time:		3 hours 45 minutes		5 hours		
Deformation strain rate:		10 s ⁻¹	50 s ⁻¹	10 s ⁻¹ ₁	50 s ⁻¹	
Deformation temperature	1100 °C	7±1	6±2	10±1	7±1	50
		8±2	7±1	11±2	6±1	70
		8±1	8±1	7±2	8±1	90
	1200 °C	13±2	20±3	17±3	14±1	50
		18±3	18±1	15±2	18±2	70
		17±2	11±3	23±2	20±4	90

The rod metal had thermo-mechanically affected zones and the interface region. Figure 4.25 is a photograph of a cross-section of the FHPP weld sample with the microstructure revealed by Vilella's reagent. Six distinct zones were identified on the FHPP weld (Figure 4.25).

SEM-BSE micrographs of zones A to F and the average sizes of prior austenite grains are presented in Figure 4.26. Zone B (Rod-TMZ) experienced high strains, resulting in a microstructure without well-defined prior austenite grain boundaries. The analysed weld region had good integrity as no voids, cracks, or any form of debonding were observed along the rod - base metal interface at zone C. The microstructures of all the weld zones were tempered martensite because there were carbides decorating the laths and prior austenite grain boundaries as shown in Figure 4.27.

- A: Rod metal heat affected zone (Rod-HAZ)
- B: Rod metal thermo-mechanically affected zone (Rod-TMZ)
- C: Rod-Base metal interface
- D: Base metal thermo-mechanically affected zone (BM-TMZ)
- E: Base metal heat affected zone (BM-HAZ)
- F: Base metal (BM)

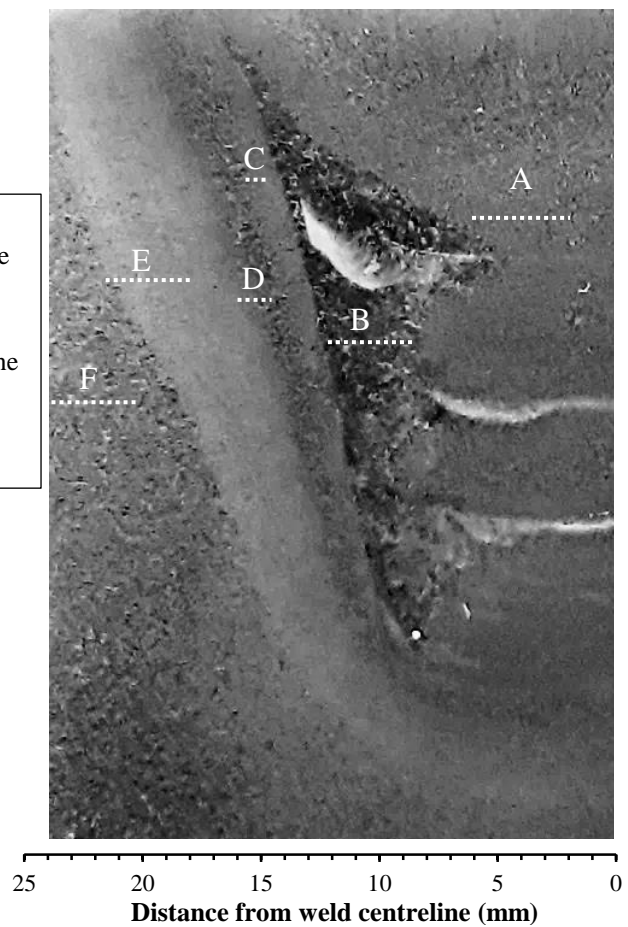


Figure 4.25: Micrograph of P92 FHPP weld cross-section with the dashed lines indicating the regions where hardness indentations were made.

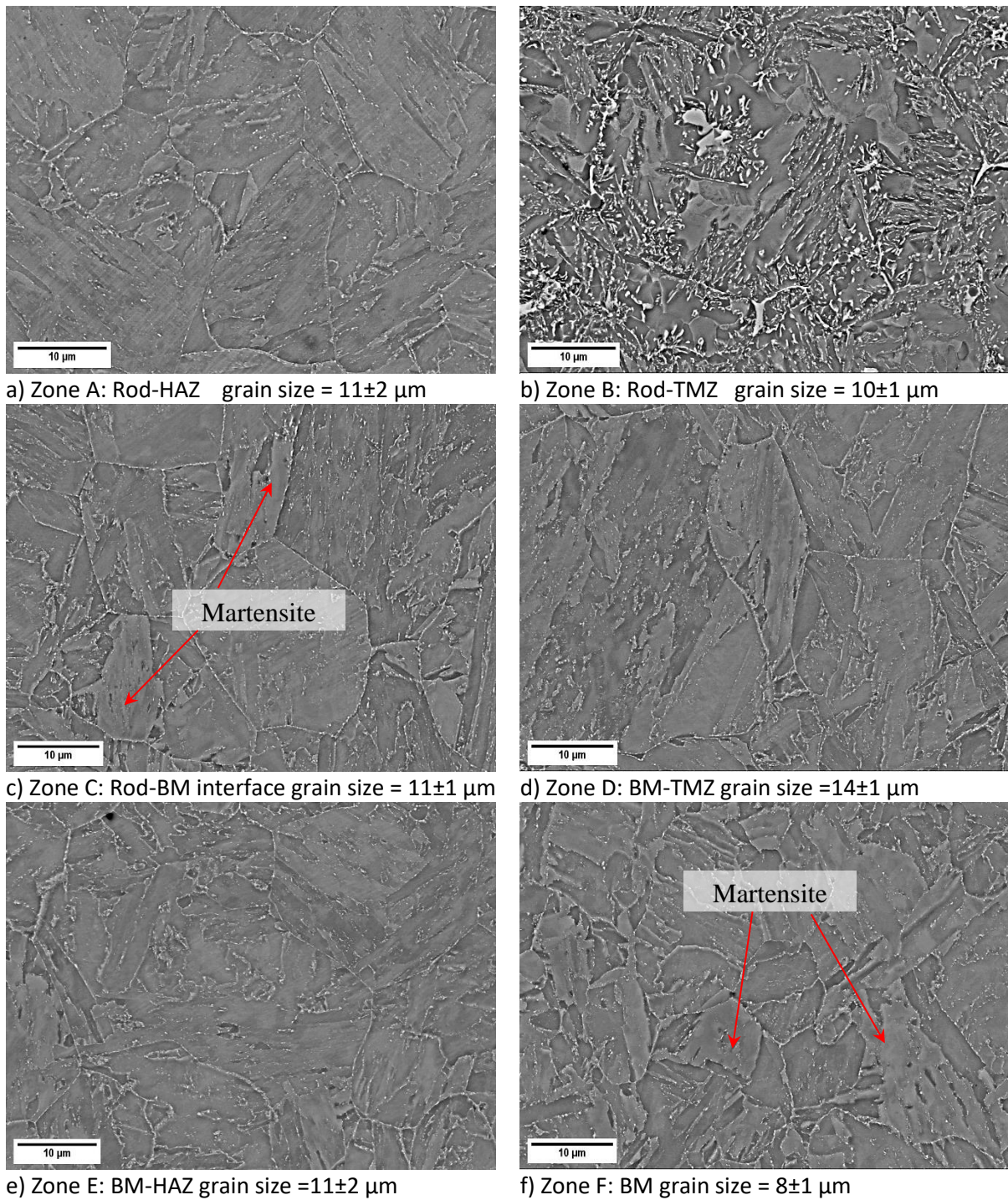


Figure 4.26: Higher magnification SEM-BSE images of FHPP weld regions with the average prior austenite grain sizes (scale bar = 10 μm).

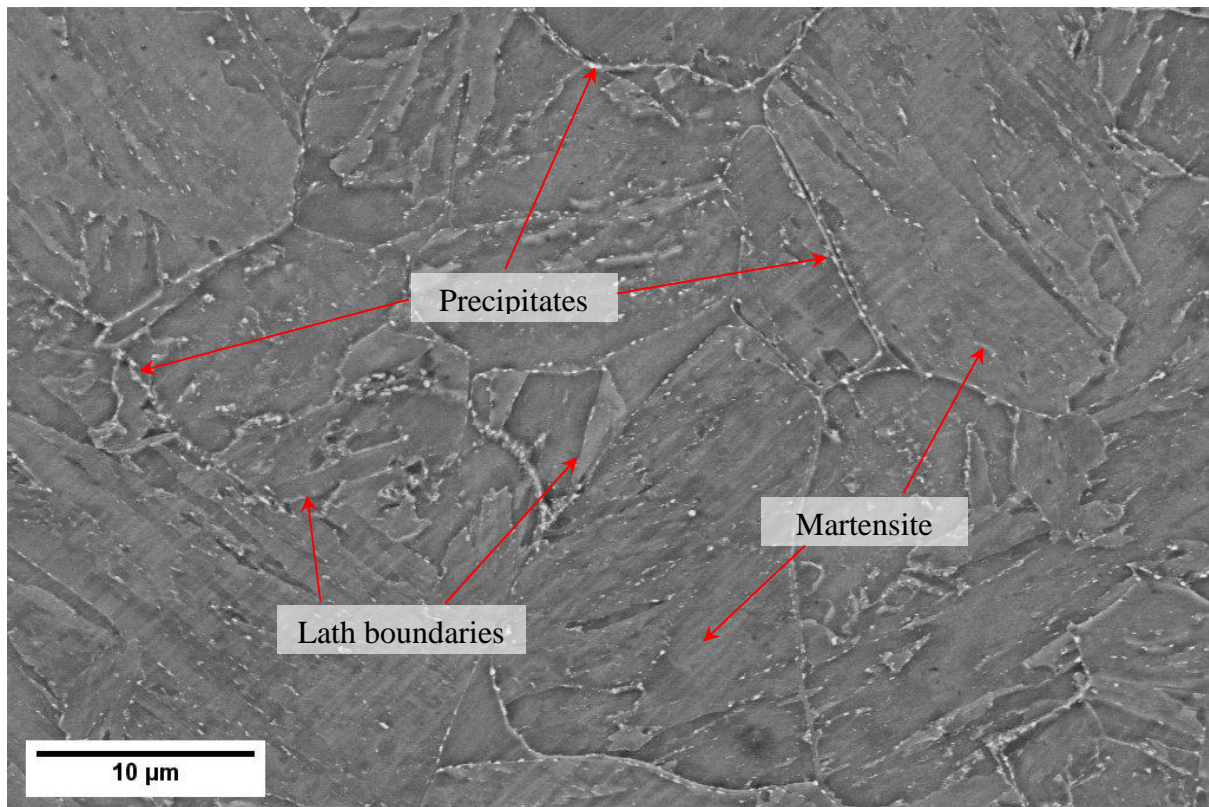


Figure 4.27: SEM-BSE image of Zone A: Rod-HAZ, showing precipitates on martensite lath boundaries (scale bar = 10 μm).

4.3.3 X-ray diffraction

An X-ray diffraction pattern of the phases in the as-received P92 pipe steel is given in Figure 4.28. Three major peaks of alpha ferrite were matched, and small amounts of precipitates had very low intensities masked by the high background counts in the XRD patterns.

Figure 4.29 shows XRD patterns for three different regions of the weld: rod-HAZ (A), BM-HAZ (E) and BM (F). The XRD patterns showed mainly the alpha ferrite, as the other minor phases and precipitates had very low volumes and were masked by the high background in the patterns. The major peak of the BM-HAZ has a lower intensity than the BM and rod-HAZ.

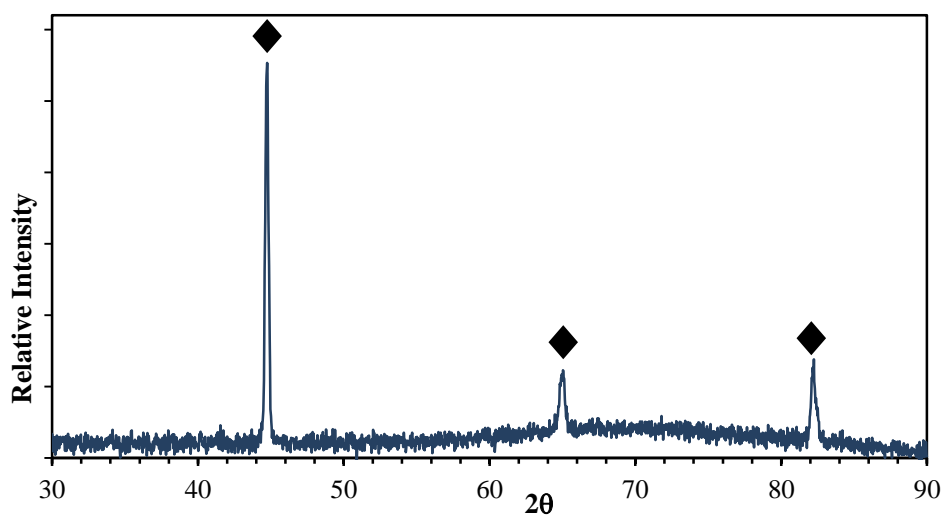


Figure 4.28: XRD pattern of the as-received P92 pipe steel sample.

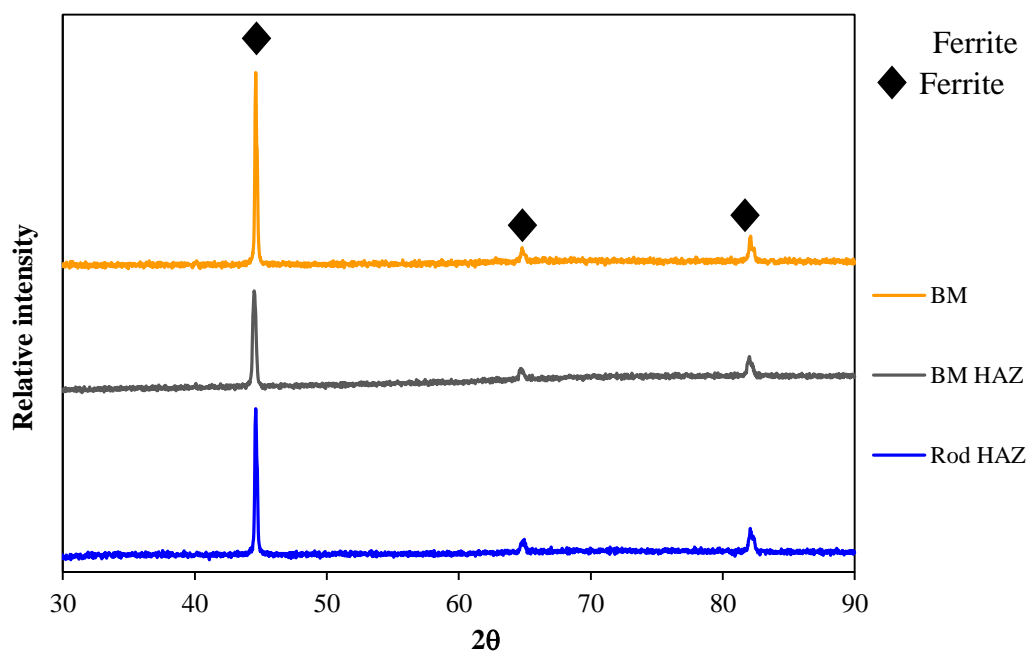


Figure 4.29: XRD patterns of the BM (F), BM-HAZ (E) and Rod-HAZ (A) zones of the FHPP weld section, where zones are labelled as in Figure 4.25.

4.3.4 Hardness

Figures 4.30 and 4.31 show the Vickers hardnesses with standard deviations of the P92 pipe steel specimens deformed at 1100 °C and 1200 °C. The compressed specimens had hardnesses ~ 200 HV_{0.3} higher than the 227 HV_{0.3} of the as-received sample. The error-bars overlap which suggests a minor difference on hardness values at 10 and 50 s⁻¹ strain rates.

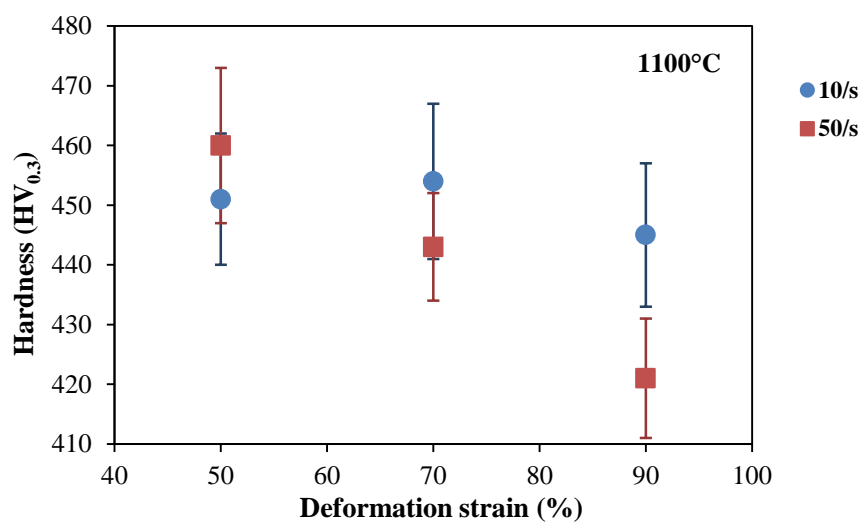


Figure 4.30: Effect of strain rate on hardness of P92 pipe samples deformed at 1100 °C.

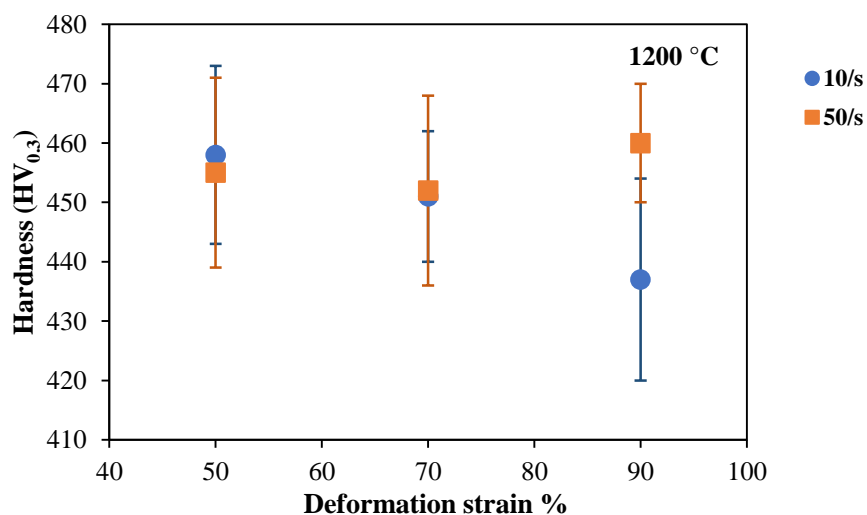


Figure 4.31: Effect of strain rate on hardness of P92 pipe samples deformed at 1200 °C.

Tempering heat treatments at 760 °C with soak times of 3 hours 45 minutes or 5 hours were done on the hot compressed specimens to simulate the post-weld heat treatment done on the FHPP sample. Figures 4.32– 4.35 show the average hardnesses for the two heat treatments. Overall, the hardnesses of the specimens soaked for 5 hours were lower than those after 3 hours 45 minutes. Figures 4.34 and 4.35 show a trend of hardness increasing with deformation strain.

The y-axis scale used in Figure 4.35 is different to Figures 4.32 – 4.34 because the hardness of specimen deformed at 1100 °C and 50 s⁻¹ at 50 % strain was lower than as-received pipe sample, 227 HV_{0.3} after 5 hours heat treatment.

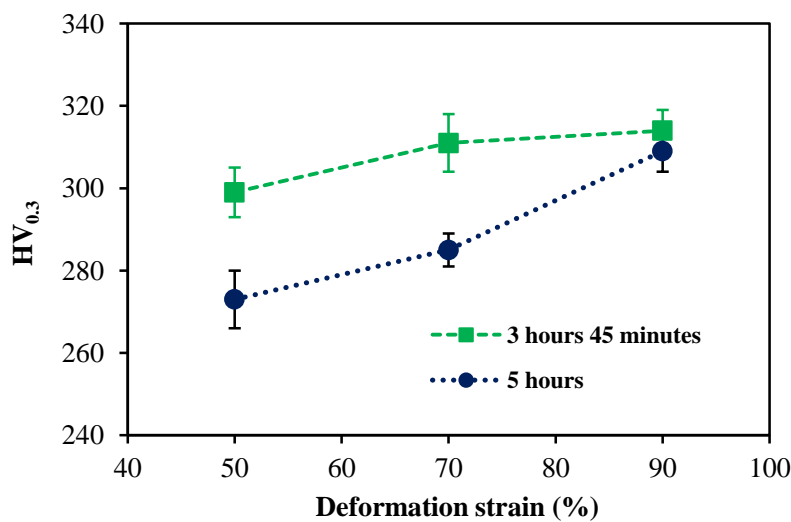


Figure 4.32: Effect of heat treatment on hardness of P92 pipe samples deformed at 1200 °C and 10 s⁻¹ and heat treated.

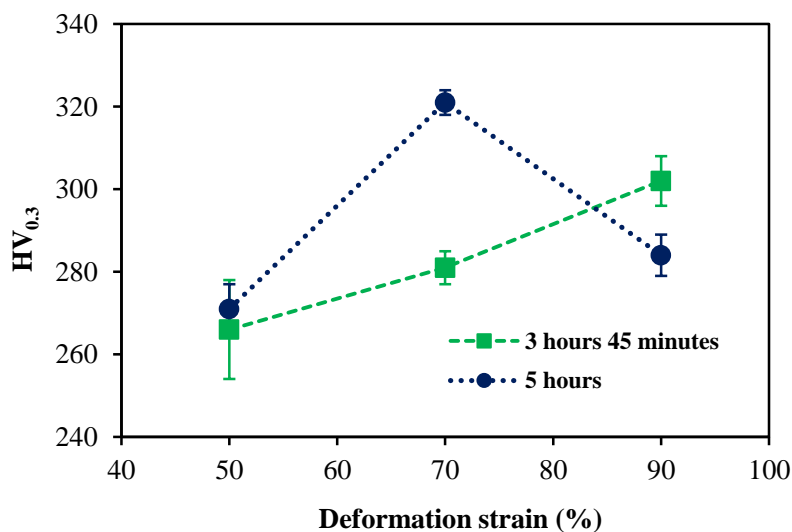


Figure 4.33: Effect of heat treatment on hardness of P92 pipe samples deformed at 1200 °C and 50 s⁻¹ and heat treated.

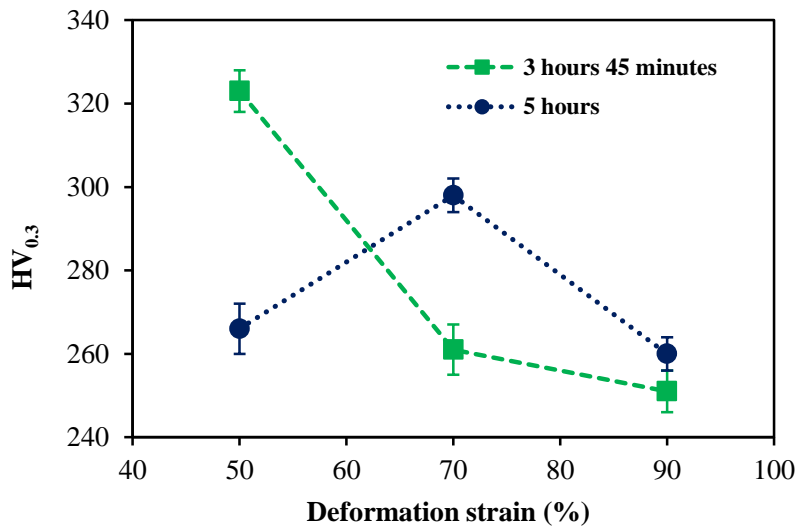


Figure 4.34: Effect of heat treatment on hardness of P92 pipe samples deformed at 1100 °C and 10 s⁻¹ and heat treated.

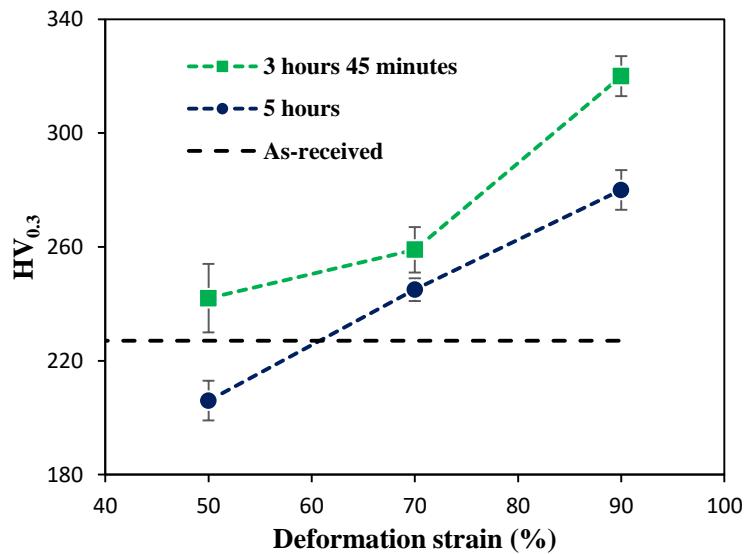


Figure 4.35: Effect of heat treatment on hardness of P92 pipe samples deformed at 1100 °C and 50 s⁻¹ and heat treated.

Table 4.8 shows the average hardnesses and standard deviations of the distinct weld zones. The average hardnesses of zones A-D *i.e.* 3 rod zones (Rod-HAZ, Rod-TMZ, Rod-BM interface, and the base metal TMZ) were all in the range 265 – 270 HV_{0.3}. The base metal (F) and its heat affected zone (E) were ~35 HV_{0.3} softer than these regions.

Table 4.8: Hardness gradient across the weld ($HV_{0.3}$).

FHPP weld hardness ($HV_{0.3}$).					
A	B	C	D	E	F
267 \pm 5	270 \pm 15	265 \pm 4	266 \pm 10	225 \pm 12	229 \pm 4

A; Rod metal heat affected zone (Rod-HAZ)

B: Rod metal thermo-mechanically affected zone
(Rod-TMZ)

C: Rod-Base metal interface

D: Base metal thermo-mechanically affected zone
(BM-TMZ)

E: Base metal heat affected zone (BM-HAZ)

F: Base metal (BM)

Chapter 5 :Discussion

5.1 Thermodynamic calculations

Thermo-Calc results showed that Laves phase, $M_{23}C_6$ and MX precipitates were formed below the deformation temperatures of the pipe samples, 1100 °C and 1200 °C (Table 4.1). MX precipitates started forming at 1050 °C, whereas Laves phase formation started at 728 °C and $M_{23}C_6$ precipitates at 897 °C. This showed the high thermal stability of the MX precipitates.

The Thermo-Calc results indicated the absence of retained austenite (FCC phase) in the as-received sample (Table 4.3) which agrees with the XRD pattern (Figure 4.28). Furthermore, the $M_{23}C_6$, MnS and MX precipitates were identified by EDX (Figure 4.14). The Laves phase was not identified but its component elements: Fe, Mo, W and Cr were all detected by EDX (Table 4.5). However, M_2B was not identified by EDX (Table 4.6) and its main component element, boron was also not identified with EDX, which could be because it is a light element, and EDX is not optimal for identifying light elements. However, boron was only present in low amounts in OES results (Table 4.4). Thermo-Calc showed precipitates forming below both deformation temperatures, 1100 °C and 1200 °C, which agreed with the microstructures, which showed no precipitates in the as-deformed samples (Figures 4.17 and 4.18). Similarly, the microstructure of the as-received sample had precipitates (Figure 4.13) as also indicated by Thermo-Calc (Table 4.1).

5.2 Hot compression of P92 steel

The deformation temperatures used in this study were high at 1100 °C and 1200 °C, so the effect of adiabatic heating on the flow curves can be neglected, thus isothermal conditions may be assumed [118, 119]. The decrease of the flow stresses with increasing temperature was attributed to the coarse grains at 1200 °C (Figures 4.19 and 4.22). Coarse grains have fewer grain boundaries which reduces the hardness of the material [66, 67]. Figures 4.4 and 4.5 show that the maximum and proof stresses (taken at 0.2 %) decreased with increasing temperature and decreasing strain rates. Although these graphs are preliminary since they have only two points (more points would be better), their trend agrees with the flow curves

(Figures 4.2 and 4.3). The high deformation temperature, 1200 °C, and low strain rate, 10 s^{-1} , could have allowed longer time for grain growth and dislocation movement [52]. Furthermore, rate of restoration processes (DRX and DRV) increased at 1200 °C, which decreased strain hardening and hence decreased the flow stresses [120].

At a fixed deformation temperature and strain rate, the flow stress increased at deformation strains higher than 0.6 due to increased interface friction between the anvil and specimens. This behaviour was also observed by Jiang *et al.* [121]. There were oscillations on the curves for tests done at the high strain rate of 50 s^{-1} , which was mainly because of changing strain rate from the uneven hydraulic movement. However, continuous work hardening also contributed towards the oscillatory behaviour, since less time was available for dynamic recovery at 50 s^{-1} which was also observed by Anand *et al.* [122].

The lubricant also contributed to the high flow stresses above 0.6 total strains. The lubricant used in the current study was tantalum foil, which is stronger than graphite foil at the tested temperatures. Although the tantalum foil did not break during the compression tests, the sample diameter increased, and sample had direct contact with the anvil which increased the friction.

5.3 Characterization

5.3.1 Chemical analysis

The difference in the compositions of the rod, pipe and base materials were very small and the alloying elements detected were the same in all the materials (Tables 4.4 and 4.5). The compositional difference for the key constituents: chromium, tungsten, molybdenum, and vanadium were in less than 5%. This suggested that they were all P92 steels, although some elements had differences, the samples were assumed to be from the same cast. There were variations in Nb, Mn and Co, and N and Cd showed larger differences, although these elements were less than 1% which is close to the detection limit of EDX. For the EDX analyses, the composition of carbon could have included the graphite foil used during SEM analyses, so it was omitted. However, EDX is not a good technique for analysing carbon and other light elements, and EELS or WDS with TEM are preferred, but were not easily available.

5.3.2 Microstructural analysis

Heat treatment of the as-received pipe sample resulted in a tempered martensite with precipitates along the grain boundaries, because it was heat treated at 760 °C which is below its lower transformation temperature, 811 °C (Figures 4.12 and 4.13). The small regions of ferrite present in the microstructure (Figure 4.13) formed during cooling from casting. The precipitates which formed during the tempering of the steel were identified by SEM-EDX: $(V,Nb)_2N$, $(Cr,Fe,Mo,W)_{23}C_6$, $(Mn,Cu)S$ and Cr_2N (Table 4.6). EDX analysis also identified oxide inclusions: Al_2O_3 and MgO , which formed during casting [123].

The Cr and Ni equivalents for a typical T/P92 steel composition, a T/P911 and three experimental creep resistant steels are shown on the Schaeffler–Schneider diagram [50] in Figure 5.1. The T/P92 steel lies on the boundary of martensite and martensite + ferrite, and has mostly martensite, with $\leq 2\%$ ferrite. The P92 steel pipe composition with a Cr_{eq} of 13.3 and a Ni_{eq} of 5.1, lies on the boundary of martensite and martensite + ferrite. Therefore, with Cr_{eq} greater than 6.5, it may contain a minor amount of ferrite.

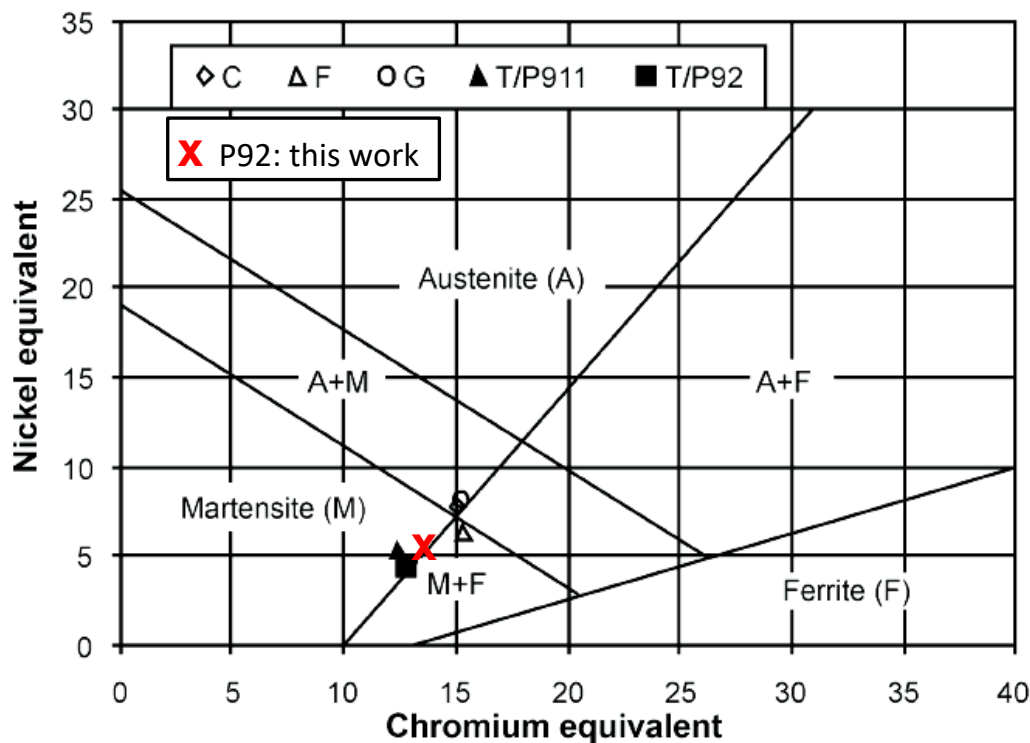


Figure 5.1: The Schaeffler–Schneider diagram showing the relative positions of various steels including a T/P92 steel [50] and the P92 steel from this work.

The as-deformed specimens had untempered martensite (Figures 4.17 and 4.18), as expected, because the hot compression tests were done at temperatures above the upper austenite to ferrite transformation temperature of 884°C (Table 4.1), and then air cooled at 5 °C.s⁻¹ after deformation. A continuous cooling transformation diagram for steel P92, Figure 2.13, indicated that a fully martensitic structure is achievable by cooling the steel from an austenitising temperature of 1050 °C, at cooling rates between 0.1 – 10 °C s⁻¹ [124].

The higher strains experienced during deformation transformed the lath structure of the as-received sample (Figures 4.8) into finer globular martensite (Figures 4.9 and 4.10). There was more grain size distinction at different deformation temperatures than for different strain rates, which implied that deformation temperature had a greater effect on the grain size than strain rate. Fine grains were formed during deformation at 1100 °C, because less energy was available for grain growth than at 1200 °C. At both deformation temperatures, 1200 °C and 1100 °C, the grains were slightly finer at the higher strain rate of 50 s⁻¹ than for 10 s⁻¹. This was due to the reduced deformation time at the higher strain rate, leading to insufficient time and energy for recrystallized grains to grow [56].

Heat treatments on the deformed specimens at 760 °C for both 3 hours 45 minutes and 5 hours changed the microstructure from untempered martensite (Figures 4.9 and 4.10) to tempered martensite with precipitates decorating the prior austenite grain boundaries (Figures 4.19 – 4.24). This was due to the tempering temperature of 760 °C being below the lower transformation temperature of 811 °C (Table 4.1). There was no notable difference in grain sizes between the samples heat treated for 5 hours and 3 hours 45 minutes (Table 4.7).

The high strain rates and temperatures experienced during FHPP welding resulted in a weld microstructure with six distinct zones without (Figure 4.25). The microstructure was similar to that found by Hattingh *et al.* [1] in Figure 2.16. Since the post weld heat treatment (PWHT) of the weld sample was done at 760 °C, which is below the lower transformation temperature of the steel, this produced tempered martensite with the precipitates on the prior austenite grain boundaries (Figures 4.26 and 4.27). The variations in grain size across the weld zones were ascribed to the temperature gradient experienced during the friction hydro-pillar processing. The zones adjacent to the interface between the rod and base metal: Rod HAZ, TMZ and BM-TMZ had coarser grains than the BM-HAZ and BM zones further away from the interface due to the higher peak temperatures experienced in the interface region

which favoured grain growth. The thermocouples placed near the heat affected zone showed that the temperatures were above 1075 °C.

The microstructures of the FHPP weld, as-received pipe sample and heat treated samples were tempered martensite because they had similar transformation temperatures (having similar compositions) and were all heat treated at 760 °C. The deformed samples could only be compared with Zones A and B of the weld sample because those are the regions where the highest temperatures and strain rates were experienced. The average grain sizes of Zones A and B (Figure 4.26) were similar to samples deformed at 1100 °C, 10 ± 1 μm (Table 4.7).

5.3.3 X-ray diffraction

The X-ray patterns for both FHPP weld and pipe samples had no austenite peaks, implying that very little or no austenite was retained (Figures 4.28 and 4.29). The positions of the ferrite peaks were similar to those of P91 and P92 steels studied by Zhou *et al.* [79] and Pandey *et al.* [125].

5.3.4 Hardness

The hardness of P92 steel depends on the factors such as grain size, the presence and distribution of fine precipitates, and the presence of carbon and nitrogen in solution [126-128]. The as-received pipe sample had an average hardness of 227 ± 5 $\text{HV}_{0.3}$ which complies with the design specification of 210-265 $\text{HV}_{0.3}$ for P92 steel [129].

The hardnesses of the compressed specimens were ~ 200 $\text{HV}_{0.3}$ higher than the as-received sample (Figures 4.30 and 4.31). The large change in hardness after deformation was due to the formation of untempered martensite (Figures 4.17 and 4.18). The measured hardnesses of the deformed specimens were higher than 400 $\text{HV}_{0.3}$, which is within the 400-480 $\text{HV}_{0.3}$ reported hardness range for untempered martensite in P92 steel [130]. The untempered martensite formed after compression on direct air cooling (rate of $5\text{ }^{\circ}\text{C.s}^{-1}$) to room temperature, whilst the as-received steel had undergone more complex heat treatments whereby it was normalised between 1040 °C and 1080 °C and cooled to room temperature to produce full martensite without retained austenite and then tempered at 760 °C; this tempering temperature is determined by the steel composition [131]. The deformation temperatures for the current study were 1100 and 1200 °C, thus high enough to dissolve the

precipitates as shown in Table 4.1. This resulted in solid solution strengthening and contributed slightly to the increased hardness after deformation [132-133].

The microstructure of the deformed specimens transformed from hard untempered to softer tempered martensite after heat treatment (Figures 4.9 and 4.10). The average hardnesses of the compressed specimens decreased after both heat treatments (Figures 4.30 - 4.35). The change in hardness after heat treatment was due to the formation of precipitates as shown in Figures 4.23 and 4.24. The formation of precipitates occurred as the constituents were drawn from the solid solution, which decreased solid solution strengthening. Also, the increase in grain size, as shown in Figures 4.9 and 4.10, after heat treatment decreased the hardness of the specimens (Figures 4.30-4.35).

The hardness varied across the weld zones due to the temperature gradient (Table 4.8). The rod-TMZ had the highest hardnesses due to severe deformation experienced in this region, as shown in Figure 4.26 b. The Rod-HAZ and the TMZs had higher hardnesses despite having coarse grains (Figure 4.26), thus the precipitates dissolution had more effect on the hardness than grain size.

The simulated Thermo-Cal results agreed with the experimental results from XRD, microscopy and EDX analyses which gives confidence in the results obtained in this study. The FHPP technique produced a weld with good integrity without cracks. Heat treatment recovered the as-received microstructure after deformation which shows the importance of PWHT on the FHPP welds, and that it is a viable process for steam pipes repair.

Chapter 6 :Conclusions

The current study investigated the transformation of phases in P92 steel during hot deformation and heat treatment and the microstructural changes in P92 steel and FHPP P92 welds. The findings can be summarized as follows:

- Thermo-Calc results of deformed P92 pipe steel showed that the BCC phase existed as delta ferrite until 1175 °C and alpha ferrite formed from 884 while FCC phase existed until 811 °C. The main precipitates: $M_{23}C_6$, MX and Laves phase formed from 897 °C, 1050 °C and 728 °C respectively, therefore they were absent at the deformation temperatures 1100 °C and 1200 °C.
- The more time and energy available at high temperature, 1200 °C and low strain rate, 10 s^{-1} during hot compression of P92 steel, caused grain growth, which led to a decrease in flow stresses.
- The flow stresses at 10 s^{-1} and 1100 °C were higher than the flow stresses at 1200 °C and 50 s^{-1} showing the greater effect of temperature on flow stress than strain rate during deformation of P92 steel.
- Heat treatment at 760 °C on both 3 hours 45 minutes and 5 hours, restored the microstructure of the P92 steel to tempered martensite after hot deformation, thus overcoming the effect of high temperatures and high strain rates such as formation of untempered martensite and its high hardness.
- The difference in grain sizes for samples deformed at 10 s^{-1} and 50 s^{-1} was small, similar to the 3 hours 45 minutes and 5 hours heat treatments. There were different grain sizes at different deformation temperatures, 1100 °C and 1200 °C: larger grains were achieved at 1200 °C and smaller grains at 1100 °C. This shows that deformation temperature had more effect on microstructure of P92 steel during deformation than strain rates and heat treatment times.
- XRD patterns showed that heat treatment of P92 steels at 760 °C successfully achieved microstructures which were free of retained austenite.
- The compositions of the as-received pipe sample and the FHPP weld were similar which suggest that they were made of the same alloy, P92. However, there were notable differences in some of the elements which suggested inhomogeneity in the alloys. Additionally, the carbon contents were not considered when analysing the

phases, because SEM has limitations for light metals, therefore better carbon analysis methods are required, although the microstructures were also used to identify the phases.

- A complex friction hydro-pillar processing weld showed at least six distinct zones: rod-heat affected zone, rod-thermo-mechanically affected zone, rod-base metal interface, base metal-thermo-mechanically affected zone, base metal-heat affected zone and base metal. The weld had good integrity, with no voids observed.
- Based on the similar microstructures and hardness values between heat treated samples and the FHPP weld, thermo-mechanical simulations with a Gleeble thermo-mechanical simulator have potential to reproduce FHPP welds.

Chapter 7 :Recommendations

For further work on FHPP simulation using Gleeble, the following should be considered:

- Temperatures 1100 and 1200 °C together with strain rates 10 and 50 s⁻¹ can be taken as test parameters. However, at high strain rates, Gleeble jerking can be a problem.
- The total strain should be taken at 50% maximum to avoid friction due to direct contact between the anvils and the sample.
- For more accurate FHPP simulations, Gleeble torsion testing should also be considered which can be done at DSI's factory in Albany, New York.
- TEM analysis is required for more detailed analysis of the microstructure and precipitates.

Chapter 8 :References

- [1] D.G. Hattingh, L. von Wielligh, W. Thomas, and M.N. James, “Friction processing as an alternative joining technology for the nuclear industry,” *J. South. African Inst. Min. Metall.*, vol. 115, no. 10, pp. 903–912, 2015.
- [2] D.T. Buzzatti, J.T. Buzzatti, R.E. dos Santos, F. Mattei, M. Chludzinski, and T.R. Strohaecker, “Friction Hydro Pillar Processing: Characteristics and Applications,” *Soldag. Inspeção*, vol. 20, no. 3, pp. 287–299, 2015.
- [3] C.R. Lessa, D. Martinazzi, A.P. Figueiredo, R.B. Machado, C. Fanezi, and T. Strohaecker, “Microstructural behavior of SAF 2205 Duplex Stainless Steel Welded by Friction Hydro Pillar Processing,” *Mater. Res.*, vol. 19, no. 4, pp. 928–936, 2016.
- [4] F. Yeh, P. Cunha, C. Lessa, T. Clarke, and T. Strohaecker, “Evaluation of Discontinuities in A36 Steel Repairs with Friction Hydro Pillar Processing Using Different Axial Forces,” *ISI Int.*, vol. 53, no. 12, pp. 2269–2271, 2013.
- [5] E.D. Nicholas, “Friction Processing Technologies,” *Weld. World*, vol. 47, pp. 2–9, 2003.
- [6] W.M. Thomas, E.D. Nicholas, and S.W. Kallee, “Friction based technologies for joining and processing,” *TMS, Frict. Stir Weld. Process.*, Warrendale, PA, pp. 3–13, 2001.
- [7] C.P. Meinhardt, M. Chludzinski, R.F. Ribeiro, C.L.F. Rocha, A.C.S. Santos, and T.R. Strohaecker, “Evaluation of friction hydro-pillar processing welding in duplex stainless steels (UNS S31803),” *J. Mater. Process. Technol.*, vol. 246, pp. 158–166, 2017.
- [8] D.L.H. Bulbring, D.G. Hattingh, A. Botes, and D.H. Odendaal, “Friction Hydro Pillar Process as an alternative repair technology for creep evaluation sites on thick-walled 10CrMo910 creep-resistant steel structures,” *J. South. African Inst. Min. Metall.*, vol. 113, no. 2, pp. 129–136, 2013.
- [9] A. Ambroziak, “Investigations of underwater FHPP for welding steel overlap joints,” *Arch. Civ. Mech. Eng.*, vol. VII, no. 2, pp. 67–76, 2007.
- [10] M. Chludzinski, M.P. Paes, F.L. Bastian, and T.R. Strohaecker, “Fracture toughness of Friction Hydro-Pillar Processing welding in C-Mn steel,” *Mater. Des.*, vol. 33, no. 1, pp. 340–344, 2012.
- [11] L. Cui, X. Yang, D. Wang, X. Hou, J. Cao, and W. Xu, “Friction taper plug welding for S355 steel in underwater wet conditions: Welding performance, microstructures and mechanical properties,” *Mater. Sci. Eng. A*, vol. 611, pp. 15–28, 2014.
- [12] I. Wedderburn, P. Doubell, D.G. Hattingh, and M. Newby, “Condition Monitoring of High Temperature, High Stress Components by Means of Core Sampling and Friction Weld Repair,” *Proc.Conf.18th World Conf. Nondestruct. Test.*, 16-20 April 2012, Durban, South Africa.
- [13] Y. Yin, X. Yang, L. Cui, J. Cao, and W. Xu, “Microstructure and mechanical properties of underwater friction taper plug weld on X65 steel with carbon and stainless steel plugs,” *Sci. Technol. Weld. Join.*, vol. 21, no. 4, pp. 259–266, 2016.

- [14] S.A. David, J.A. Siefert, and Z. Feng, "Welding and weldability of candidate ferritic alloys for future advanced ultrasupercritical fossil power plants," *Sci. Technol. Weld. Join.*, vol. 18, no. 8, pp. 631–651, 2013.
- [15] D. Coutsouradis, "Materials for advanced power engineering" Conference Proc., Part 1, Liège, Belgium, 3-6 October 1994.
- [16] J. Lecomte-Beckers, M. Carton, F. Schubert, P.J. Ennis "Materials for advanced power engineering", Proc. 8th Liego conf., Part 1, Belgium, 18-20 Sep. 2006.
- [17] F. Masuyama, and J.P. Shingledecker, "Recent status of ASME code on creep strength enhanced ferritic steels," *Procedia Eng.*, vol. 55, pp. 314–325, 2013.
- [18] V.A. Dudko, A.E. Fedoseeva, A.N. Belyakov, and R.O. Kaibyshev, "Influence of the carbon content on the phase composition and mechanical properties of P92-type steel," *Phys. Met. Metallogr.*, vol. 116, no. 11, pp. 1165–1174, 2015.
- [19] IEA, "Coal." International Energy Agency. Available: <https://www.iea.org/aboutus/faqs/coal/>. [Accessed Jun. 20, 2016]
- [20] "World Coal Association, "Coal and electricity." Available: <http://www.worldcoal.org/coal/uses-coal/coal-electricity>. [Accessed Jun. 22, 2016]
- [21] Department of Energy, South Africa, "Basic electricity." Available: http://www.energy.gov.za/files/electricity_frame.html. [Accessed Jun. 20, 2016]
- [22] "World Energy Council.", "World energy council report confirms global abundance of energy resources and exposes myth of peak oil" Available: <https://www.worldenergy.org/news-and-media/press-releases>. [Accessed Jul. 05, 2016]
- [23] L. Baxter, and R. Desollar, Eds., "Application of advanced technology to ash-related problems in boilers," Springer Science & Business Media, New York, 1995.
- [24] H. Zhuangqi, and G. Jianting, "Development of high temperature materials for energy market in China," *Mater. Adv. Power Gener.*, vol. 53, pp. 189–200, 2006.
- [25] H.K.D.H. Bhadeshia and R.W.K. Honeycombe, *Steels: Microstructure and Properties*, 3rd Edition. Elsevier Ltd, Oxford, 2006.
- [26] S. Wang, L.I. Chang, D. Lin, X. Chen, and X. Hui, "High Temperature Strengthening in 12Cr-W-Mo Steels by Controlling the Formation of Delta Ferrite," vol. 45, pp. 4371–4385, 2014.
- [27] K.L. Murty, and L. Charit, "Structural materials for Gen-IV nuclear reactors: Challenges and opportunities." *J. Nucl.*, vol. 383, no.(1-2), 2008, pp. 189–195.
- [28] D.J. Abson, and J.S. Rothwell, "Review of type IV cracking of weldments in 9–12%Cr creep strength enhanced ferritic steels," *Int. Mater. Rev.*, vol. 58, no. 8, pp. 437–473, 2013.
- [29] "Explore the World of Piping" Available: http://www.wermac.org/pipes/pipe_vs_tube.html. [Accessed Feb. 16, 2021]
- [30] S. Roberts, "Advanced material castings for high temperature coal fired steam turbine applications - part I," *Foundry Trade J. Int.*, vol. 185, no. 3686, pp. 210-212, 2011.
- [31] H. Naoi, M. Ohgami, S. Araki, T. Ogawa, T. Fujita, H. Mimura, M. Sakakibara, Y. Sogoh, and H. Sakurai, "Development of tubes and pipes for ultra-supercritical thermal power plant boilers," *Nippon Steel Corp.*, Tokyo, pp. 22-27, 1993.

- [32] R.L. Klueh, "Elevated temperature ferritic and martensitic steels and their application to future nuclear reactors," *Int. Mater. Rev.*, vol. 50, no. 5, pp. 287-310, 2005.
- [33] H.S.F. Medina, "General Expression of the Zener-Hollomon parameter as a function of low alloy and microalloyed steels," *Acta Mater.*, vol. 44, no. 1, pp. 137-148, 1996.
- [34] M. Maalekian, "The Effects of Alloying Elements on Steels (I)," Report CLD/ESOP, Technische Universitat Graz: Christian Doppler Laboratory for Early Stages of Precipitation, Austria, Oct. 2007.
- [35] T. Shrestha, S.F. Alsagabi, I. Charit, G.P. Potirniche, and M.V. Glazoff, "Effect of heat treatment on microstructure and hardness of Grade 91 steel," *Metals*, vol. 5, no. 1, pp. 131-149, 2005.
- [36] M. Santella, "Improving the performance of creep-strength-enhanced ferritic steels." In *Proc. 23rd Annual Conf. on 'Fossil Energy Materials'*, Pittsburgh, PA, USA, May 2009.
- [37] B. Alexandrov, L. Wang, J. Siefert, J. Tatman, and J. Lippold. "Phase transformations in creep strength enhanced ferritic steel welds." In *Proceedings of the 8th International Congress "Machines, Technologies, Materials"*, Varna. 2011.
- [38] W. Yan, W. Wang, Y. Shan, and K. Yong, "Microstructural stability of 9--12%Cr ferrite/martensite heat-resistant steels," *Front. Mater. Sci.*, vol. 7, no. 1, pp. 1-27, 2013.
- [39] F. Abe, "Precipitate design for creep strengthening of 9% Cr tempered martensitic steel for ultra-supercritical power plants," *Sci. Technol. Adv. Mater.*, vol. 9, no. 1, 013002, 2008.
- [40] C. Chovet, E. Galand, and B. Leduey, "Effect of various factors on toughness in P92 SAW weld metal," *Riv. Ital. della Saldatura*, vol. 60, no. 4, pp. 547-553, 2008.
- [41] P.J. Dobson, "Why new US supercritical units should consider T/P92 piping," *Power*, 150, no. 3, pp.77-80, 2006.
- [42] F.S. Yin, W.S. Jung, and S.H. Chung, "Microstructure and creep rupture characteristics of an ultra-low carbon ferritic/martensitic heat-resistant steel," *Scri. Mater.*, vol. 6, no. 57, pp. 469-472, 2007.
- [43] J. Hald, "Microstructure and long-term creep properties of 9-12% Cr steels," *Int. J. Press. Vessel. Pip.*, vol. 85, no. 1-2, pp. 30-37, 2008.
- [44] Z. Zhang, G. Holloway, and A. Marshall, "Properties of T/P92 Steel Weld Metals for Ultra Super Critical (USC) Power Plant," *Weld. World*, vol. 6, no. 1, pp. 1-13, 2008.
- [45] R.N. Hajra, A.K. Rai, H.P. Tripathy, S. Raju, and S. Saroja, "Influence of tungsten on transformation characteristics in P92 ferritic-martensitic steel," *J. Alloys Compd.*, vol. 689, pp. 829-836, 2016.
- [46] G. Taniguchi, and K. Yamashita, "Effects of Post Weld Heat Treatment (PWHT) Temperature on Mechanical Properties of Weld Metals for High-Cr," *Kobelco Technol. Rev.*, no. 32, pp. 33-39, 2013.
- [47] K.S. Hosoi, and Y.N. Wade, "Precipitation behavior of Laves-phase and its effect on toughness of 9Cr- 2Mo ferritic martensitic steel," *J. Nucl. Mater.*, no. 141-143, pp. 461-467, 1986.
- [48] A. Aghajani, F. Richter, C. Somsen, S.G. Fries, I. Steinbach, and G. Eggeler, "On the

- formation and growth of Mo-rich Laves phase particles during long-term creep of a 12% chromium tempered martensite ferritic steel,” *Scr. Mater.*, vol. 61, no. 11, pp. 1068–1071, 2009.
- [49] K.H. Lee, S.M. Hong, J.H. Shim, J.Y. Suh, J.Y. Huh, and W.S. Jung, “Effect of Nb addition on Z-phase formation and creep strength in high-Cr martensitic heat-resistant steels,” *Mater. Charact.*, vol. 102, pp. 79–84, 2015.
 - [50] B. Hahn, and W. Bendick, “Pipe steels for modern high-output power plants. Part. 1. Metallurgical principles - long-term properties, recommendations for use,” *3R Int.*, vol. 47, no. 7, pp. 398–407, 2008.
 - [51] N.E.A Shokuhfar, and S.M. Abbasi, “Dynamic recrystallisation under hot deformation of PH Stainless Steel,” *Int. J. ISSI*, vol. 3, no. 1, pp. 8–12, 2006.
 - [52] Q. Guo-Zheng, “Characterization for dynamic recrystallisation kinetics based on stress-strain curves, recent developments in the study of recrystallisation”, In.tech, Croatia, 2013.
 - [53] T.C. Colombo, A.M. Brito, and L. Schaeffer, “Numerical Simulation of Thermomechanical Processes Coupled with Microstructure Evolution,” *Comput. Sci. Eng.*, vol. 16, no. 2, pp. 10–15, 2014.
 - [54] A. Najafizadeh, and J.J. Jonas, “Predicting the Critical Stress for Initiation of Dynamic Recrystallization,” *ISIJ Int.*, vol. 46, no. 11, pp. 1679–1684, 2006.
 - [55] D. Munz, “Fracture of Ceramics and Glass,” *Encycl. Mater. Sci. Technol.*, pp. 3315–3319, Elsevier, 2001.
 - [56] M. Liu, Q.X. Ma, and J. Bin Luo, “Hot deformation behavior and a two-stage constitutive model of 20Mn5 solid steel ingot during hot compression,” *Materials.*, vol. 11, no. 3, 2018.
 - [57] F. Campbell, *Elements of Metallurgy and Engineering alloys*, ASM Int., Ohio, 2008.
 - [58] M. Jafari, and A. Najafizadeh, “Comparison Between the Methods of Determining the Critical Stress for Initiation of Dynamic Recrystallization in 316 Stainless Steel,” *Differentiation*, vol. 24, no. 6, pp. 840–844, 2008.
 - [59] T. Sakai, and J.J. Jonas, “Overview dynamic recrystallization: mechanical and microstructural considerations,” *Acta Metall.*, vol. 32, no. 2, pp. 189–209, 1984.
 - [60] G.R. Stewart, A.M. Elwazri, S. Yue, and J.J. Jonas, “Modelling of dynamic recrystallisation kinetics in austenitic stainless and hypereutectoid steels,” *Mater. Sci. Technol.*, vol. 22, no. 5, pp. 519–524, 2006.
 - [61] K. Huang, and R. Loge, “A review of dynamic recrystallization phenomena in metallic materials,” *Mater.Des.*, vol. 111, pp. 548–574, 2016.
 - [62] I. Mejía, A. Bedolla-Jacuinde, C. Maldonado, and J.M. Cabrera, “Determination of the critical conditions for the initiation of dynamic recrystallization in boron microalloyed steels,” *Mater. Sci. Eng. A*, vol. 528, no. 12, pp. 4133–4140, 2011.
 - [63] T. Sakai, A. Belyakov, R. Kaibyshev, H. Miura, and J.J. Jonas, “Dynamic and post-dynamic recrystallization under hot, cold and severe plastic deformation conditions,” *Prog. Mater. Sci.*, vol. 60, no. 1, pp. 130–207, 2014.
 - [64] V.V. Bulatov, B.W. Reed, and M. Kumar, “Grain boundary energy function for fcc metals,” *Acta Mater.*, vol. 65, pp. 161–175, 2014.

- [65] E.O. Hall, "The deformation and ageing of mild steel: III discussion of results," *Proc. Phys. Soc.*, vol. 64, no. 9, pp. 747–755, 1951.
- [66] N.J. Petch, "The cleavage strength of polycrystals," *J. Iron Steel Inst.*, vol. 174, no. 1 pp. 25–28, 1953.
- [67] C.E. Carlton and P.J. Ferreira, "What is behind the inverse Hall-Petch effect in nanocrystalline materials," *Acta Mater.*, vol. 55, no. 11, pp. 3749–3756, 2007.
- [68] J. Weertman, "Zener-Stroh crack, Zener-Hollomon parameter, and other topics," *J. Appl. Phys.*, vol. 60, no. 6, pp. 1877–1887, 1986.
- [69] D. Samantaray, S. Mandal, and A.K. Bhaduri, "Optimization of hot working parameters for thermo-mechanical processing of modified 9Cr-1Mo (P91) steel employing dynamic materials model," *Mater. Sci. Eng. A*, vol. 528, no. 15, pp. 5204–5211, 2011.
- [70] G.E. Dieter, *Mechanical Metallurgy: SI Metric*, UK, Mc Graw Hill, New York, 1988.
- [71] P. Yan, Z. Liu, W. Liu, H. Bao, and Y. Weng, "Hot deformation behavior of a new 9%Cr heat resistant steel G115," *J. Iron Steel Res. Int.*, vol. 20, no. 9, pp. 73–79, 2013.
- [72] W.F. Zhang, W. Sha, W. Yan, W. Wang, Y.Y. Shan, and K. Yang, "Analysis of deformation behavior and workability of advanced 9Cr-Nb-V ferritic heat resistant steels," *Mater. Sci. Eng. A*, vol. 604, pp. 207–214, 2014.
- [73] C.Y. Liu, R.J. Zhang, and Y.N. Yan, "Hot deformation behaviour and constitutive modelling of P92 heat resistant steel," *Mater. Sci. Technol.*, vol. 27, no. 8, pp. 1281–1286, 2011.
- [74] R.X. Shi, and Z.D. Liu, "Hot deformation behavior of P92 steel used for ultra-supercritical power plants," *J. Iron Steel Res. Int.*, vol. 18, no. 7, pp. 53–58, 2011.
- [75] S. Alsagabi, "High Temperature Deformation Behavior of P92 Steel," *Trans. Indian Inst. Met.*, vol. 69, no. 8, pp. 1513–1518, 2016.
- [76] H. Yang, Z. Li, and Z. Zhang, "Investigation on Zener-Hollomon parameter in the warm-hot deformation behavior of 20CrMnTi," *J. Zhejiang Univ. A*, vol. 7, no. 8, pp. 1453–1460, 2006.
- [77] S.H. Cho, K.B. Kang, and J.J. Jonas, "Mathematical modeling of the recrystallization kinetics of Nb microalloyed steels," *ISIJ Int.*, vol. 41, no. 7, pp. 766–773, 2001.
- [78] J. Hald, "Creep resistant 9-12% Cr steels long-term testing, microstructure stability and development potentials," In *Proc. ECCC Creep Conf.*, London, Nov. 2005.
- [79] X. Zhou, C. Liu, L. Yu, Y. Liu, and H. Li, "Phase Transformation Behavior and Microstructural Control of High-Cr Martensitic/Ferritic Heat-resistant Steels for Power and Nuclear Plants: A Review," *J. Mater. Sci. Technol.*, vol. 31, no. 3, pp. 235–242, 2015.
- [80] A. Výrostková, V. Homolová, J. Pecha, and M. Svoboda, "Phase evolution in P92 and E911 weld metals during ageing," *Mater. Sci. Eng. A*, vol. 480, no. 1–2, pp. 289–298, 2008.
- [81] Z. Zhang, P.M. Singh, and Z.F. Hu, "The Corrosion Behavior of 9Cr Ferritic–Martensitic Heat-Resistant Steel in Water and Chloride Environment," *J. Eng. Mater. Technol.*, vol. 137, no. 3, 0131009, 2015.
- [82] P. Mayr, and I. Holzer, "Microstructural evolution during production—General

- Principles.” In COST 536 Summer School, Lanzarote, 27 Oct. 2008.
- [83] W. Yan, W. Wang, Y.Y. Shan, and K. Yang, “Microstructural stability of 9-12%Cr ferrite/martensite heat-resistant steels,” *Front. Mater. Sci.*, vol. 7, no. 1, pp. 1–27, 2013.
 - [84] V.C. Igwemezie, C.C. Ugwuegbu, and U. Mark, “Physical metallurgy of modern creep-resistant steel for steam power plants: Microstructure and phase transformations,” *Riv. Ital. della Saldatura*, vol. 69, no. 3, pp. 319–339, 2017.
 - [85] Q. Gao, Y. Zhang, H. Zhang, H. Li, F. Qu, J. Han, C. Lu, B. Wu, Y. Lu, and Y. Ma, “Precipitates and Particles Coarsening of 9Cr-1.7W-0.4Mo-Co Ferritic Heat-Resistant Steel after Isothermal Aging,” *Sci. Rep.*, vol. 7, no. 1, pp. 1–11, 2017.
 - [86] A. Czyrska-Filemonowicz, A. Zielińska-lipiec, and P.J. Ennis, “Modified 9 % Cr Steels for Advanced Power Generation : Microstructure and Properties,” *J. Achiev. Mater. Manuf. Eng.*, vol. 19, no. 2, pp. 43–48, 2006.
 - [87] C.G. Panait, W. Bendick, A. Fuchsmann, A.F. Gourgues-Lorenzon, and J. Besson, “Study of the microstructure of the Grade 91 steel after more than 100,000 h of creep exposure at 600 °C,” *Int. J. Press. Vessel. Pip.*, vol. 87, no. 6, pp. 326–335, 2010.
 - [88] K. Sawada, K. Suzuki, H. Kushima, M. Tabuchi, and K. Kimura, “Effect of tempering temperature on Z-phase formation and creep strength in 9Cr-1Mo-V-Nb-N steel,” *Mater. Sci. Eng. A*, vol. 480, no. 1–2, pp. 558–563, 2008.
 - [89] G.E Totten, Ed., *Steel Heat Treatment: Metallurgy and Technologies*. CRC press, Taylor & Francis Group, London, Sep. 28, 2006.
 - [90] R. Dipika, T. Barbadikar, A.R Ballal, D.R Peshwe, P. Syamala Rao, and M.D Mathew, “An assessment of mechanical properties of P92 steel weld joint and simulated heat affected zones by ball indentation technique”. CRC press, Taylor & Francis Group, London, Sep. 28, 2017.
 - [91] T.Barbadikar, R.Dipika, G.S. Deshmukh, L. Maddi, K. Laha, P. Parameswaran, A.R. Ballal, D. R. Peshwe, R.K. Paretkar, M. Nandagopal, and M.D. Mathew. "Effect of normalizing and tempering temperatures on microstructure and mechanical properties of P92 steel," *Int. J. Pres. Vessel. Pip.*, vol. 132, 97-105, 2015.
 - [92] F.Peñalba, X. Gómez-Mitxelena, J.A. Jiménez,M.Carsi, and O.A. Ruano, “Effect of Temperature on Mechanical Properties of 9% Cr Ferritic Steel,” *ISIJ Int.*, vol. 56, no. 9, pp. 1662-7, 2016.
 - [93] J.O. Andersson, T. Helander, L. Höglund, P.F. Shi., and B. Sundman “Thermo-Calc and DICTRA, Computational tools for materials science,” *Calphad*, vol. 26, pp. 273-312, 2002.
 - [94] Overview of Thermodynamic and Properties Databases - 2021a <https://thermocalc.com/about-us/methodology/the-calphad-methodology/>[Accessed Feb. 25, 2021]
 - [95] M. Hillert, and M. Selby, “Computarized Thermodynamics for Materials scientist and Engineers’, Royal Institute of Technology, 2008, <https://thermocalc.com/academia/free-academic-package>. [Accessed Jan. 08, 2021]
 - [96] Q. Chen, H.J. Jou, and G. Sterner. TC-PRISMA User’s Guide. Thermo-Calc Software AB, Stockholm, Sweden, <http://www.thermocalc.com/support/documentation/>, 2015. [Accessed Jan. 15, 2021]

- [97] F. Delany, W. Lucas, W. Thomas, D. Howse, D. Abson, S. Mulligan, and C. Bird, "Advanced joining processes for repair in nuclear power plants," Proceedings of International Forum on Welding Technologies in Energy Engineering. Shanghai, China Sep. 21-23, 2005.
- [98] E. D. Nicholas, "Friction Processes," Weld. World, vol. 47, no. 11, pp. 2–9, 2003.
- [99] W. Li, A. Vairis, M. Preuss, and T. Ma, "Linear and rotary friction welding review," Int. Mater. Rev., vol. 61, no. 2, pp. 71–100, 2016.
- [100] S. Kallee, and D. Nicholas, "Friction and forge welding processes for the automotive industry," SAE Tech. Pap., no. 724, 1999.
- [101] D.R. Raghavendra, "Comparison of Friction Welding Technologies," IJISSET-International J. Innov. Sci. Eng. Technol., vol. 2, p. 12, 2015.
- [102] D.L.H. Bulbring, D.G. Hattingh, A. Botes, and D. H. Odendaal, "Friction Hydro Pillar Process as an alternative repair technology for creep evaluation sites on thick-walled 10CrMo910 creep-resistant steel structures," J. South. African Inst. Min. Metall., vol. 113, no. 2, pp. 903-912, 2013.
- [103] A. Meyer, "Friction hydro pillar processing–bonding mechanism and properties," Master's dissertation, Technical University Braunschweig. 2003.
- [104] T. Nakajima, and A. Sato, " A New Hole-Filling Technique onto Thin Aluminium Alloy Sheets Using a Rotational Consumable Tool." Mater. Transac., vol. 56, no. 12, pp. 263-266, 2015.
- [105] B. Vicharapu, L.F Kanan,T. Clarke, and A. De," An investigation on friction hydro-pillar processing," Sci. Technol. Weld. Join., vol.22, no.7, pp. 555-61, 2017.
- [106] C.P. Meinhardt, M. Chludzinski, R.F. Ribeiro, C.L.F. Rocha, A.C.S. Santos, and T.R. Strohaecker, "Evaluation of friction hydro-pillar processing welding in duplex stainless steels (UNS S31803)," J. Mater. Process. Technol., vol. 246, pp. 158–166, 2017.
- [107] W.M. Thomas, E.D. Nicholas, and S.W Kallee, "Friction based technologies for joining and processing.", TMS (The Minerals, Metals and Materials Society), Friction Stir Welding and Processing Conference, Warrendale, PA, USA, pp. 3-13, Nov. 2001.
- [108] W.M. Thomas, E.D. Nicholas. "Emerging friction joining technology for stainless steel and aluminium applications", "Productivity beyond 2000", IIW Asian Pacific Welding Congress, Auckland, New Zealand, Feb. 1996.
- [109] H.L. Lukas, S.G. Fries, B. Sundman, Computational Thermodynamics — the Calphad Method (Cambridge University Press, UK, 2007).
- [110] Application notes, Gleeble, DSI [<https://www.leeble.com/resources/application-notes.html>] [Accessed May.05, 2015]
- [111] J. Wolk, "Microstructural Evolution in Friction Stir," Diss. Submitt. to Fac. Grad. Sch. Univ. Maryland, degree Dr. Philos., p. 198, 2010.
- [112] A.I. Toumpis, A.M. Galloway, L. Arbaoui, and N. Poletz, "Thermomechanical deformation behaviour of DH36 steel during friction stir welding by experimental validation and modelling," Sci. Technol. Weld. Join., vol. 19, no. 8, pp. 653–663, 2014.
- [113] L. Von Wielligh, Private communication, Department of Mechanical Engineering,

- [114] http://www.iitk.ac.in/meesa/SEM/SEM_manual.pdf [Accessed March.19, 2021]
- [115] ASTM Int. “ASTM Standard E384-11e1, Standard Test Method for Knoop and Vickers Hardness of Materials,” ASTM Int., West Conshohocken, USA, 2011.
- [116] ASTM Int. “ASTM E112-13. Standard Test Methods for Determining Average Grain Size,” 2013 edition, Ohio, Oct. 1, 2013.
- [117] C.R. Anderson., “SEM Illustrative Example: Secondary Electron and Backscatter Electron Images,” Anderson Materials Evaluation, Inc. <http://www.andersonmaterials.com/sem/sem-secondary-backscatter-images.html> [Accessed Jul. 20, 2018]
- [118] M.A. Mostafaei, and M. Kazeminezhad, “Analyses on the flow stress of an Al-Mg alloy during dynamic recovery,” J. Mater. Eng. Perform., vol. 22, no. 3, pp. 700–705, 2013.
- [119] H. Li, Y. Feng, T. Yan, and E. Yu, “Constitutive Model of Warm Deformation Behavior of Medium Carbon Steel,” J. Iron Steel Res. Int., vol. 23, no. 9, pp. 940–948, 2017.
- [120] H. Mirzadeh, J.M. Cabrera, and A. Najafizadeh, “Constitutive relationships for hot deformation of austenite,” Acta Mater., vol. 59, no. 16, pp. 6441–6448, 2011.
- [121] F. Jiang, J. Tang, D. Fu, J. Huang, and H. Zhang, “A Correction to the Stress–Strain Curve During Multistage Hot Deformation of 7150 Aluminum Alloy Using Instantaneous Friction Factors,” J. Mater. Eng. Perform., vol. 27, no. 6, pp. 3083–3090, 2018.
- [122] A. Anand, K. Nageswaran, and V. Kumar, “Hot deformation studies on 2.7 % Si steel using Gleeble thermo-mechanical simulator,” J. Met. Mater Sc., vol. 58, no. 4, pp. 251–258, 2016.
- [123] J.M. Gregg and H.K.D.H. Bhadeshia, “Solid-state nucleation of acicular ferrite on minerals added to molten steel,” Acta Mater., vol. 45, no. 2, pp. 739–748, 1997.
- [124] Y.J. Whan, B. Frederic, E. Dick Robert, C. Kwansoo C, and K.T. Jin, “Plane stress yield function for aluminium alloy sheets-part I: anisotropic behaviour of aluminium alloy”, Int. J. Plast., vol. 19, no.1, pp. 297–304, 2003.
- [125] C. Pandey, M. Mahapatra, P. Kumar, N. Saini, J. Thakare, R. Vidyarthi and H. Narang, “A brief study on δ -ferrite evolution in dissimilar P91 and P92 steel weld joint and their effect on mechanical properties,” Arch. Civ. Mech. Eng., vol. 18, no. 3, pp. 713–722, 2001.
- [126] N. Saini, C. Pandey, and M.M. Mahapatra, “Microstructure Evolution and Mechanical Properties of Dissimilar Welded Joint of P91 and P92 Steel for Subsequent PWHT and N&T Treatment,” Trans. Indian Inst. Met., pp. 1–14, 2017.
- [127] N. Saini, C. Pandey, and M.M. Mahapatra, “Characterization and evaluation of mechanical properties of CSEF P92 steel for varying normalizing temperature,” Mater. Sci. Eng. A, vol. 688, pp. 250–261, 2017.
- [128] T. Shrestha, S.F. Alsagabi, I. Charit, G.P. Potirniche, and M.V. Glazoff, “Effect of heat treatment on microstructure and hardness of grade 91 steel,” Metals, vol. 5, no. 1, pp. 131–149, 2015.

- [129] N.G. Peng, B. Ahmad, R.M. Mohd, and M. Ahadlin, "Microstructure Characterization for P92 Steels Subjected to Short Term Overheating above Critical Transformation Temperatures," *Appl. Mech. Mater.*, vol. 625, pp. 114–117, 2014.
- [130] C. Pandey, M. Mahapatra, P. Kumar, J.G. Thakre, and N. Saini, "Role of evolving microstructure on the mechanical behaviour of P92 steel welded joint in as-welded and post weld heat treated state," *J. Mater. Process. Technol.*, vol. 263, pp. 241–255, 2019.
- [131] S.A. David, J.A. Siefert, and Z. Feng, "Welding and weldability of candidate ferritic alloys for future advanced ultrasupercritical fossil power plants," *Sci. Technol. Weld. Join.*, vol. 18, no. 8, pp. 631–651, 2013.
- [132] B. Yan, Y. Liu, Z. Wang, C. Liu, Y. Si, H. Li, and J. Yu., "The effect of precipitate evolution on austenite grain growth in RAFM steel," *Materials*, vol. 10, no. 9, pp. 1–11, 2017.
- [133] M. El-Rahman Abd El-Salam, I. El-Mahallawi, and M.R. El-Koussy, "Influence of heat input and post-weld heat treatment on boiler steel P91 (9Cr-1Mo-V-Nb) weld joints: Part 2 - Mechanical properties," *Int. Heat Treat. Surf. Eng.*, vol. 7, no. 1, pp. 32–37, 2013.